

NIST-GCR-94-651

---

---

STRUCTURE AND RADIATION  
PROPERTIES OF POOL FIRES

---

---

M. Klassen and J. P. Gore  
School of Mechanical Engineering  
Purdue University  
West Lafayette, IN

Issued June 1994  
August 1992



Sponsored by:  
**U.S. Department of Commerce**  
Ronald H. Brown, *Secretary*  
**Technology Administration**  
Mary L. Good, *Under Secretary for Technology*  
National Institute of Standards and Technology  
Arati Prabhakar, *Director*

### **Notice**

**This report was prepared for the Center for Fire Research of the Building and Fire Research Laboratory of the National Institutes of Standards and Technology, under Grant Number 60NANB1D1169. The statements and conclusions contained in this report are those of the authors and do not necessarily reflect the views of the National Institutes of Standards and Technology, the Building and Fire Research Laboratory, and the Center for Fire Research.**

# **STRUCTURE AND RADIATION PROPERTIES OF POOL FIRES**

by

**M. KLASSEN AND J.P. GORE**

**Thermal Sciences and Propulsion Center  
School of Mechanical Engineering  
Purdue University  
West Lafayette, IN**

**FINAL REPORT: Grant No. 60NANB1D1169**

**August 1992**

Sponsored by

**U.S. DEPARTMENT OF COMMERCE  
NATIONAL INSTITUTE OF STANDARDS AND TECHNOLOGY  
BUILDING AND FIRE RESEARCH LABORATORY  
CENTER FOR FIRE RESEARCH**

## EXECUTIVE SUMMARY

An experimental and theoretical study of radiative feedback, burning rates, radiative heat loss fractions, and flame heights for pool fires with diameters ranging from 4.6 cm to 100 cm was completed. Transient measurements of soot and temperature distributions were obtained in 7.1 cm and 30 cm heptane and toluene fires using a three-wavelength emission/absorption probe. The heat release rates of the fires varied from 0.6 kW to 2166 kW allowing a study over a wide range. A variety of fuels were tried but most of the measurements were restricted to methanol, heptane, and toluene as representatives of the alcohols, paraffins and aromatics. Radiative feedback was measured using a new insitu purged optical probe inserted at the level of the fuel surface. Measurements of reflection of energy from the fuel surface were also obtained. A multi-ray radiation calculation procedure utilizing simultaneous single-point measurements of soot volume fractions and temperatures was used to estimate the heat transfer to the surroundings and that to the fuel surface. Importance of turbulent fluctuations of different frequencies on the radiation heat flux was studied using filtered simulations. Important conclusions of the present study are:

- (1) The total radiative heat loss fractions of several alcohol fuels were approximately 0.2 and those of paraffin and aromatic fuels were approximately 0.3 within the range of pool diameters and heat release rates,
- (2) Flame heights of alcohol and paraffin fuels were in reasonable agreement with existing correlations while those of aromatic fuels showed possible effects of lower combustion efficiency,
- (3) Burning rate measurements showed significant effects of fuel type for all pool diameters. For aromatic fuels such as toluene, the radiation dominated limit was reached at a relatively small pool diameter (between 5-7 cm). For heptane fires, the limit was reached at approximately four times the value for toluene. However, none of the pools in the present size range showed a clear conduction regime. The experiments at NIST with much smaller diameter pool flames conducted by Dr. John Yang should shed further light on this.
- (4) Radiative heat flux incident on the fuel surface was large (almost equal to the total heat feedback) for all the fuels for pool sizes above 30 cm near the pool center. For toluene fires, the heat flux remained high and almost constant as a function of radial distance. For heptane fires, the radiative feedback diminished a little with radius. However, for methanol fires, a significant decrease was observed with radius. It was found that the burning rate vs. pool diameter drop showing regimes of different heat transfer mechanisms is not consistent with insitu radiative heat feedback

measurements. Hence, the utility of such a map for fire-modelling should be reconsidered.

(5) Measurements of transient emission and absorption properties resolved to 10 mm show that:

- Large fluctuations in emission intensity and soot volume fractions occur in all regions of the flames.
- A layer of relatively cold soot particles exists near the fuel surface probably resulting from hydrodynamic transport from the edge of the fire.
- Comparison of measurements of soot volume fractions based on absorption with those based on emission shows that within a 10 mm long probe volume, a large portion of the soot particles are at relatively low temperatures and do not contribute to the emission.

(6) Calculations of radiation intensity and radiative heat flux using the time series of emission soot volume fractions and temperatures showed that:

- The 10 mm resolution offered by the present probe was sufficient for obtaining effective values of these properties.
- Use of mean values of temperature and soot volume fractions may result in an order of magnitude underestimate of radiation intensity and heat flux. However, due to the high sensitivity to temperatures, the error is normally corrected by using slightly higher average temperatures.
- Use of a Gaussian filter applied to the temperature and soot volume fraction time-series showed that relatively low frequency fluctuations in temperature and soot volume fractions contribute the most to the increase in radiation heat flux above that estimated from mean properties. The frequency above which the fluctuations appear to have minimal effects is close to the characteristic oscillation frequency of the fires.

(7) Predictions of radiative heat feedback and heat flux to surroundings using a multiray method showed that:

- The total heat flux changed by less than 15% between 22 and 450 rays.
- Reasonable comparison between predictions and measurements was observed.

The multi-ray procedure allows an examination of the regions of origin of the radiative heat feedback. It was observed that bulk of the feedback originated at heights below 0.5 D

in toluene fires, and at heights below 3.5 D in heptane fires.

The results of the present research are being applied by NIST personnel to the development of advanced global burning rate models. The multi-wavelength emission absorption probe has been used and improved by NIST researchers. The measurements have spurred activity in the areas of optical properties of soot, flame structure that leads to the relatively low temperature soot, utility of absorption vs. emission measurements, use of appropriate effective temperature from the fire, and evaluation of current entrainment rate correlations and data for compatibility with global fire models. Improvements in such models resulting from the knowledge gained in studies, such as the present work, are expected to contribute to long-term fire safety.

## List of Figures

	<u>Page</u>
CHAPTER I	
Figure 1-1	Surface energy balance..... 2
CHAPTER II	
Figure 2-1	Sketch of enclosure..... 8
Figure 2-2	Sketch of 4.6 and 7.1 cm burners..... 10
Figure 2-3	Sketch of 30, 60 and 100 cm burners..... 11
Figure 2-4	Sketch of the fuel supply and regulation system..... 13
Figure 2-5	Sketch of three wavelength optical pyrometer (path integrated)..... 15
Figure 2-6	Sketch of fuel vapor transmittance probe... 16
Figure 2-7	Apparatus for measurement of fuel surface reflectivity..... 17
Figure 2-8	Radiative heat fluxes as a function of axial distance for heptane flames..... 22
Figure 2-9	Radiative heat fluxes as a function of axial distance for methanol flame..... 23
Figure 2-10	Radiative heat fluxes as a function of radial distance for heptane flames..... 24
Figure 2-11	Radiative heat fluxes as a function of radial distance for methanol flames..... 25
Figure 2-12	Mean emission temperatures (path integrated) for toluene and heptane flames. 27
Figure 2-13	Mean absorption and emission transmittances for toluene and heptane flames..... 28
Figure 2-14	Visible flame heights as a function of heat release rate..... 29
Figure 2-15	Fuel burning rates as a function of heat release rate..... 33

## List of Figures (Cont.)

		<u>Page</u>
Figure 2-16	Flame emission at various wavelengths for toluene and heptane flames.....	34
Figure 2-17	Fuel vapor transmittance at various wavelengths for toluene and heptane.....	35
CHAPTER III		
Figure 3-1	Sketch of Feedback Radiometer.....	39
Figure 3-2.	Sketch of feedback radiometer traversing system.....	40
Figure 3-3.	Hemispherical coordinate system.....	42
Figure 3-4.	Directional radiative heat feedback as a function of angle and radial position in methanol.....	45
Figure 3-5.	Directional radiative heat feedback as a function of angle and radial position in heptane.....	46
Figure 3-6.	Distribution of directional radiative heat feedback at r=0 cm for heptane.....	47
Figure 3-7.	Distribution of directional radiative heat feedback at r=8 cm for heptane.....	48
Figure 3-8.	Radiative heat feedback as a function of radial position for methanol, heptane and toluene.....	50
Figure 3-9.	Normalized radiative heat feedback as a function of radial position for methanol, heptane and toluene (uncertainty $\pm 20\%$ )....	51
Figure 3-10.	Radiative heat feedback as a function of radial position for methanol in 60 and 100 cm burners.....	52
CHAPTER IV		
Figure 4-1.	Sketch of three wavelength emission/absorption probe.....	56
Figure 4-2.	Sketch of a radiation path and discretization grid for the equation of radiative transfer.....	62

## List of Figures (Cont.)

		<u>Page</u>
Figure 4-3.	Power spectral density of filtered white noise.....	64
Figure 4-4.	Radial distributions of mean and RMS wideband spectral radiation intensity at $\lambda=0.9$ and $1.0 \mu\text{m}$ for locations near the flame base.....	66
Figure 4-5.	Radial distributions of mean and RMS wideband spectral radiation intensity at $\lambda=0.9$ and $1.0 \mu\text{m}$ for locations near the flame tip.....	67
Figure 4-6.	Radial distributions of mean and RMS wideband spectral radiation intensity at $\lambda=0.632 \mu\text{m}$ for locations near the flame base.....	69
Figure 4-7.	Radial distributions of mean and RMS wideband spectral radiation intensity at $\lambda=0.632 \mu\text{m}$ for locations near the flame tip.....	71
Figure 4-8.	Radial distributions of mean and RMS two line emission temperatures for locations near the flame base.....	72
Figure 4-9.	Radial distributions of mean and RMS two line emission temperatures for locations near the flame tip.....	73
Figure 4-10.	Radial distributions of mean and RMS soot volume fractions based on emission and absorption data near the flame base.....	74
Figure 4-11.	Radial distributions of mean and RMS soot volume fractions based on emission and absorption data near the flame tip.....	75
Figure 4-12.	PDFs of emission intensity as a function of radial position at $x/D=0.8$ .....	78
Figure 4-13.	PDFs of emission intensity as a function of radial position at $x/D=0.8$ .....	79
Figure 4-14.	Predictions and measurements of monochromatic intensity ( $\lambda=1.0\mu\text{m}$ ) at $x/D=0.8$ .....	80

## List of Figures (Cont.)

	<u>Page</u>
Figure 4-15. Predictions of monochromatic intensity ( $\lambda=1.0\mu\text{m}$ ) using filtered emission intensity and soot volume fraction.....	81
Figure 4-16. Predictions of monochromatic intensity ( $\lambda=1.0\mu\text{m}$ ) using filtered emission temperature and soot volume fraction.....	83
Figure 4-17. Effect of cutoff frequency on predictions of monochromatic intensity ( $\lambda=1.0\mu\text{m}$ ).....	84
CHAPTER V	
Figure 5-1. Sketch of the rays and flame segments used in the calculations of radiative heat feedback.....	89
Figure 5-2. Radial distributions of measurements of mean and RMS temperatures based on emission at two wavelengths in a 30 cm toluene pool fire.....	92
Figure 5-3. Radial distributions of measurements of mean and RMS soot volume fractions based on absorption ( $\lambda=0.632\ \mu\text{m}$ ) in a 30 cm toluene pool fire.....	93
Figure 5-4. Radial distributions of measurements of mean and RMS soot volume fractions based on emission at two wavelengths in a 30 cm toluene pool fire.....	95
Figure 5-5. Measurements and calculations of hemispherical radiative intensity incident the liquid surface as a function of radial location and viewangle.....	96
Figure 5-6. Measurements and calculations of hemispherical radiative heat flux incident the surface of a 30 cm toluene pool fire as a function of radial location.....	97
Figure 5-7. Radial distributions of measurements of mean and RMS temperature based on emission at two wavelengths in a 30 cm heptane pool fire.....	99

## List of Figures (Cont.)

	<u>Page</u>
Figure 5-8. Radial distributions of measurements of mean and RMS soot volume fractions based on emission at two wavelengths in a 30 cm heptane pool fire.....	100
Figure 5-9. Measurements and calculations of hemispherical radiative heat flux incident on the surface of a 30 cm heptane pool fire as a function of radial location.....	101
Figure 5-10. Calculations of the contribution of radiative heat flux from different axial locations in 30 cm toluene and heptane pool fires.....	102

## TABLE OF CONTENTS

	<u>Page</u>
EXECUTIVE SUMMARY.....	iv
LIST OF FIGURES.....	vii
CHAPTER I INTRODUCTION.....	1
1.1 General Statement of the Problem.....	1
1.2 Related Studies.....	3
1.3 Overall Objectives.....	4
CHAPTER II GLOBAL FLAME PROPERTIES.....	6
2.1 Introduction.....	6
2.2 Experimental Methods.....	7
2.2.1 Experimental Apparatus .....	7
2.2.2 Instrumentation.....	12
2.2.3 Data Analysis.....	18
2.2.4 Operating Conditions.....	19
2.3 Results and Discussion.....	19
2.3.1 Radiative Properties.....	19
2.3.2 Effective Temperatures and Transmittances.....	26
2.3.3 Flame Heights.....	26
2.3.4 Fuel Burning Rates.....	30
2.3.5 Overall Energy Distribution.....	30
2.3.6 Spectral Fuel Vapor Transmittance and Flame Emission.....	32
2.3.7 Fuel Surface Reflection.....	32
2.4 Summary and Conclusions.....	32
CHAPTER III RADIATIVE FEEDBACK TO THE FUEL SURFACE.....	37
3.1 Introduction.....	37
3.2 Experimental Methods.....	38
3.2.1 Experimental Apparatus.....	38
3.2.2 Instrumentation.....	38
3.2.3 Data Analysis.....	41
3.2.4 Operating Conditions.....	43
3.3 Results and Discussion.....	43
3.3.1 Radiative Feedback in the 30 cm Burner.....	43
3.3.2 Radiative Feedback in 60 and 100 cm Burners.....	53
3.4 Conclusions.....	53
CHAPTER IV LOCAL EMISSION/ABSORPTION PROPERTIES.....	54
4.1 Introduction.....	54
4.2 Experimental Methods.....	55
4.2.1 Experimental Apparatus.....	55
4.2.2 Instrumentation.....	55

## Table of Contents (Cont.)

	<u>Page</u>
4.2.3 Data Analysis.....	58
4.2.3.1 Emission/Absorption Data.....	58
4.2.3.2 Turbulence-Radiation Interactions.....	59
4.2.3.3 Frequency Analysis.....	60
4.2.3.4 Frequency Content of Emission Properties.....	61
4.2.4 Operating Conditions.....	63
4.3 Results and Discussion.....	65
4.3.1 Mean and RMS Properties.....	65
4.3.2 Emission Statistics.....	77
4.3.2.1 Flame Properties.....	77
4.3.2.2 Turbulence Radiation Interactions.....	77
4.4 Conclusions.....	82
CHAPTER V PREDICTIONS OF RADIATIVE FEEDBACK.....	86
5.1 Introduction.....	86
5.2 Experimental Methods.....	87
5.2.1 Experimental Apparatus.....	87
5.2.2 Instrumentation.....	87
5.2.3 Data Analysis.....	88
5.2.4 Radiation Predictions.....	88
5.2.5 Operating Conditions.....	90
5.3 Results and Discussion.....	91
5.3.1 Toluene.....	91
5.3.2 Heptane.....	98
5.4 Conclusions.....	103
CHAPTER VI SUMMARY AND CONCLUSIONS.....	104
6.1 Summary.....	104
6.2 Conclusions.....	104
6.3 Recommendations for Further Research...	104
APPENDICES: TABULATED DATA	
APPENDIX A Fuel Property Data.....	107
APPENDIX B Total Radiative Output.....	108
APPENDIX C Directional Radiative Feedback.....	118
APPENDIX D Emission/Absorption Properties.....	122
APPENDIX E Spectral Emission, Fuel Vapor Transmission and Fuel Surface Reflection Properties.....	130
REFERENCES.....	134

## Chapter I Introduction

### 1.1 General Statement of the Problem

Radiation from liquid fueled flames is an important heat transfer mechanism in combustion systems such as fires, furnaces and gas turbine combustors. Radiative heat flux from fires to the surrounding objects determines the possibility of ignition, flame spread and flashover. Burning rates of objects on fire determine safe egress times, heating rates of surrounding objects and flame spread rates. Knowledge of the mechanisms that determine the burning rate and radiative heat flux of fires has been sought since early days of fire science (Hottel, 1958).

deRis (1979), Mudan (1984) and Quintiere (1992) have reviewed past work concerning burning rates and radiation properties of pool fires. Existing methods of calculating radiation from liquid fueled fires are based on homogeneous, isothermal flame approximations and an effective average flame temperature and emissivities. The effect of the differences in the structure of the flames generated by different fuels are considered only in a global manner in this approach. Effects of turbulent fluctuations on radiative transfer are not explicitly considered. Motivated by these observations, the overall objective of the present investigation was to study the radiation properties of liquid fueled diffusion flames.

The study concentrated on axisymmetric diffusion flames from circular burners containing liquid fuels. The main research issues addressed here are: (1) total radiative output of liquid fueled flames; (2) radiative heat transfer to the fuel surface; (3) local emission and absorption properties of strongly radiating pool flames; and (4) the significance turbulence-radiation interactions in buoyant turbulent luminous pool flames. Particular emphasis was placed on the mechanism of radiative heat transfer to the fuel surface, termed radiative heat feedback, in luminous flames where the continuum radiation properties depend on local soot volume fractions and temperatures.

The burning rate of pool fires is determined by the rate at which energy is transferred to the liquid fuel. Fig. 1-1 shows the energy balance at the fuel surface of a liquid pool fire.  $Q_{fb}$  is the energy from the flame incident on the fuel surface,  $Q_{cond}$  is the energy conducted into the fuel by the burner walls,  $mH_{fg}$  is the total latent heat of vaporization, and  $Q_{cond-loss}$  is the energy conducted through the fuel layer. The energy feedback term  $Q_{fb}$  involves radiation, convection, and conduction from the hot flame gases to the liquid fuel surface. This term proves to be difficult to characterize since turbulence and radiation are often involved in the mechanisms.

As discussed in the literature reviews cited above, the related studies cited in the next section and the literature

# SURFACE ENERGY BALANCE

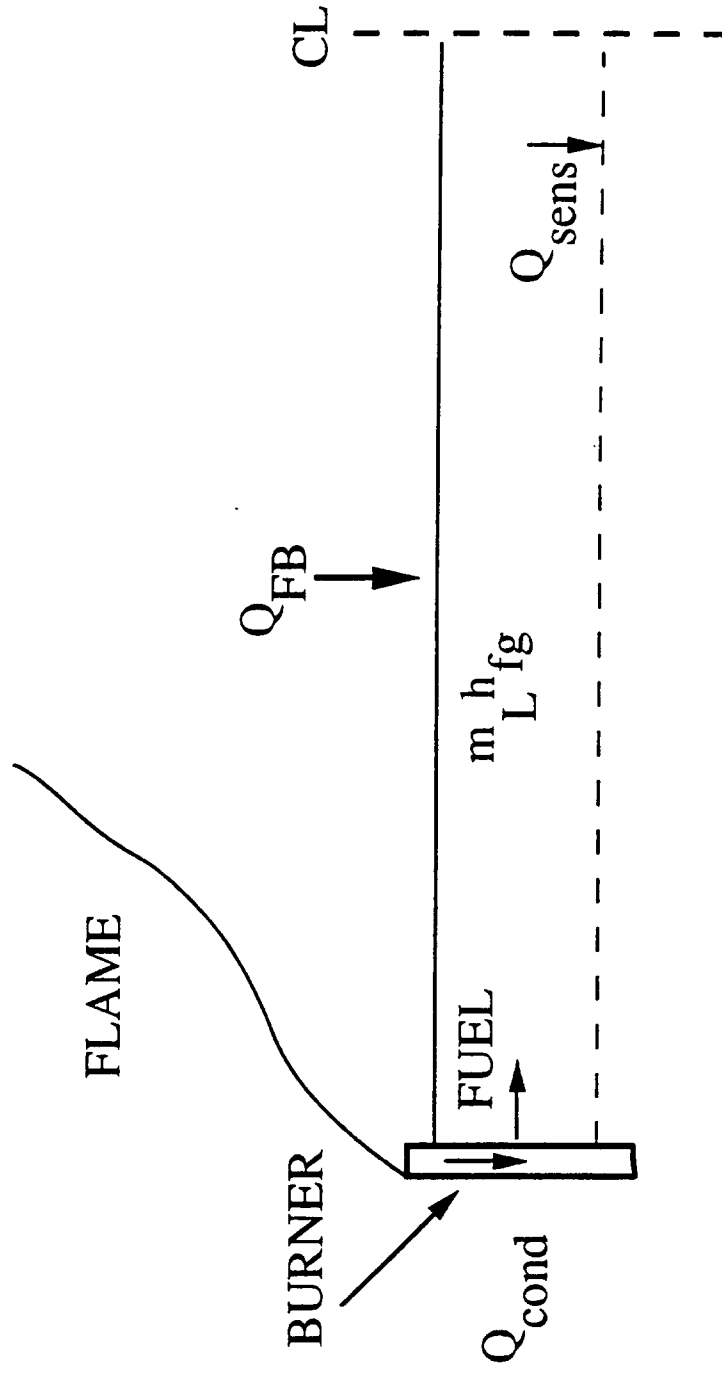


Fig. 1-1 Surface energy balance

reviewed in the introductory sections of each of the following chapters, there are specific breaches in our understanding of the effects of fuel properties, burner size and sooting tendency on heat transfer from the flames to the liquid surface (heat feedback). Information concerning the relative contribution of radiative and convective processes to the heat feedback is lacking. Furthermore, the effect of transient local flame structure (distribution of scalar properties such as species concentrations that affect emissivity and temperature) on heat feedback has not been quantified. In situ measurements of the heat feedback and the local, transient scalar properties are lacking for many fuels of interest.

The present work addresses some of these gaps. The main technical application of this research is to develop a fundamental understanding of the continuum radiation properties in luminous diffusion liquid fueled flames, particularly with regard to the mechanism of heat feedback. The results have application to modelling fires within structures, material characterization and test methods and fire detection systems.

## 1.2 Related Studies

Past work in radiation from pool fires has been reviewed by deRis (1979), Mudan (1984) and Fischer (1988). These reviews provide descriptions of the approximate radiation calculations methodologies and experimental data concerning pool fires. Fernandez-Pello (1991) and Quintiere (1992) have reviewed the fundamental mass and energy transfer processes in pool burning. Faeth et al. (1989) and Fischer (1988) have reviewed the effects of fluctuating scalar properties in flame radiation. Background material on radiation in pure and particle laden gases is provided by Siegal and Howell (1981), Ludwig et al. (1973), Goody (1964) and Hottel and Sarofim (1967).

Burgess and Hertzberg (1974) and Blinov and Khudiakov (1957) have shown that for certain fuels, the radiative feedback is dominated by conduction below a pool size of 10 cm diameter, between a pool size of 30-50 cm diameter convection is important and above this range the fires become radiatively dominated. For large fires, the relative contribution of radiative and convective heat flux may also depend on the position on the pool surface due to changes in flame shapes and convective velocities.

In non-luminous flames, energy is radiated from gases such as  $\text{CO}_2$ ,  $\text{CO}$  and  $\text{H}_2\text{O}$ . Edwards and Menard (1964) developed wide band exponential models to predict the emission from radiating gases which has been used successfully by Negrelli et al. (1977) and Liu et al. (1981) in laminar methane/air flames. Grosshandler and Sawyer (1978) examined the non-luminous spectral radiation properties of methanol/air combustion products. This study used a statistical narrow-band model to make encouraging predictions in the post-flame region.

Several recent studies have made transient measurements of radiation and flow field properties of pool fires. The results of these studies indicated the fluctuating nature of the scalars in all regions of pool fires. McCaffrey (1979) measured velocity and temperature distributions in natural gas pool fires. This study identified the various flow regions within a pool fire. Weckman and Sobiesiak (1989) studied the entrainment mechanism in medium scale acetone pool fires. Bouhafid et al. (1989) measured temperature, gas species concentrations and monochromatic absorption coefficients near the fuel surface of kerosene pool fires. They identified the fluctuating nature of scalars in pool fires. Fischer and Grosshandler (1987) measured time-averaged compositions of radiating gases and soot, and fluctuating temperatures in alcohol pool fires. Shinotake et al. (1985) made transient measurements of heat feedback in heptane pool fires.

The effects of scalar fluctuations on luminous radiation have been shown to be significant. Mean property methods that are frequently used to compute radiation intensities underestimate the mean radiation intensity. This has been noted by Cox (1977), Faeth et al. (1988), Gore and Faeth (1986, 1987), Kabshinov and Kmit (1979) and Portscht (1974). Stochastic simulations following the time series analysis methods of Box and Jenkins (1976) have been successfully applied to fully turbulent jet flames by Kounalakis et al (1988a,b). Sivathanu et al. (1991) and Sivathanu and Gore (1991) have shown that the joint statistics of temperature and soot volume fractions are necessary for obtaining reasonable predication of radiation intensity in strongly radiating flames.

### **1.3 Overall Objectives**

The present study seeks to improve the understanding of radiation from liquid fueled pool flames by addressing some open research issues. These include:

1. The effect of fuel type and scale on mass burning rates and flame radiation;
2. The mechanism of radiative heat transfer in pool fires;
3. Local emission/absorption properties of luminous pool fires; and
4. Turbulence-radiation interactions in prediction of radiative feedback in luminous pool fires.

Chapter II describes the global properties of all the flames studied in the present investigation. The global properties include mass burning rates, flame heights and radiative heat loss fractions. Chapter III describes the measurements of radiative heat feedback to the fuel surface in medium sized pool flames. Chapter IV reports the measurement of local emission/absorption properties in a small scale strongly radiating pool flame. The fluctuating nature of emission scalars is investigated. Chapter V describes

measurements of emission/absorption properties in a medium scale pool fire and the use of these properties in the prediction of radiative heat feedback.

## CHAPTER II GLOBAL FLAME PROPERTIES

### 2.1 Introduction

Pool fires are generally luminous and emit radiation due to both soot and combustion products. The energy radiated from the flames is an important parameter in fire safety. The amount of heat flux directly contributes to the hazard posed by the flame and the spread rate of the fire.

A number of experimental studies have considered the total radiant heat loss from gaseous turbulent and laminar diffusion flames (Markstein, 1984; deRis, 1979; Faeth et al, 1989; Gore, 1986; Sivathanu, 1990; and Gore et al, 1991). Markstein (1984) found that the radiative heat loss fraction is a constant for highly buoyant turbulent flames, as opposed to laminar gaseous flames for which the radiative fraction increases until the smoke point (defined as the fuel flow rate at which visible dark smoke is just emitted at the flame tip) is reached. Jeng and Faeth (1984) report the radiant heat loss from methane flames both in buoyant and in the forced regimes. Subsequent studies (Gore, 1986; Sivathanu, 1990) support the experimental finding that for low speed turbulent flames burning a variety of fuels (acetylene, carbon monoxide, methane, ethylene, propane, propylene, and ethylene), the radiation losses are a constant fraction of the chemical energy release.

Past measurements of radiant heat loss from liquid and solid fueled flames have generally relied on single location measurements. This method assumes that the radiative heat flux from flames is spherically isotropic:

$$Q_{rad} = 4\pi R^2 q'' \quad (2-1)$$

where R is the radius of the sphere and  $q''$  is the radiative flux at the measurement location on the sphere. Modak and Croce (1977) used this method for estimating the radiative heat loss fraction from PMMA. Koseki and Yumoto (1988) measured the radiant heat loss for large scale heptane fires relying on single point measurements. Bouhafid et al. (1989) measured radiative heat flux at various distances from pool fires and calculated the heat loss fraction. Recently, Köylü and Faeth (1991) have reported measurements of radiative loss fractions for 0.1 (m) diameter flames stabilized on a porous matrix.

The objective of this portion of the investigation was to determine the total radiative output of liquid-fuel pool flames at a range of scales burning a variety of fuels. Faeth and co-workers (Jeng and Faeth, 1984; Gore, 1986; and Sivathanu 1990) utilized a multi-location method for radiant heat flux measurements in gaseous diffusion flames. This technique, used in the present investigation, avoids the assumptions used in single point measurements, and had not been utilized in previous studies of liquid and solid fueled

flames.

Additionally, measurements of effective temperature and transmittances were made for two flames of different sooting tendency. Measurements of the spectral flame emission and spectral fuel vapor transmittance were made for heptane and toluene. Measurements of flame heights and fuel burning rates were also made.

## **2.2 Experimental Methods**

### **2.2.1 Experimental Apparatus**

The experiment involved the burning of liquid fuels from a circular pan in a quiescent room environment. The flames were operated in a large enclosure, the location and size of which varied due to the large range of burner diameters which were used in the study. A sketch of the general characteristics of the enclosures is shown in Fig. 2-1. The enclosure utilized wire mesh screens and/or plastic sheets to minimize effects of room disturbances on flame shape and other flame properties. Each facility employed an adjustable exhaust system to remove combustion gases and soot from the enclosure. The burners were mounted rigidly and was placed approximately 15 cm above ground level.

Pool burners of inner diameter 4.6, 7.1, 30, 60, 100 cm were used. Other relevant dimensions of the burners are given Table 2-1. The 4.6 and 7.1 cm burners (Fig. 2-2) were uncooled and constructed from pyrex and included ports from which fuel could be delivered and a thermocouple could be installed.

The larger burners were made of rolled steel and are depicted in Fig. 2-3. Each burner contained several ports in the base for delivery of fuel and installation of thermocouple arrays. A cooling water reservoir was placed on the bottom of the steel pan and was fed cold tap water throughout each test. Incoming and out-going cooling water temperatures were monitored throughout the test by chromel/alumel thermocouples connected to a data acquisition computer. The thermocouple arrays consisted of individual thermocouples which were placed at different distances relative to the burner lip. The output of these thermocouples provided a temperature profile of the fuel in the liquid phase.

Fuel burning rate was monitored using a load cell mounted under the fuel supply reservoir. In a few trials with the smaller pools (4.6 and 7.1 cm), a 75 ml burette and stop watch were used and the burning rates manually recorded. The output of the load cell was collected by a data acquisition computer. The uncertainty of the load cell data is estimated to be 5% based on repeated measurements and calibrations. The uncertainty of the burette data is estimated to be 10%.

Preparation for the tests began with activation of the cooling water. Sufficient time was allowed for the cooling water temperature to stabilize. The burner was filled until the fuel level was approximately 1 cm below the edge. The

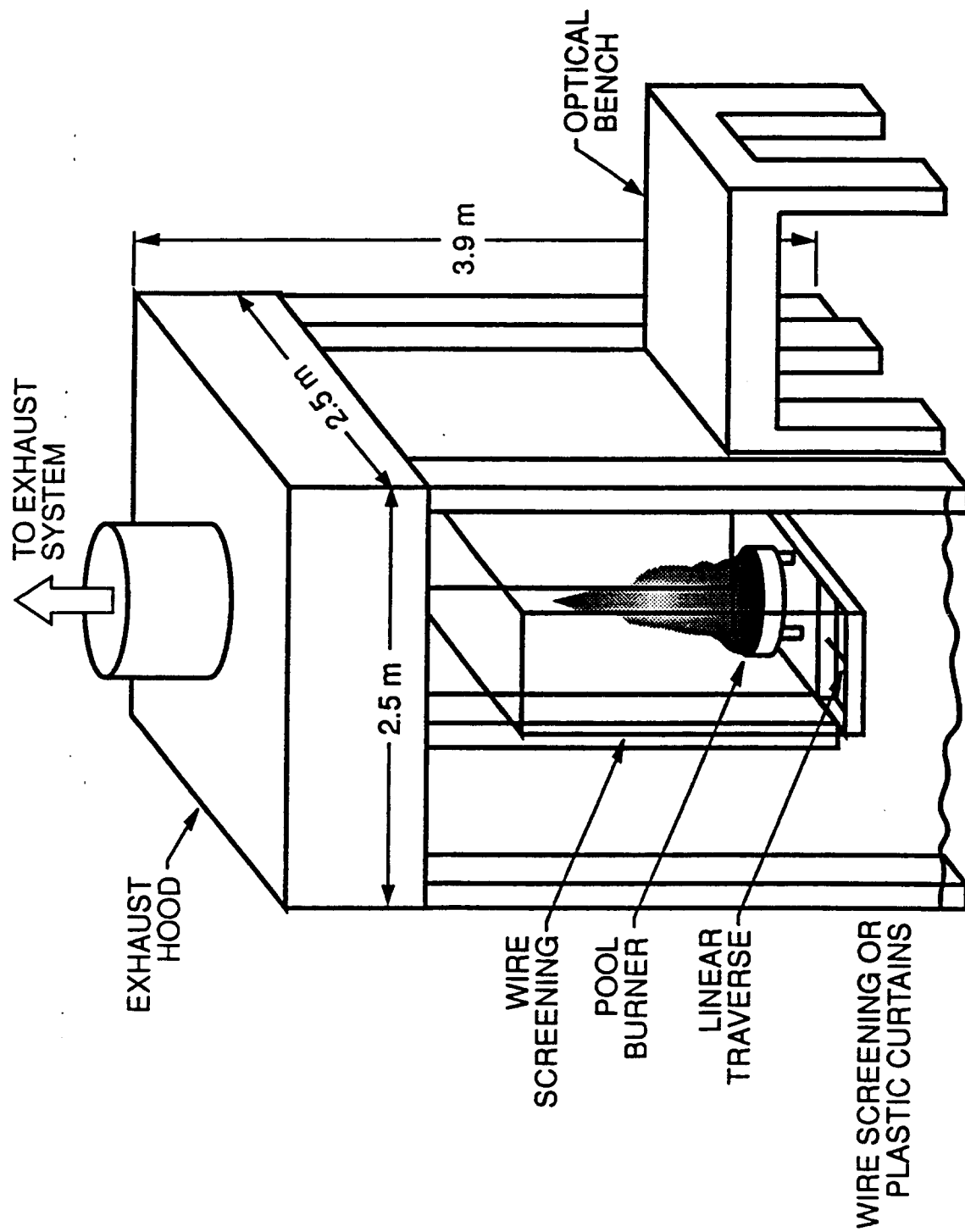


Fig. 2-1 Sketch of enclosure

BURNER INNER DIAMETER (cm) D	BURNER DEPTH (cm) A	BURNER WALL THICKNESS (cm) t	BURNER MATERIAL
4.6	8.0	0.32	PYREX
7.1	10.0	0.32	PYREX
30	15.2	0.16	STAINLESS STEEL
60	10.2	0.16	STEEL
100	10.2	0.16	STEEL

Table 2-1 Burner Dimensions

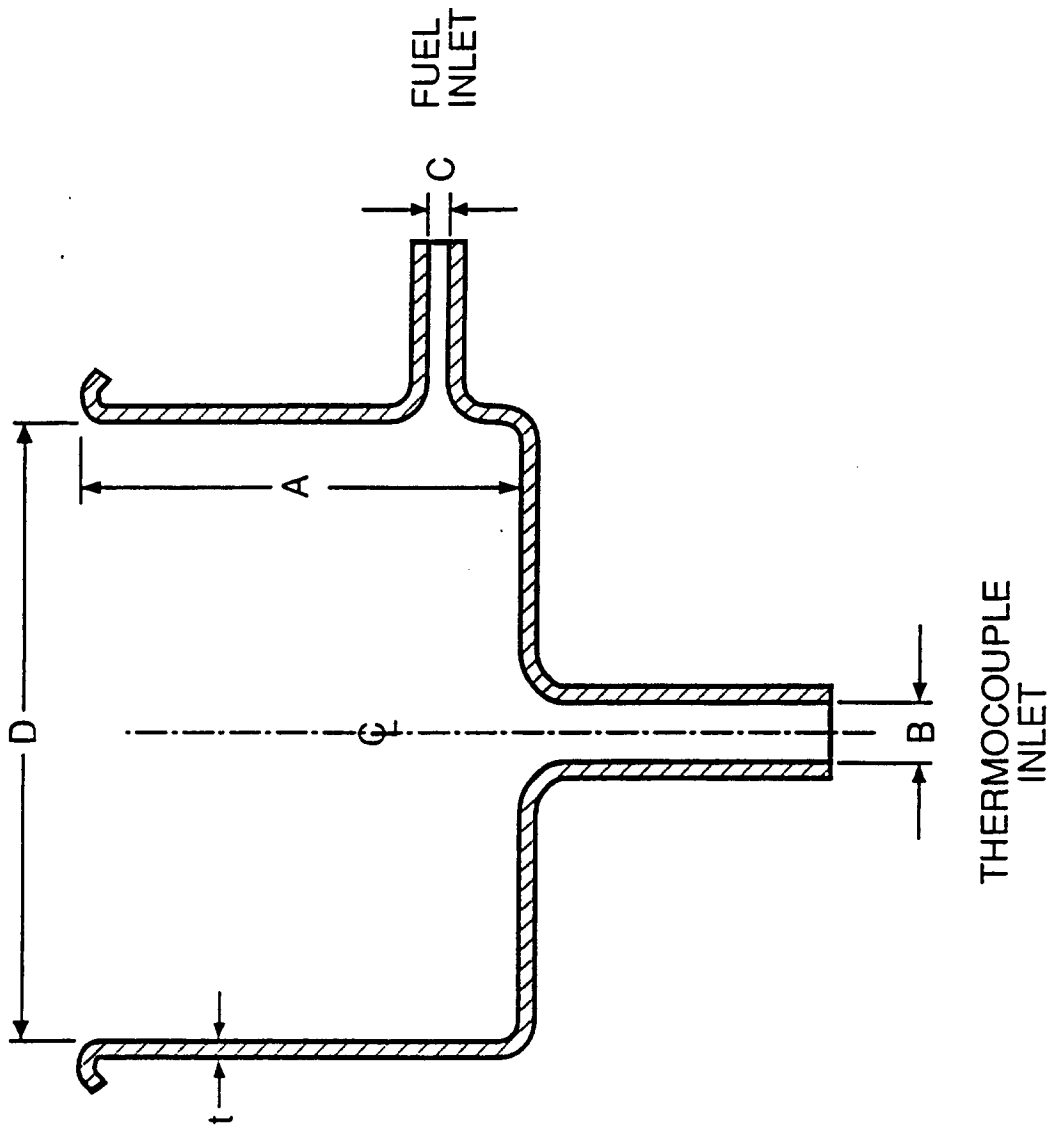


Fig. 2-2 Sketch of 4.6 and 7.1 cm burners

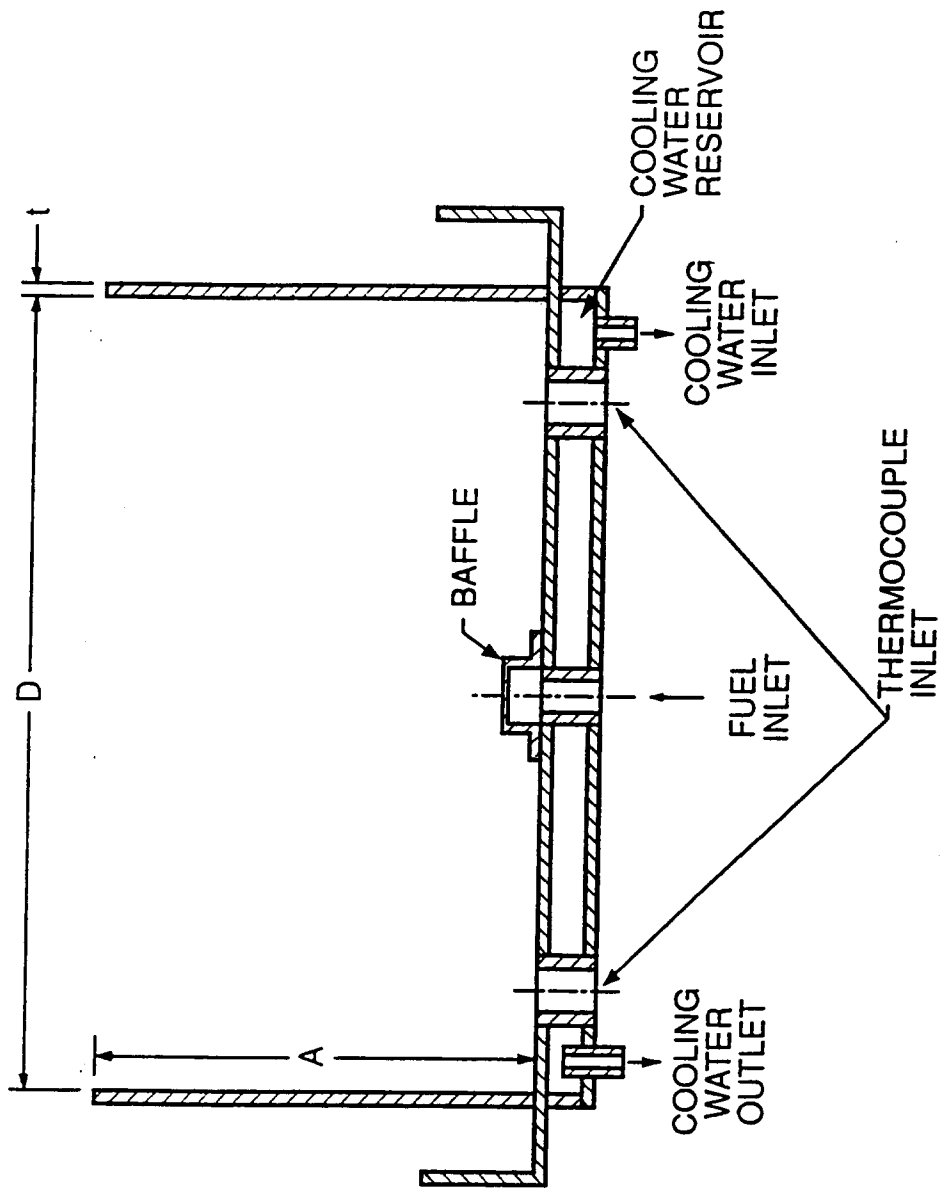


Fig. 2-3 Sketch of 30, 60 and 100 cm burners

fuel reservoir was filled and any air in the fuel line was bled out. The regulating and solenoid valves were shut and exhaust system activated. After ignition, the exhaust system was adjusted so that combustion products were removed but the flame shape was unaffected. The fuel regulating valves were adjusted to maintain the fuel at the required level.

The fuel level was maintained constant relative to the burner lip during the entire test. The level was 5 mm below the edge for the larger burners ( $D \geq 30$  cm) and 3.5 mm below the edge for the smaller burners. The level control was accomplished using a gravity feed fuel system which utilized a fine adjustment regulating valve and a temperature-controlled solenoid valve. The control system is depicted in Fig. 2-4. The solenoid valve controller received input from a thermocouple placed just above the liquid fuel surface. The solenoid valve is activated open when the temperature rises above a prescribed value and shuts when the temperature limit is again reached. The regulating valve controls the rate at which fuel enters the burner, preventing (along with the baffles placed at the bottom of the burner) disturbances of the fuel surface by the incoming fuel.

Data collection began only after a warm-up period of at least 10 minutes. This allowed for the fuel in the pan and the surroundings to attain a relatively steady temperature. Obtaining acceptable flame shapes (negligible amount of flame lean) became more difficult as the scale increased. This was true even with the enclosures described previously. Much effort was made to attain axisymmetric, uniformly attached, vertical flame shape with minimum room disturbances during the warm-up period. The effort involved placement of screens and baffles and adjustment of exhaust flow rate to achieve desirable conditions. In the larger scale tests ( $D > 30$  cm), the fuel height in the burner was varied slightly (5 - 15 mm) in order to maintain reasonable flame shapes. This was necessary for heptane and toluene as fuel vapor would occasionally ignite in the over flow ring on the burner if the fuel level was at 5 mm.

### 2.2.2 Instrumentation

Flame heights were obtained from video tapes (30 frames/sec) and still photographs. The luminous flame heights were obtained by averaging approximately one hundred frames selected at random. When necessary and possible, room lighting was dimmed and dark backgrounds were used to enhance the quality of the video and stills. Distances on the film and video were calibrated by photographing scales. Experimental uncertainties for these measurements depended on the room lighting, flame luminosity and film sensitivity. For a specific set of these conditions, the uncertainties were less than 10% but could be as high as 40% for different tests.

A calibrated radiative heat flux transducer was used to measure total radiative heat fluxes. The method used to determine total radiative heat flux is identical to that Gore (1986) and Sivathanu (1990). The transducer(s) used were water cooled and provided a  $120^\circ$  to  $150^\circ$  viewing angle. The

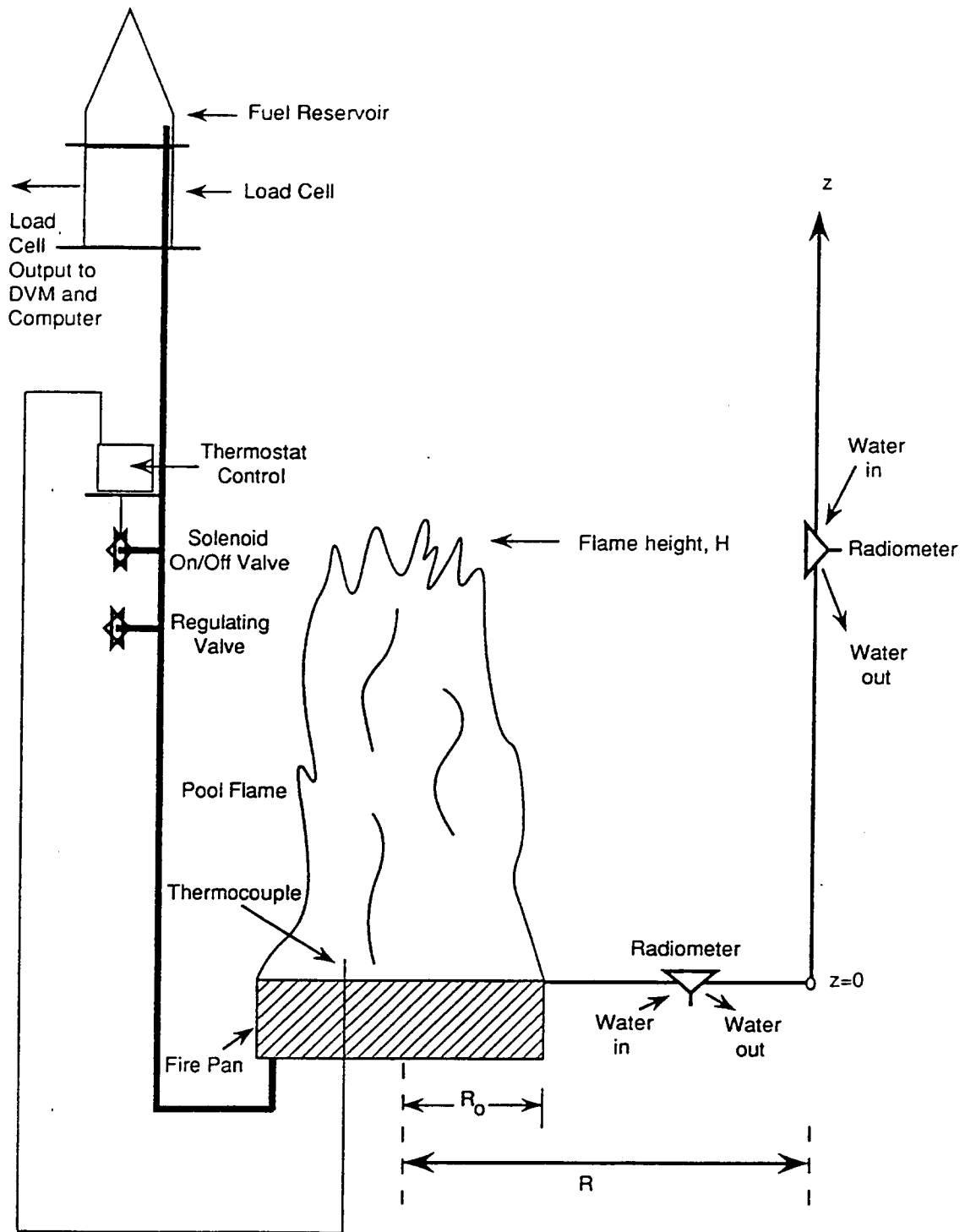


Fig. 2-4 Sketch of the fuel supply and regulation system

radiant heat flux incident on locations on the burner plane and also on locations parallel to the flame axis was measured.

In the burners with diameters less than 30 cm, a single heat flux transducer was traversed both radially and axially to capture the radiant energy. In the larger sized pools, test times were generally much shorter due the large amount of fuel consumed. In these tests, an array of transducers was used. The transducers were fixed in place in both the radial and axial directions. The transducers were calibrated using a known standard transducer and a tungsten lamp source. Experimental uncertainties for the total radiant output measurements are estimated to be less than 15 percent based on repeated tests.

Effective temperatures and transmittances were measured by using three wavelength optical pyrometry. A schematic of the experimental apparatus is shown in Fig. 2-5. The technique consists of the simultaneous measurement of flame emission intensities at two wavelengths ( $\lambda = 0.9$  and  $1.0 \mu\text{m}$ ) and laser transmission ( $\lambda = 0.632 \mu\text{m}$ ) across the entire width of the flame. The light leaving the flames is collected by a 0.6 cm diameter, 25 cm long stainless steel tube that has a nitrogen purge of 1 cc/min. A second tube with identical purge flow serves as the cold background for the measurement and also as the guide for the incident He-Ne laser used for the transmittance measurements. Two beam splitters are used to divide the light into three parts. Focussing lenses and line filters with 10 nm bandwidth on each channel complete the optics. The emission detectors are two photomultiplier tubes and the transmittance detector is a laser power meter. The incident laser power is monitored by an identical detector. All signals are sampled by a laboratory computer at 250 Hz.

Spectral fuel vapor transmittance is measured using the experimental apparatus shown in Fig. 2-6. Two probes, defining a 10 mm path length, are placed at a position in the flame where little emission and soot is present ( $x/D = 0.01$ ). Blackbody radiation transmission is monitored through the probes. A 1/8 m grating monochromator is used to determine the spectral content of the transmission signal. A Pb-S or Pb-Se detector is utilized depending on the wavelength of interest. The detection signal is sampled by a laboratory computer.

Spectral flame emission is measured for a path length that encompasses the entire width of the flame. A 1/8 m grating monochromator defines the wavelength interval of interest and a Pb-S or Pb-Se detector is used for the measurement. An appropriate optical edge filter is used to prevent measurement of harmonics. The signal is monitored by a laboratory computer at 250 Hz. The detectors are calibrated at each wavelength by a blackbody radiation source.

Fuel surface reflection of incident infrared radiation ( $\lambda = 1.0 - 3.0 \mu\text{m}$ ) is measured using the apparatus depicted in Fig. 2-7. An alignment laser is used to position the mirrors and infrared detector(s) and measure the incident radiation

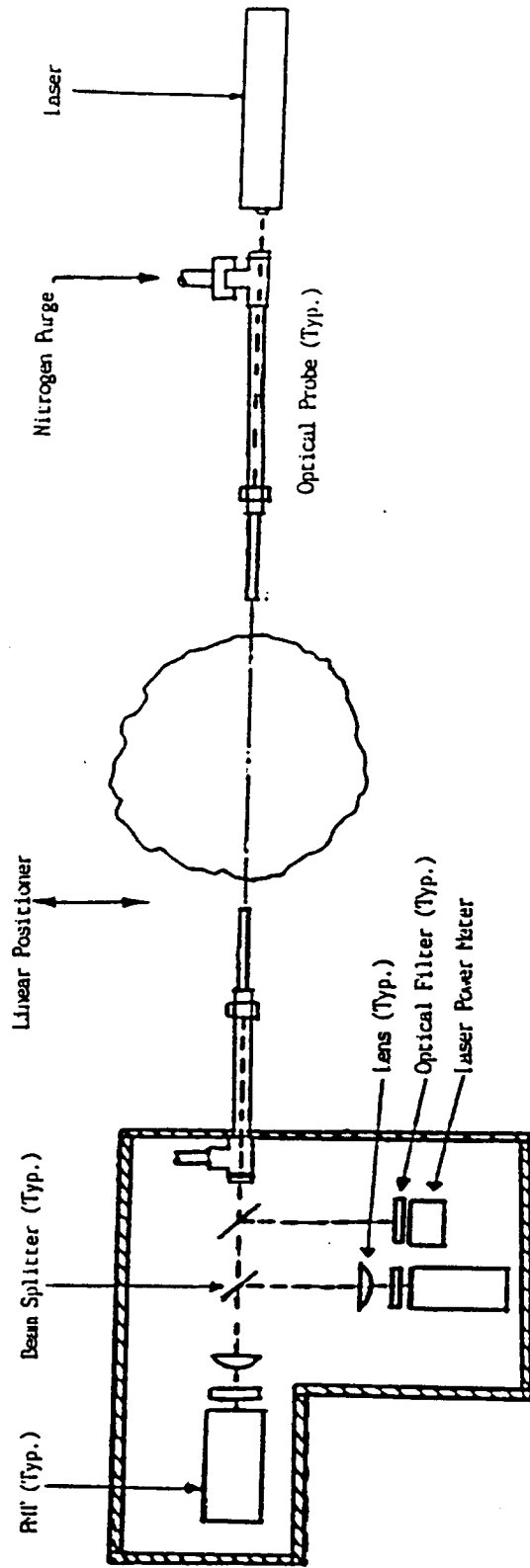


Fig. 2-5 Sketch of three wavelength optical pyrometer (path integrated)

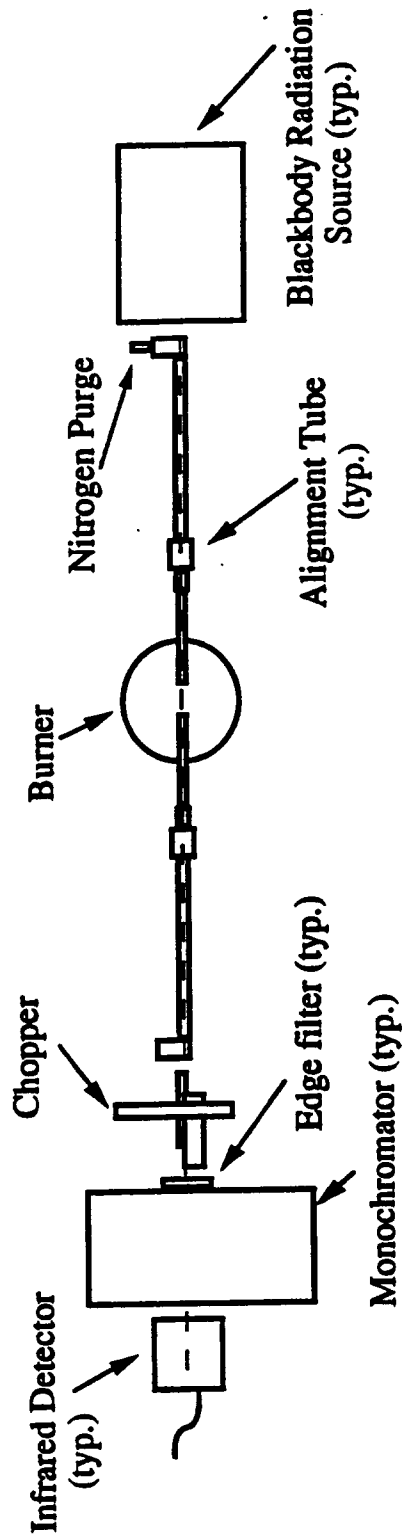


Fig. 2-6 Sketch of fuel vapor transmittance probe

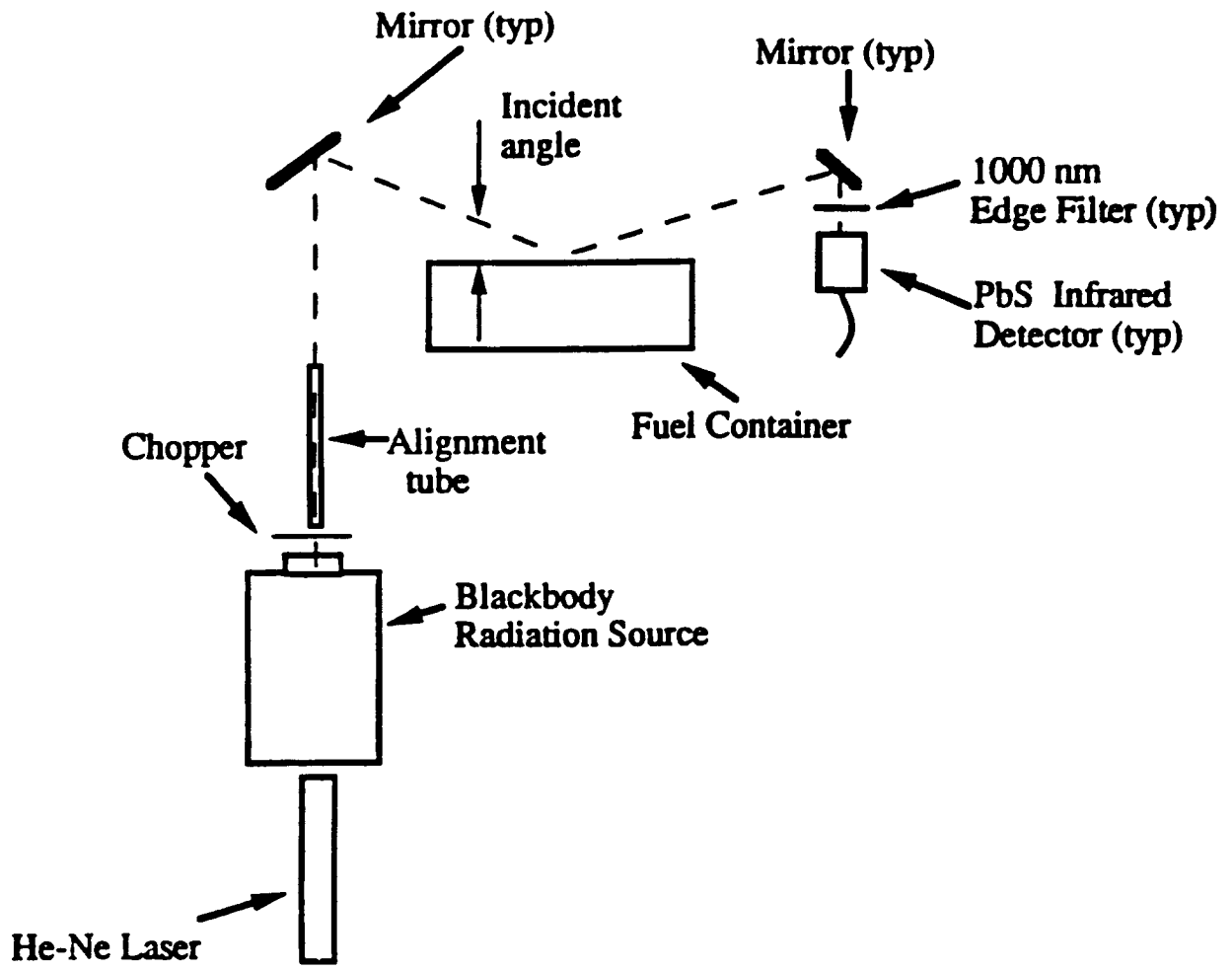


Fig. 2-7 Apparatus for measurement of fuel surface reflectivity

angle. Infrared radiation from a blackbody source is colimated used 6 mm diameter tubes. The detector signal is measured with the use of a lock-in amplifier and a laboratory computer.

### 2.2.3 Data Analysis

The radiative heat flux was measured in a direction normal to the plane of the fuel surface at the burner plane for a distance R and then in a direction perpendicular to the flame axis (see Fig. 2-4). These measurements were extended in the axial direction until close to background flux were found. Radiation incident on the pool surface were assumed equal to value measured just outside the burner. The radiant flux distributions are integrated to enclose the flame in a "semi-infinite" cylinder (see Hamins et al. (1991)), thus providing the total radiative energy ( $Q_{rad}$ ) of the flame. The radiative heat loss fraction ( $X_R$ ) is defined as:

$$X_R = Q_{rad} / Q_{chem} \quad (2-2)$$

where  $Q_{chem}$  is the fuel burning rate ( $m_b$ ) multiplied by the ideal heat of combustion ( $H_c$ ).

The ratio of laser intensity after passing through the flame and the initial laser intensity is known as the transmittance through the flame:

$$\frac{I_\lambda}{I_{\lambda_0}} = e^{-\frac{K_\lambda}{\lambda} \int_0^s f_v ds} = \tau_{\lambda_a}(s) \quad (2-3)$$

Under the present approximations, the transmittance is related to the volume fraction and the refractive index of soot along the radiation path. The refractive index of soot is assumed to be independent of temperature and fuel type. There is controversy in the literature concerning the temperature dependence of refractive index of soot [Sivathanu, et al. (1991)]. However, variation with temperature and fuel type is not seen for a majority of the measurements. Therefore, a constant value (1.55- 0.56i) of refractive index given by Dalzell and Sarofim (1969) is used in the present study. With this value,  $K_\lambda$  is set at 4.89. The laser absorption measurements are used to calculate  $\tau_{\lambda_a}$  using Eqn. 2-2.

Radiation intensities leaving the flame at the two wavelengths ( $\lambda = 0.9$  and  $1.0 \mu\text{m}$ ) are related to the distribution of soot volume fractions and temperatures along the narrow radiation path selected by the long receiving tube by:

$$I_\lambda = \int_1^{\tau_\lambda(s)} I_{\lambda_b} d\tau_\lambda = (1 - \tau_{\lambda_0}(s)) I_{\lambda_b}(T_e) \quad (2-4)$$

ere the local transmittance  $\tau_\lambda(s)$  is defined by Eqn. 2-2 and  $I_{\lambda_b}$  is the black body intensity at the local temperature: <sup>wh</sup>

$$I_{\lambda_b} = \frac{2hc^2}{\lambda^5 (e^{hc/\lambda k_b T} - 1)} \quad (2-5)$$

It is noted that the intensity leaving the radiation path at

the two emission wavelengths defined by Eqn. 2-3 depends on the soot volume fraction distribution along the path weighted by the local Planck's function  $I_{\lambda b}$ . The  $K_{\lambda}$  is 5.33 at  $0.9 \mu\text{m}$  and 5.59 at  $1.0 \mu\text{m}$  based on the refractive index for soot.

Equivalent radiation temperature ( $T_e$ ) and emission transmittance ( $\tau_{\lambda e}$ ) for the radiation path are defined as shown in Eqn. 2-4. Using the measurements of intensity at the two wavelengths, Eqns. 2-4 are solved for  $T_e$  and  $\tau_{\lambda e}$ , assuming that the reciprocal wavelength dependence of Eqn. 2-3 is applicable to  $\tau_{\lambda e}$ . For an isothermal path,  $T_e$  is equal to the actual temperature and  $\tau_{\lambda e}$  is identical to  $\tau_{\lambda a}$  after correcting for the wavelength dependence of the absorption coefficient. For a non-isothermal path, Sivathanu et al. (1991) found that the  $T_e$  is close to the peak soot temperature along the path. If a large portion of the soot particles along the path are at temperatures close to  $T_e$ , then  $\tau_{\lambda e}$  is similar to  $\tau_{\lambda a}$ . On the other hand, if  $\tau_{\lambda a}$  is much larger than  $\tau_{\lambda e}$ , a large portion of the soot particles are at relatively low temperatures.

#### 2.2.4 Operating Conditions

The operating conditions for the present tests are summarized in Table 2-2. The general flame shapes were typical of pool fires with the flame width equal to that of burner at the lowest regions of the flame and then necking in toward the pool center at some distance above the burner. The fuels of similar composition, such as fuels classified as parafins, aromatics or alcohols, generally have comparable flame shapes. The alcohol fuels generally necked in just above the burner lip and the parafin and aromatic fuels had a larger distance before necking begins. All flames exhibited large scale pulsations characteristic of buoyancy dominated flows (Pagni, 1989). The parafin and aromatic flames formed soot particles at all scales, which is characterized by yellow luminous radiation. The alcohols contained no measurable soot, though the ethanol and hexanol flames did exhibit faint visible luminosity. Methanol flames exhibit only radiation from the combustion gas bands and burned with a bright blue color. Toluene (an aromatic), heptane (a parafin), and methanol (an alcohol) were selected as representative fuels for more detailed study. These three fuels represent a wide range in sooting tendency.

### 2.3 RESULTS AND DISCUSSION

#### 2.3.1 Radiative Properties

Measurements to determine the radiative heat loss fraction for a variety of fuels yielded extensive information on the distribution of radiative heat fluxes to the surroundings. Measurements of radiant heat flux incident on the plane of the burner lip in the radial direction and incident in the axial direction at a fixed distance from the burner center are presented (see Fig. 2-4). As expected, the overall magnitude of the radiant heat fluxes varied with both fuel and scale. However, the trend of the data was remarkably similar for all fuels and scale. The general trends are shown for both luminous and non-luminous flames in the following

FUEL	D (cm)	R/R <sub>0</sub>	m" (kg/m <sup>2</sup> -s)	Q" (KW/m <sup>2</sup> )	Q <sub>chem</sub> (KW)	H <sub>t</sub> (cm)	X <sub>R</sub>
METHANOL	7.1	9.3	0.0131	16	1.2	27.9	0.20
	30	5.5	0.0130	15	20	50.8	0.18
	60	8.6	0.0134	16	84		0.17
	100	6.6	0.0144	17	252	135	0.12
ETHANOL	4.6	16	0.0138	14	0.6		0.20
	7.1	10	0.0127	11	1.4	19.0	0.17
HEXANOL	7.1	12	0.010	8.5	1.5	16.0	0.21
HEPTANE	4.6	16	0.0186	9.1	1.4		0.27
	7.1	11	0.0230	11	4.0	34.5	0.29
	30	5.5	0.0362	18	116	131	0.31
	60	8.6	0.0566	27	770		0.36
	100	8.8	0.0655	32	2480	341	0.28
MMA	7.1	10	0.0250	12	2.4	24.6	0.33
	30	13	0.0367	17	72	96.0	
TOLUENE	4.6	16	0.0318	16	2.2		0.32
	7.1	11	0.0404	21	6.7	30.4	0.31
	30	13	0.0431	22	125	130	
	60	8.6	0.0768	40	892		0.36
	100	8.8	0.0671	34	2166	274	0.24
STYRENE	4.6	16	0.0325	17	2.2		0.31
	7.1	10	0.0353	19	5.6	36.3	0.31
TOLUENE + ETHANOL	7.1	12	0.0170	15	2.2	25.4	0.32

Table 2-2 Test Conditions for Liquid Fueled Pool Flames

figures. Fig. 2-8 shows the distribution of axial heat fluxes for heptane at three different scales. Fig. 2-9 shows the axial fluxes of methanol for at the same three scales. The non-dimensional axial radiative heat fluxes,  $(q'' \cdot R^2)/Q_{\text{chem}}$ , are shown as a function of axial distance normalized by the flame height ( $x/H_f$ ). The maximum flux was found at a relatively low axial position at all scales. The data collapses until  $x/H_f \approx 0.8$  beyond which scatter is seen. This trend that shows that radiative heat flux did correlate well with total heat release of the flame for luminous and non-luminous flames until the magnitudes of the heat flux data are low. Hamins et al. (1991) found that measurements of total radiative heat loss based on single location measurements were most accurate when made in the range of  $x/H_f = 0.2$  to  $0.6$ . This corresponds to the location where the heat flux values at different scales collapse when normalized using this method.

The radial heat fluxes for heptane and methanol at several scales are shown in Fig. 2-10 and Fig. 2-11. The radial radiative heat flux is normalized by the square of the distance from the burner center divided by the total chemical energy of the flame  $(q'' \cdot (r-D/2)^2)/Q_{\text{chem}}$ .  $(r-D/2)$  is used as the length scale for the radiative flux since  $\pi(r-D/2)^2$  represents the area on the radial plane to which the flame radiates. The radial distance from the pool center is normalized by the flame height ( $r/H_f$ ). The heptane data collapse along a single curve for all flames considered until the heat flux magnitudes become low. The methanol radiative heat flux do not collapse well. However, the magnitudes of the flux are low in this region.

The radiative heat loss fractions,  $X_r$  (the fraction of total chemical energy of flame lost as radiation) were found to be nearly constant for a particular fuel, and relatively independent of burner size (Table 2-2). This property has been seen in other highly-buoyant flames (deRis, 1979). Furthermore, each classification of fuel, i.e. parafin, aromatic or alcohol, also tend to have a constant radiative heat loss fraction, regardless of fuel or scale. The parafin and aromatic fuels generally lose approximately 30% of their energy as radiation while the alcohols lose approximately 20%. Flames burning an azeotropic mixture of toluene and ethanol had an  $X_r$  between the two groups.

The relatively constant radiative heat loss fraction for the various fuels was quite surprising in light of the tremendous differences in sooting tendency of the hydrocarbon fuels. For example, the soot production for toluene and heptane varied by an order of magnitude (Gore et al. 1991). Soot continuum radiation contributes much to the radiant output of flames, but the radiant energy released by the flames and the burning rates of the fuels vary by less than 50% at any one scale. If all the soot present in the flame was contributing the flame emission, the total radiant output and the fuel burning rates should also vary by approximately an order of magnitude for optically thin flames. This will further investigated by path integrated measurements of

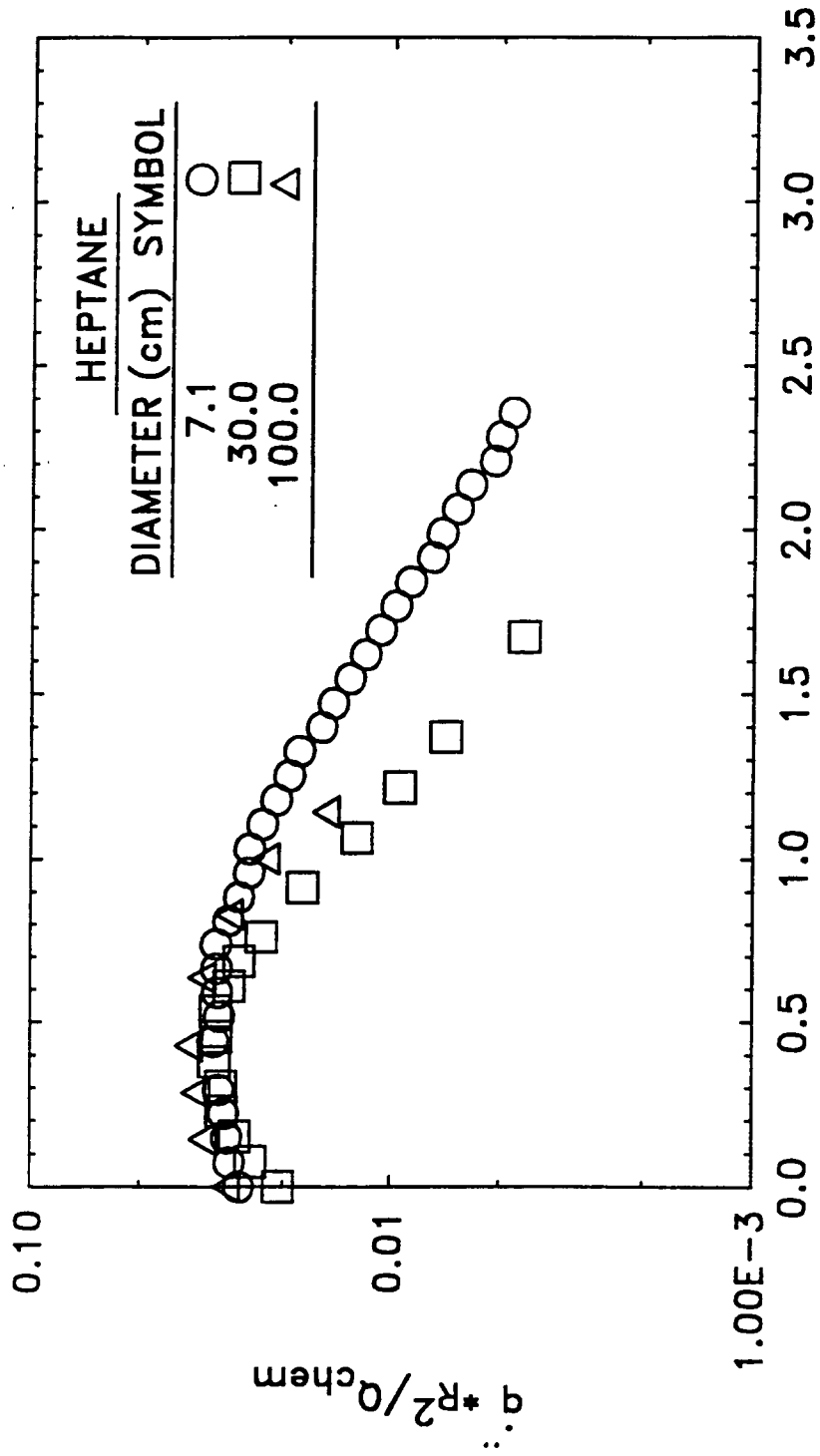


Fig. 2-8 Radiative heat fluxes as a function of axial distance for heptane flames

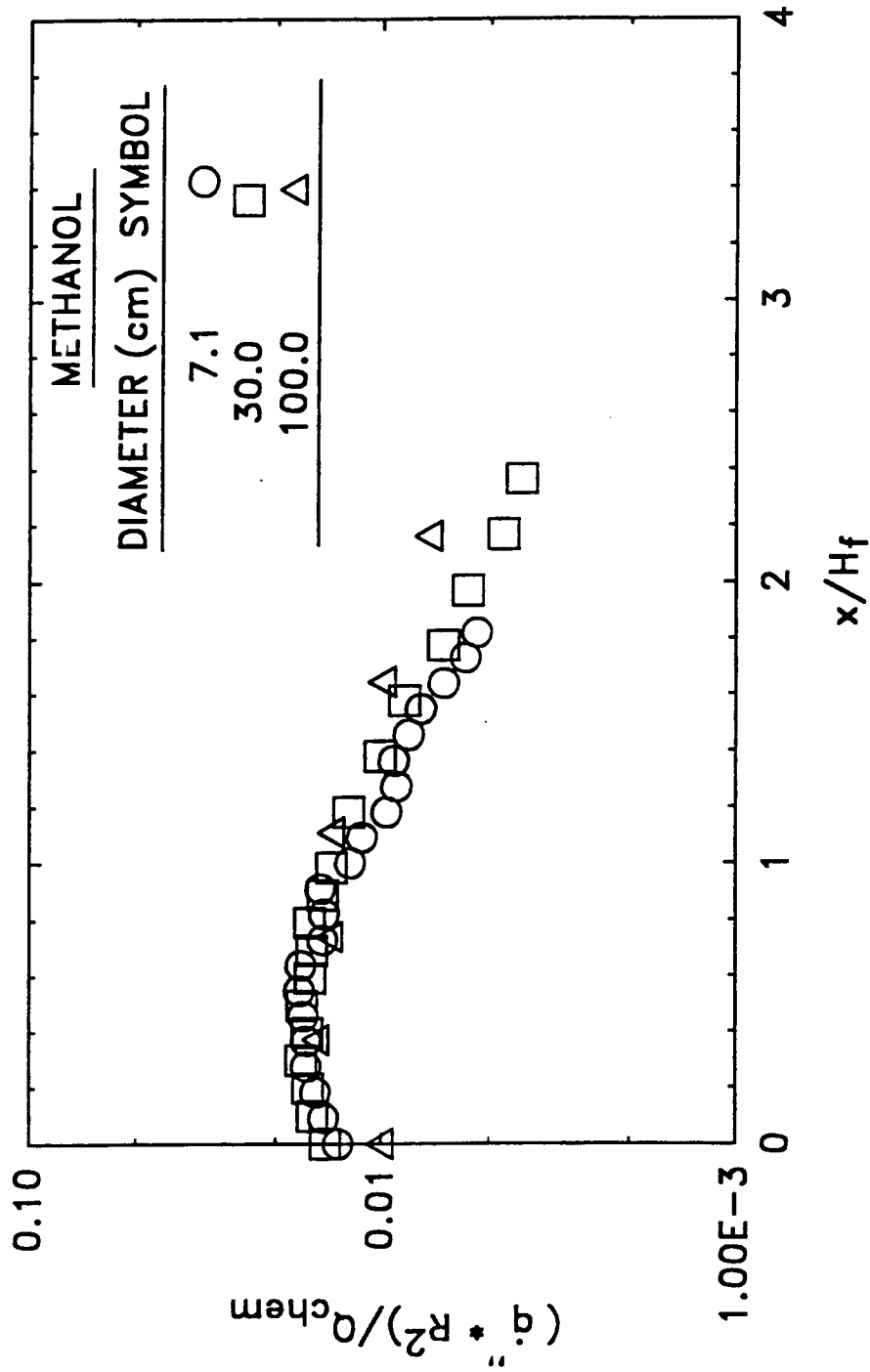


Fig. 2-9 Radiative heat fluxes as a function of axial distance for methanol flames

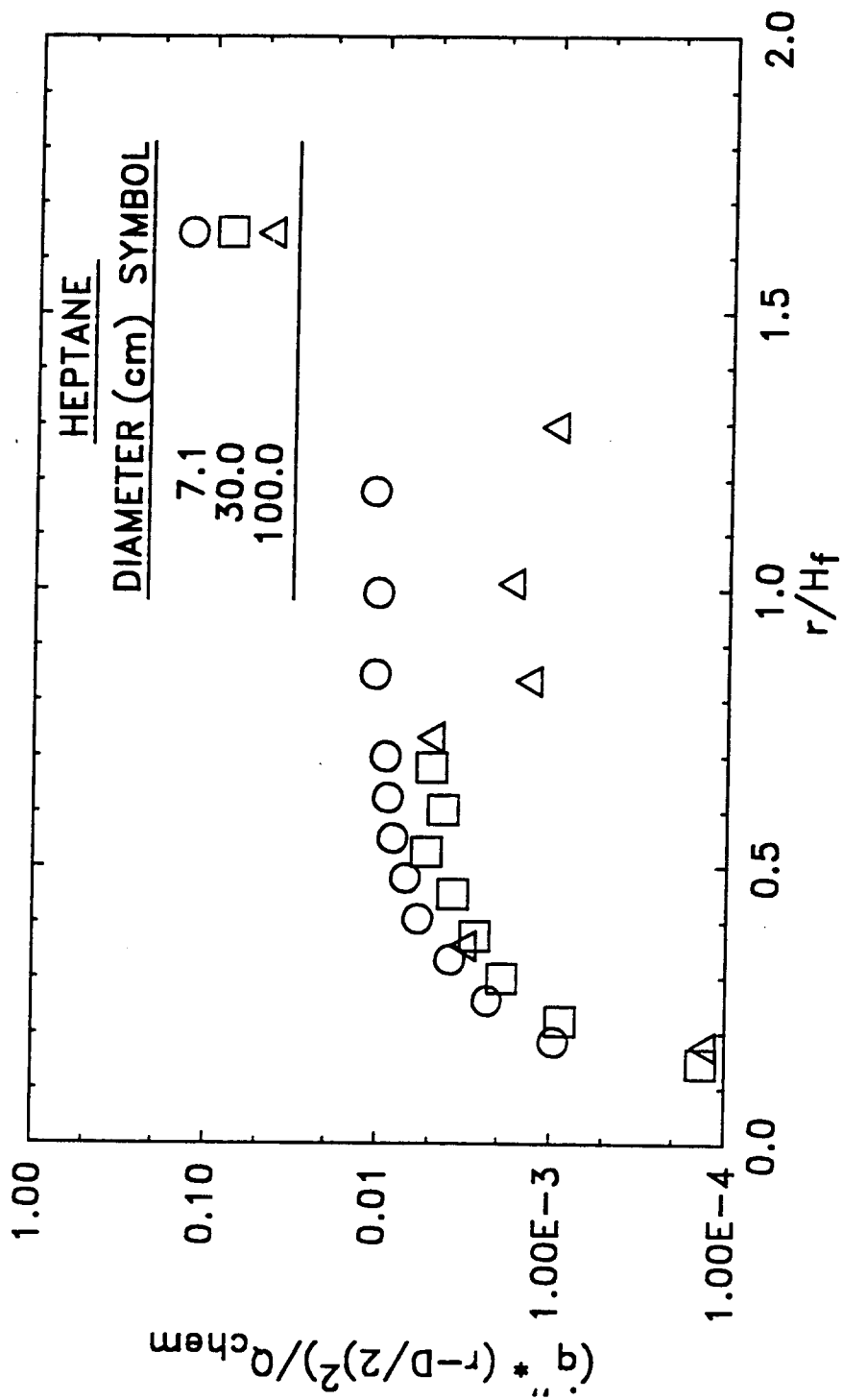


Fig. 2-10 Radiative heat fluxes as a function of radial distance for heptane flames

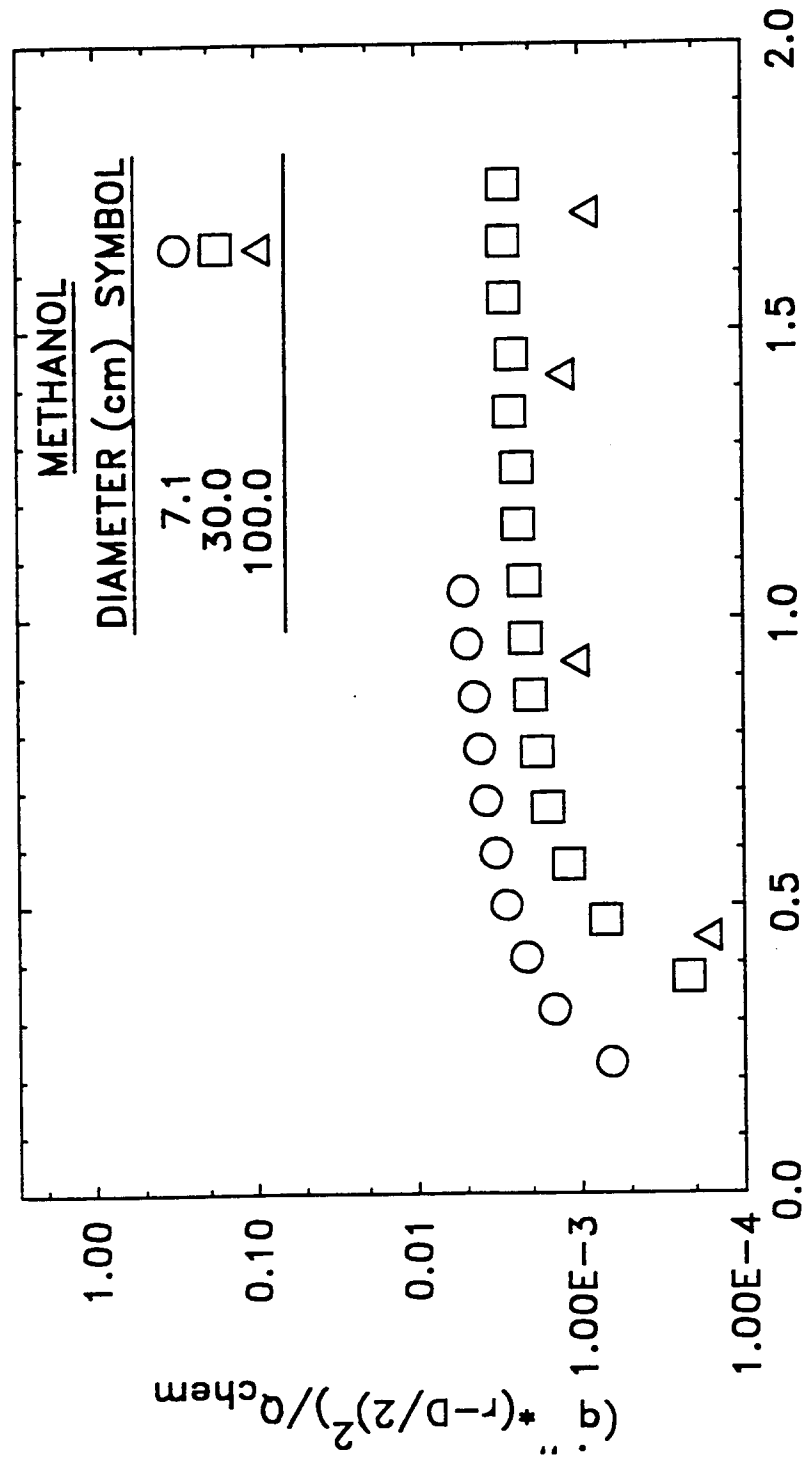


Fig. 2-// Radiative heat fluxes as a function of radial distance for methanol flames

radiation temperature and transmittance.

### 2.3.2 Effective Temperatures and Transmittances

Measurements of radiation temperature and effective absorptive and emissive transmittance were made for heptane and toluene flames from the 7.1 cm burner. The mean emission temperatures for the two flames are plotted as a function of normalized distance from the fuel surface in Fig. 2-12. As noted in section 2.2.3, these temperatures are close to the peak temperatures across the entire diametric radiation path. For approximately half the flame height, the temperatures in the toluene flame are lower by approximately 200 K than those of the heptane flame. The adiabatic flame temperature (assuming complete combustion) for toluene is approximately 150 K higher than that for heptane. The observed temperatures indicate incomplete and non-adiabatic combustion. Since the radiative heat loss fraction for the two fuels are close, the differences in the temperatures can not be attributed to the differences in radiative cooling but are consequence of the reduced combustion efficiency of toluene as compared to heptane.

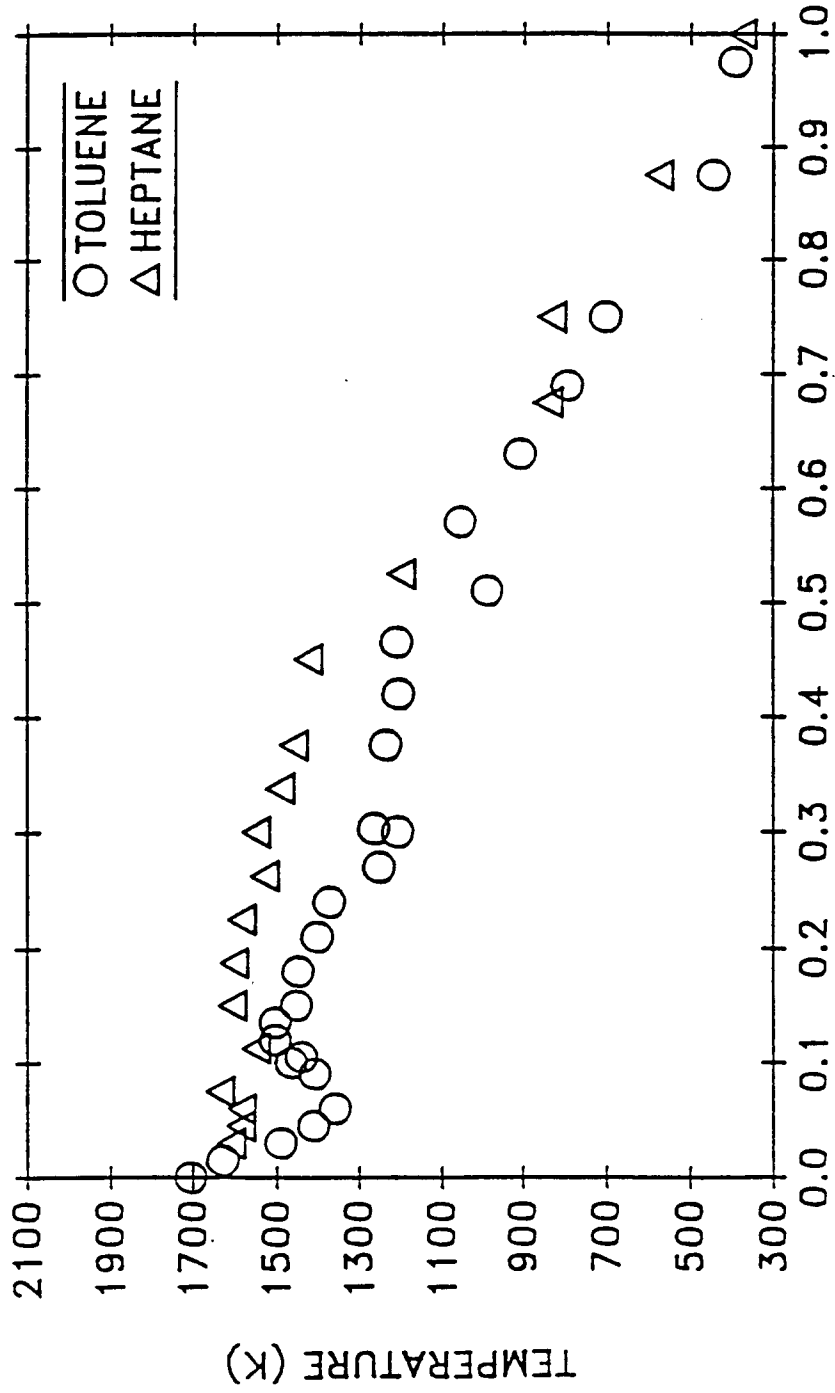
Fig. 2-13 shows the absorption and emission transmittances for the two flames plotted as a function of normalized axial distance. The measurements of  $\tau_{\lambda a}$  show that the toluene flames are optically thick with a transmittance of less than 5% at certain locations and generally less than 30% at all locations. Based on both  $\tau_{\lambda a}$  and  $\tau_{\lambda e}$ , the heptane flames are optically thin with transmittances greater than 70% for all locations. The differences between  $\tau_{\lambda a}$  and  $\tau_{\lambda e}$  for the heptane flames are relatively small suggesting that large portions of the soot particles in this flame contribute to the radiation intensity. In contrast, the differences between  $\tau_{\lambda a}$  and  $\tau_{\lambda e}$  for the toluene flame vary by a factor of 4 to 10. This observation suggests that a large portion of the soot particles in the toluene flames are at relatively low temperatures and do not contribute significantly to the radiation intensity. Sivathanu et al. (1990) found that a large percentage of soot present in strongly radiating acetylene/air jets was relatively "cold" and not contributing to flame emission. The existence of large quantities of cold soot in the toluene flames helps explain the relatively small increase in  $X_R$  and heat feedback for fuels of different sooting tendencies.

### 2.3.3 Flame Heights

Visible flame heights for the test flames in the present study are plotted in Fig. 2-14 and tabulated in Table 2-2. Flame heights measurements from the 4.6 cm and 60 cm burners were not made in this study. The results are plotted according to the scaling relationships proposed by Zukoski et al. (1984) with  $H_f/D$  as a function of normalized heat release rate ( $Q_{chem}/d^{5/2}$ ). Data for a variety of buoyant diffusion flames from gaseous, liquid and solid fuels (Thomas, 1962; Steward, 1970; Terai and Nitta, 1975; McCaffrey, 1979; You and Faeth, 1979; Zukoski et al., 1984; and Sivathanu, 1990) are plotted as solid lines in Fig. 2-14.

# AXIAL TEMPERATURE PROFILE

7.1 cm BURNER INTEGRATED PATH



X/H<sub>f</sub>

Fig. 2-12 Mean emission temperatures (path integrated) for toluene and heptane flames

EFFECTIVE TRANSMITTANCES  
7.1 CM BURNER PATH INTEGRATED

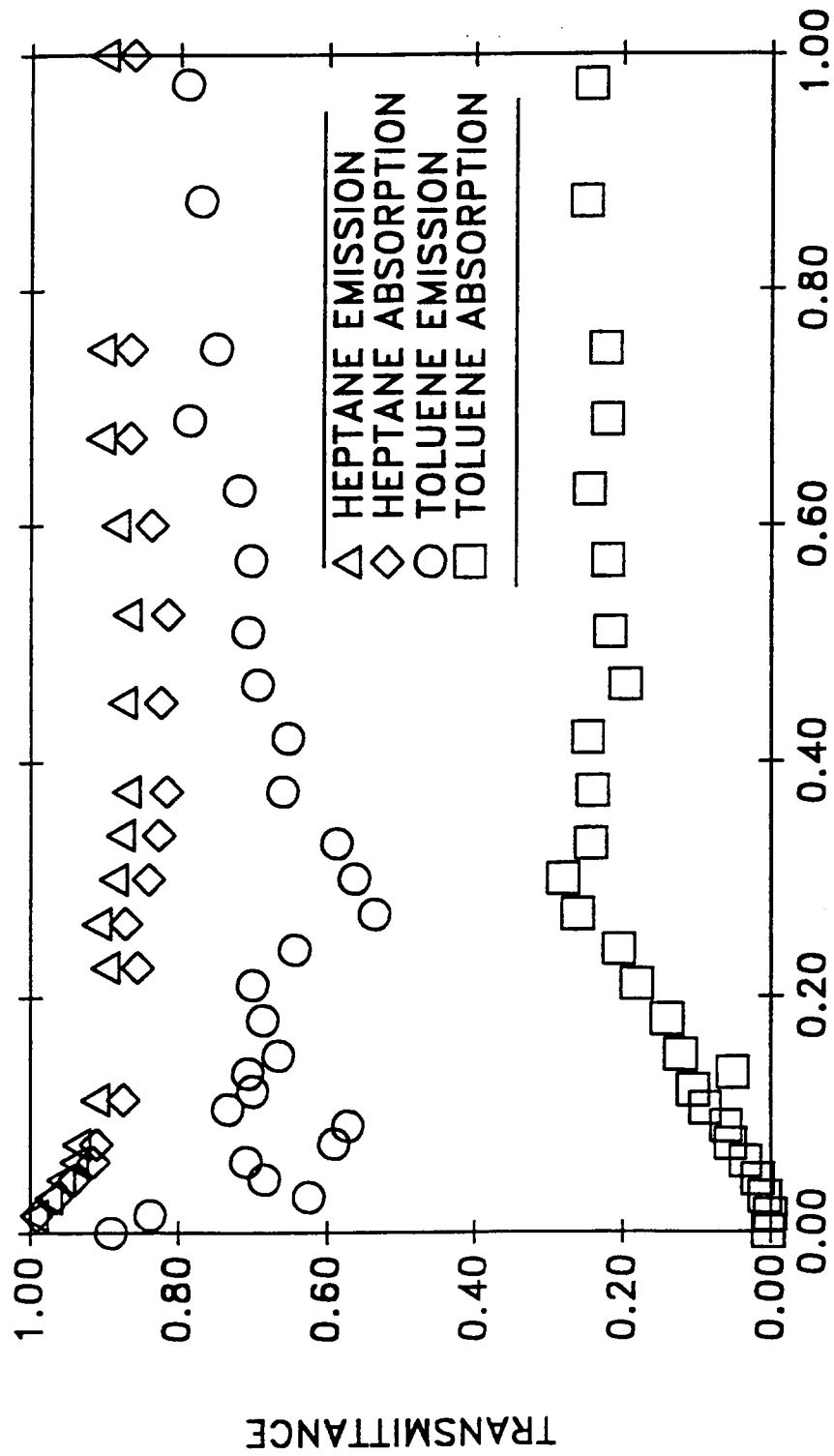


Fig. 2-13 Mean absorption and emission transmittances for toluene and heptane flames

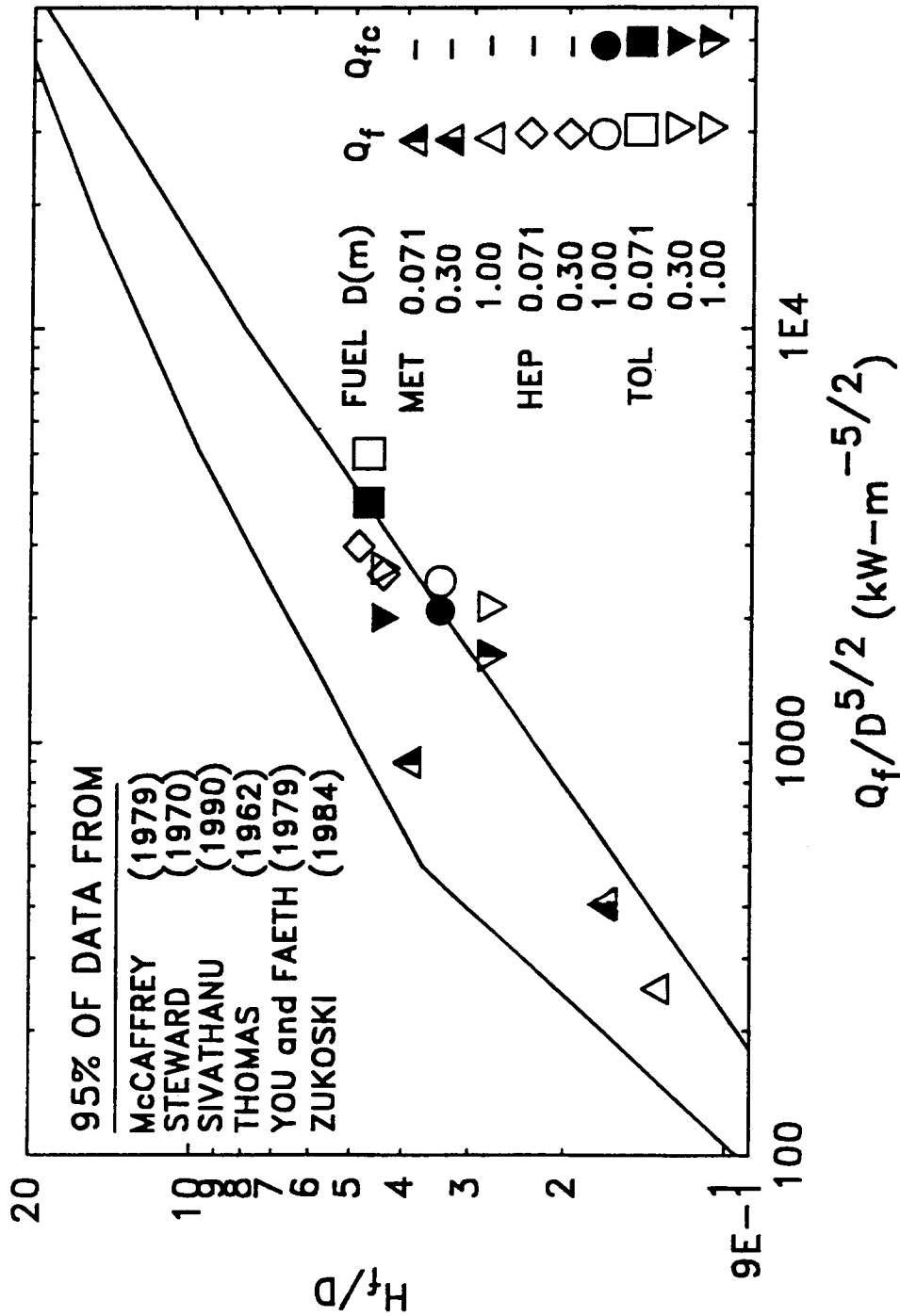


Fig. 2-14 Visible flame heights as a function of heat release rate

The flame heights for methanol are characterized very well by this normalization and agree with the data from other investigators. The flame heights from heptane measured in this study are in the lower portions of the correlation for  $D = 7.1$  and  $30$  cm. The flame height for heptane at  $D = 100$  cm and the normalized toluene flame heights at all scales do not correlate well as a function of normalized heat release when ideal heat of combustion is considered. This may be due to the low combustion efficiency of toluene (0.76 according to Mulholland et al., 1988) which is not taken into account by the correlation. If the toluene flame heights are corrected for combustion efficiency ( $Q_{fc}$  in Fig. 2-14), agreement with correlations from the literature improves. Additionally, blockage of the upper regions of the toluene flame by soot release (especially at  $D = 100$  cm) made accurate flame height measurements difficult.

#### 2.3.4 Fuel Burning Rates

Fuel burning fluxes for many of the present test flames are shown in Fig. 2-15 and tabulated in Table 2-2. The fuel burning rates have been plotted as a function of the burner diameter. As described previously, a constant fuel height was maintained in the burners during measurements.

Several researchers have compiled fuel burning rate data versus diameter for a variety of fuels (e.g. Barbasukas, 1983; Hamins et al., 1992). Burning rate data of Corlett and Fu (1966) for methanol and Koseki and Yumoto (1988) for heptane are included in Fig. 2-15 for reference. Corlett and Fu (1966) maintained a constant fuel level relative to the burner rim. An increase of mass burning flux at the smaller diameters ( $D > 3$  cm) has been found by other investigations (e.g. Blinov and Khudiakov, 1957). This may be due to the enhanced effect of conduction from the burner material to the fuel or laminar convection at small diameters. This effect was not studied in the present investigation. At larger diameters, the alcohol fuels show very little variation in burning flux rate with diameter.

The parafin and aromatic fuels show an increased mass burning flux with diameter. This was attributed the increased importance of radiative heat feedback to the fuel surface as the pool diameter increases (Blinov and Khudiakov 1957, Hottel, 1958). Koseki and Yumoto (1988) allowed the fuel level relative to the burner rim to decrease with time. This may explain the systematic difference between their burning rate data and the present study.

#### 2.3.5 Overall Energy Distribution

Table 2-3 shows the energy distribution of the 30 cm pool fires of methanol, heptane and toluene. The ideal heat release ( $Q_{chem}$ ) and the total feedback ( $Q_{fb}$ ) are based on the burning rate of the fuel. The energy loss term ( $Q_{loss}$ ) is estimated from the increased sensible energy of the fuel and the increased temperature of the cooling water. The sensible energy of the fuel was estimated from the liquid fuel temperature distribution.

FUEL	$Q_{\text{CHEM}}^a$ (kW)	$Q_{\text{RAD}}^b$ (kW)	$Q_{\text{FB}}^c$ (kW)	$Q_{\text{LOSS}}^d$ (kW)
METHANOL	20.6 ± 5%	5.8 ± 10%	1.1 ± 5%	0.01 ± 10%
HEPTANE	126 ± 5%	39.0 ± 10%	1.4 ± 5%	0.07 ± 10%
TOLUENE	131 ± 5%	39.4 <sup>e</sup> ± 10%	1.6 ± 5%	0.13 ± 10%

<sup>a</sup> Based on complete combustion to stable gas products

<sup>b</sup> Multi-location measurements

<sup>c</sup> Based on average fuel burning rate

<sup>d</sup> Based on increased sensible energy of liquid fuel and energy lost to cooling water

<sup>e</sup> Based on estimate of radiative loss fraction

Table 2-3 Energy distribution in 30 cm pool fires

### **2.3.6 Spectral Fuel Vapor Transmittance and Flame Emission**

The spectral content of flame emission at  $x/D = 1.0$  for heptane and toluene are presented in Fig. 2-16. The greater amount of soot in toluene accounts for the generally larger emission signal as compared to heptane. The spike at 4500 nm is due to  $\text{CO}_2$  and is quite evident in both flames. In heptane, the emission at 4500 nm is quite large when compared to soot emission which is evident across the spectrum. This indicates that gas band radiation in heptane should be quite significant. In contrast, the  $\text{CO}_2$  emission at 4500 nm for toluene, though apparent, is not overwhelming compared to the soot emission across the spectrum.

Fig. 2-17 presents the fuel vapor transmittance for heptane and toluene. Significant drops in transmittance are seen at wavelengths of approximately 3400 nm for both heptane and toluene and 4500 nm for heptane. The drop in transmittance at 4500 nm for toluene may have been missed due to the large (200 nm) measurement interval as opposed to the heptane measurements. The 4500 nm line corresponds to the presence of  $\text{CO}_2$  in the flame. The drop in fuel vapor transmittance does not correspond with regions of high flame emission (Fig. 2-16) indicating that fuel vapor above the fuel surface is not an important absorber of incident radiation.

### **2.3.7 Fuel Surface Reflection**

A possible component of the radiative feedback process in pool fires could be the reflection of the incident radiation off the fuel surface. Fig. 2-18 shows measurements of thermal radiation off the surface of water, toluene, methanol, and heptane at various incident angles. At very low incident angles, a large percentage of the incident energy is reflected off the fuel surface and is not involved in the vaporization of the fuel.

## **2.4 Summary and Conclusions**

1. The total radiative heat output for a variety of liquid fuels was obtained using a multi-point measurement technique. Several alcohol fuels were considered at different scales and a radiative heat loss fraction of approximately 0.2 was found. A variety of paraffin and aromatic fuels, with vastly different sooting tendencies, were also tested at different scales and a radiative heat loss fraction of approximately 0.3 was found over the range investigated.

2. The radiative heat flux distributions for paraffin and aromatic fuels correlated fairly well as a function of heat release rates and flame length in the axial and radial directions. Radiative heat flux for methanol correlated well in the axial direction, but showed a large amount of scatter in the radial direction possibly due to the small levels of signal.

3. The effective radiation temperatures and transmittances for heavily sooting toluene and moderately



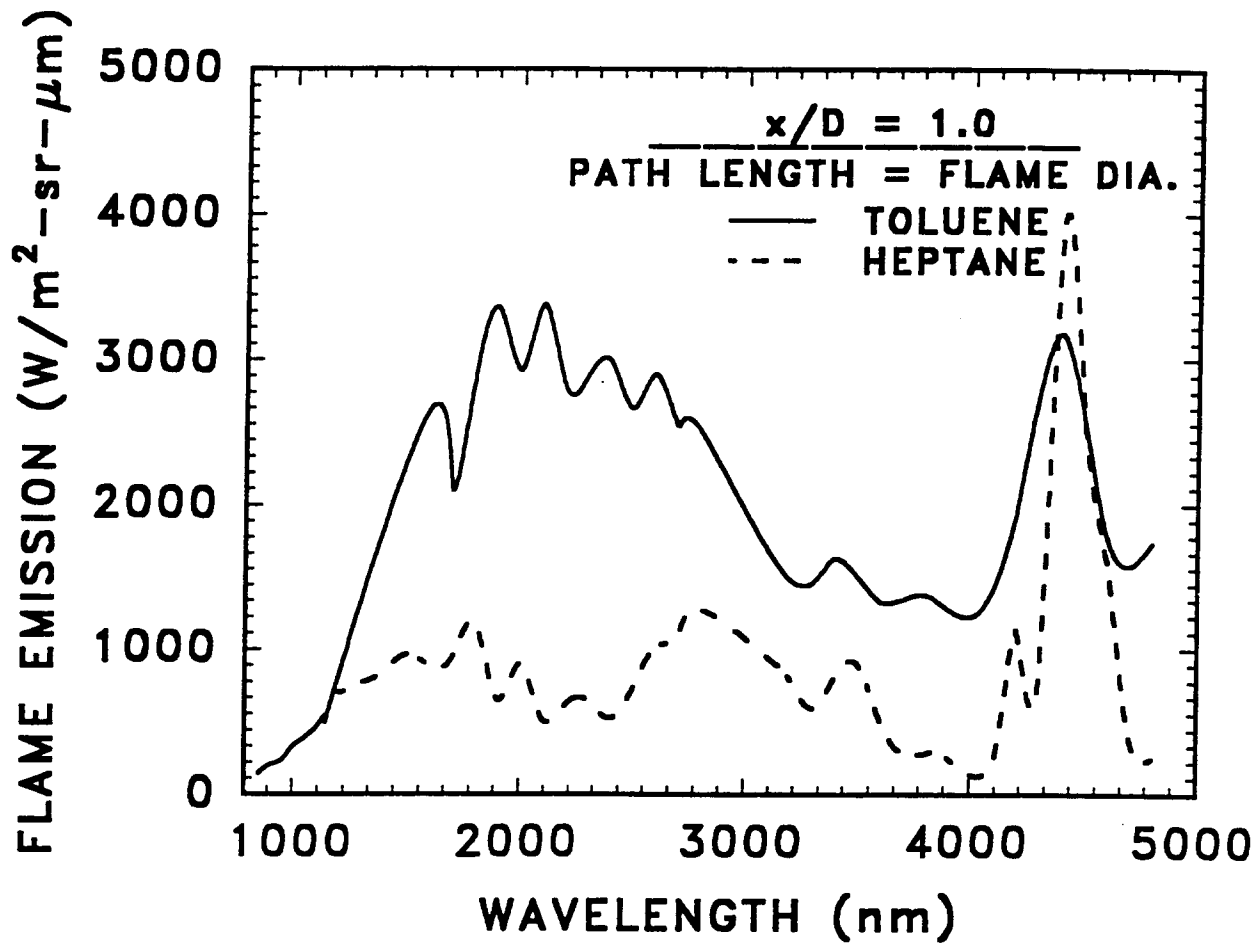


Fig. 2-16 Flame emission at various wavelengths for toluene and heptane flames

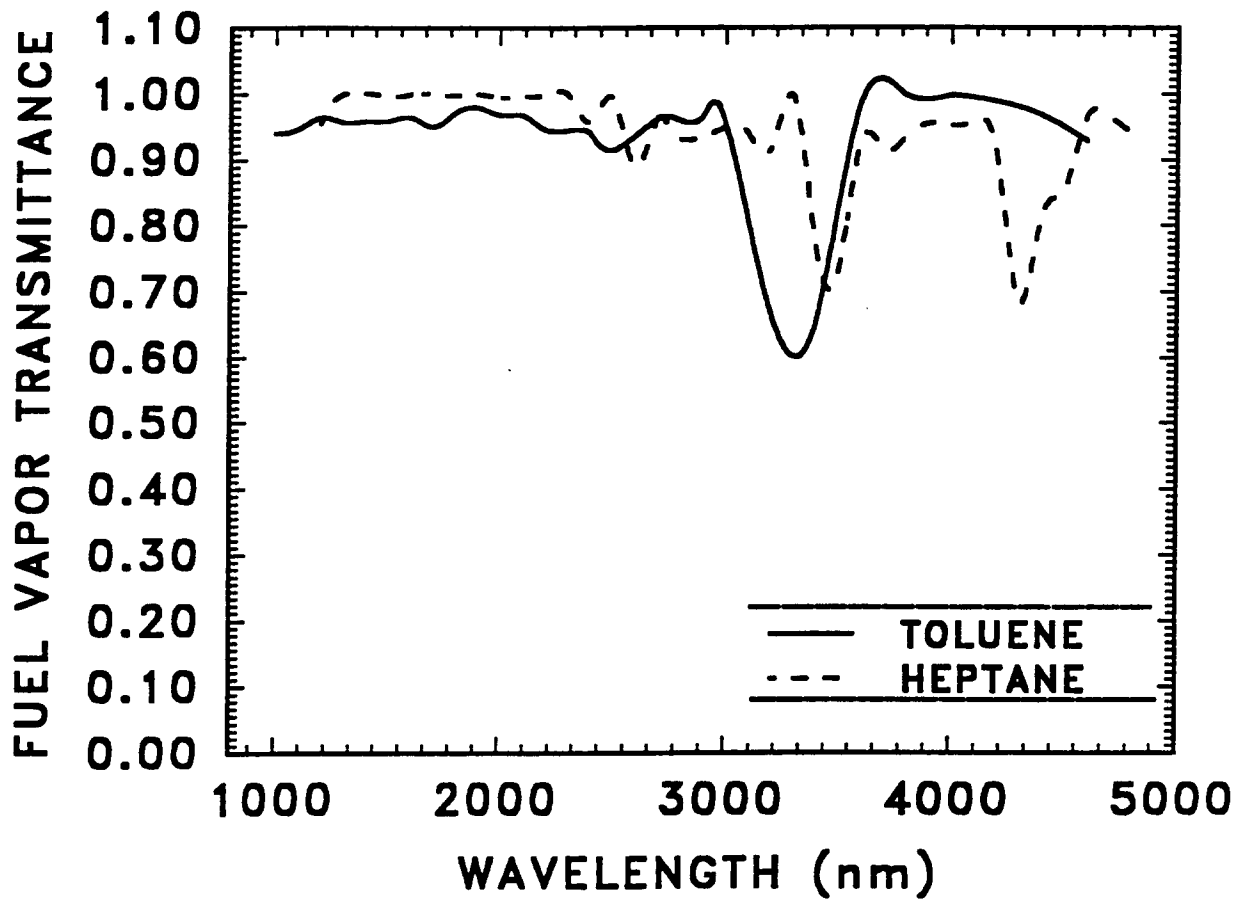


Fig. 2-17 Fuel vapor transmittance at various wavelengths for toluene and heptane

sooting heptane indicate that toluene contains a large volume of "cold" soot particles which are not contributing to emission. This may explain the similarity of  $X_R$  and heat feedback for fuels of differing sooting tendency.

4. The visible flame heights measured during the present investigation satisfied the correlations of Zukoski et al. (1984) for buoyant diffusion flames. Flame heights for methanol correlated very well at all scales. At the larger scales, flame heights for heptane and toluene did not correlate well as a function of idealized heat release, possibly due to low combustion efficiency. Accurate measurement of toluene flame heights was difficult at larger scales due to blockage by cold soot particles.

5. Measurements of flame emission and fuel vapor transmittance in toluene and heptane indicate that fuel vapor absorption of radiation is not significant in these flames. Flame emission measurements show that gas band radiation in heptane flames should prove to be important, while in toluene flames, continuum soot radiation is dominant. Reflection of incident infrared radiation ( $\lambda = 1.0 - 3.0 \mu\text{m}$ ) is substantial at low incident angles.

## CHAPTER III RADIATIVE FEEDBACK TO THE FUEL SURFACE

### 3.1 Introduction

A major goal of this investigation is to improve the understanding of the role of radiation in providing energy for fuel vaporization in liquid pool flames. Measurements of radiation heat flux incident on the fuel surface in different directions at various radial positions are necessary for this purpose. In the following, existing measurements of hemispherical radiative heat feedback and the techniques used for these are reviewed. Measurements of directional heat feedback to the fuel surface have not been reported in the past. Therefore, a new technique was developed for obtaining these. The technique and its application to the pool fires is described in this chapter and the resulting measurements are reported and discussed. Fuels of various sooting tendencies were used and differences in radiative feedback characteristics are examined.

Blinov and Khudiakov (1957) monitored burning rates for a variety of industrial fuels in pools consisting of concentric rings. Total heat transfer to the fuel within each ring can be found based on the local fuel burning rates within each ring. Blinov and Khudiakov (1957) found the highest heat transfer at the pool center, decreasing somewhat along the radius, and increasing at the pool edge. Akita and Yumoto (1965) used a multi-ring pool to obtain local measurements of burning rates in methanol. This study found qualitatively different results than Blinov and Khudiakov (1961) for their methanol pools. Hamins (1992) found results similar to Blinov and Khudiakov (1957) for several fuels, including methanol. Modak and Croce (1977) measured the local fuel surface regression rates for various sizes of square PMMA fuel beds (.025 - 1.22 m (side)). Radiative feedback was found from a surface energy balance. Convective heat feedback was assumed to be the primary heat transfer mechanism for the smaller diameter pools and taken as a constant. Heat feedback was shown to be dominated by thermal radiation at larger scales.

A few investigators have reported direct measurements of heat feedback at the fuel surface in order to determine the importance of radiation and convection components. Corlett and Fu (1965) measured the fuel vaporization rate in an insulated teflon cup containing fuel placed in 30 cm pools. Their calorimetric measurements indicated that radiation was an important component in non-sooting methanol fires. Alger et al. (1979) used Gardon and transpiration radiation gauges to measure total and radiative heat feedback in large (3 m) methanol pool fires. Shinotake et al. (1985) used gardon gauges with differing surface emissivities to separate convective and radiative components. Measurements at four locations in heptane pool fires of 100, 70, and 30 cm were

made. Results indicated that radiation contributed 80% of the total feedback for the 100 cm and 80 cm pools and 70% of the total feedback for the 30cm pool. Yumoto (1971) also used two color Gardon gauges in intermediate sized hexane pools. This study showed slightly larger contributions of radiation to the total heat feedback. Changes in surface emissivity of the gauges by fuel condensation and soot deposition are some the problems associated with this technique.

### **3.2 Experimental Methods**

#### **3.2.1 Experimental Apparatus**

The details of the pool burner and fuel supply system are described in Section 2.2. Radiative feedback measurements were performed in the 30, 60 and 100 cm diameter burners. A constant fuel level (5 mm below burner rim) was maintained. The apparatus was allowed an adequate warm-up period before data were acquired. The warm time was determined by a trial and error procedure to obtain steady burning rates and flame heights. The feedback radiometer was mounted on a traverse system that allowed for linear motion in two directions and angular motion about the radiometer axis. The traverse system enabled measurements to be taken at locations over most of the fuel surface. Measurements of radiative feedback in the 60 cm burner for heptane and toluene were made in the center of the burner due to traversing difficulties caused by the large heat release of these flames. Feedback measurements in the 100 cm burner were made for methanol only.

#### **3.2.2 Instrumentation**

The radiometer was specifically designed for use in the hostile environment near the fuel surface. The radiative component of heat feedback was measured independently avoiding the need for approximate models for deducing this quantity. Convective heat transfer was eliminated by placing the heat sensing element inside a gauge housing which is water cooled and has a purge flow of nitrogen over the sensing element and through its aperture.

Fig. 3-1 shows a schematic of the gauge. The sensing element is recessed 11 mm below the top surface of the gauge. This restricts the gauge field of view to 14° (half peak). This design allows measurements of directional heat fluxes resolved to a relatively narrow angle. The methodology for determining total hemispherical radiative heat flux from directional measurements is fully described in section 3.3.3. The spectral response of the gauge was flat between 0.5 and 10  $\mu\text{m}$ . A nitrogen purge (30 cc/min) was used to prevent soot and fuel vapor deposition on the sensing element. Care was taken to determine that this purge had minimal effect on the flame. Additionally, considerable cooling the gauge using tap or warm water was required to maintain the gauge at a relatively constant temperature. Increased gauge temperature changed the baseline zero. Fig. 3-2 shows the arrangement used for

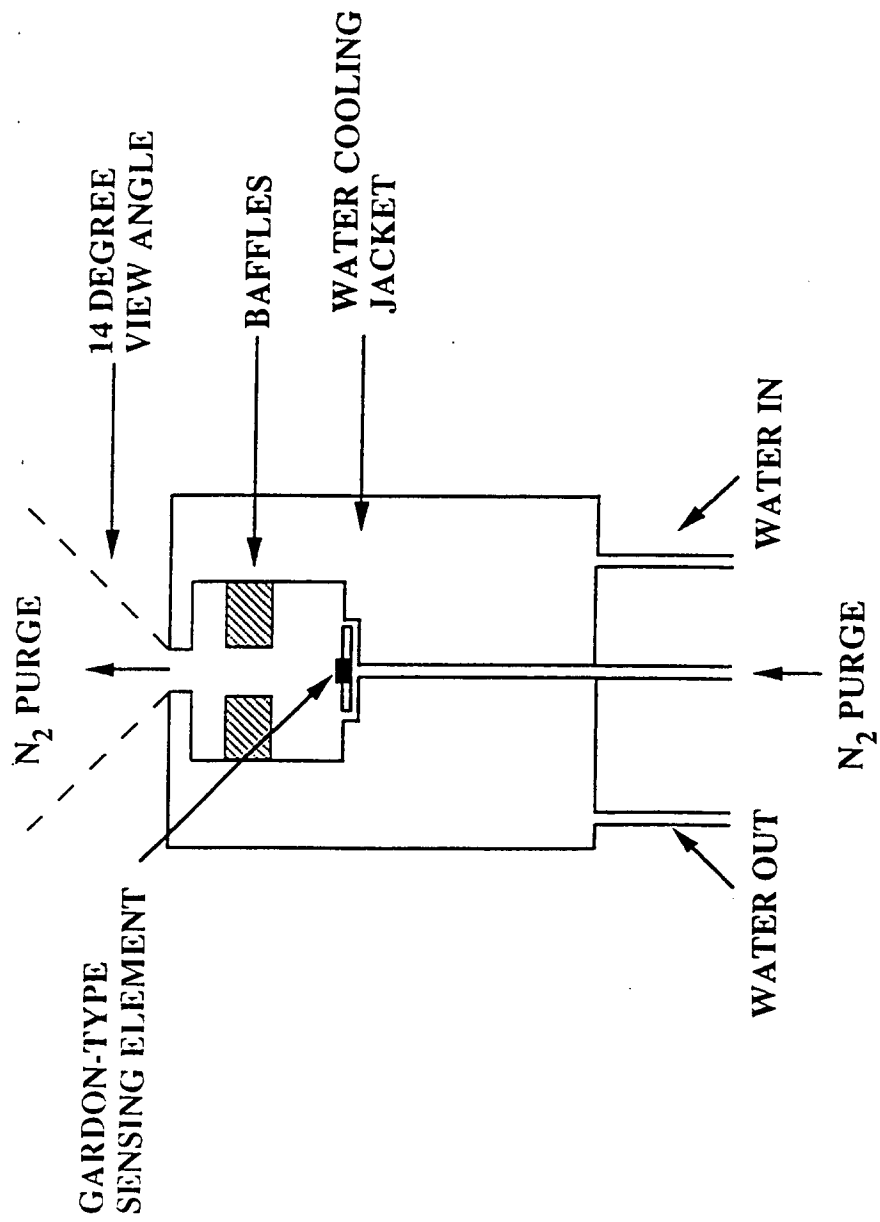


Fig. 3-1 Sketch of Feedback Radiometer

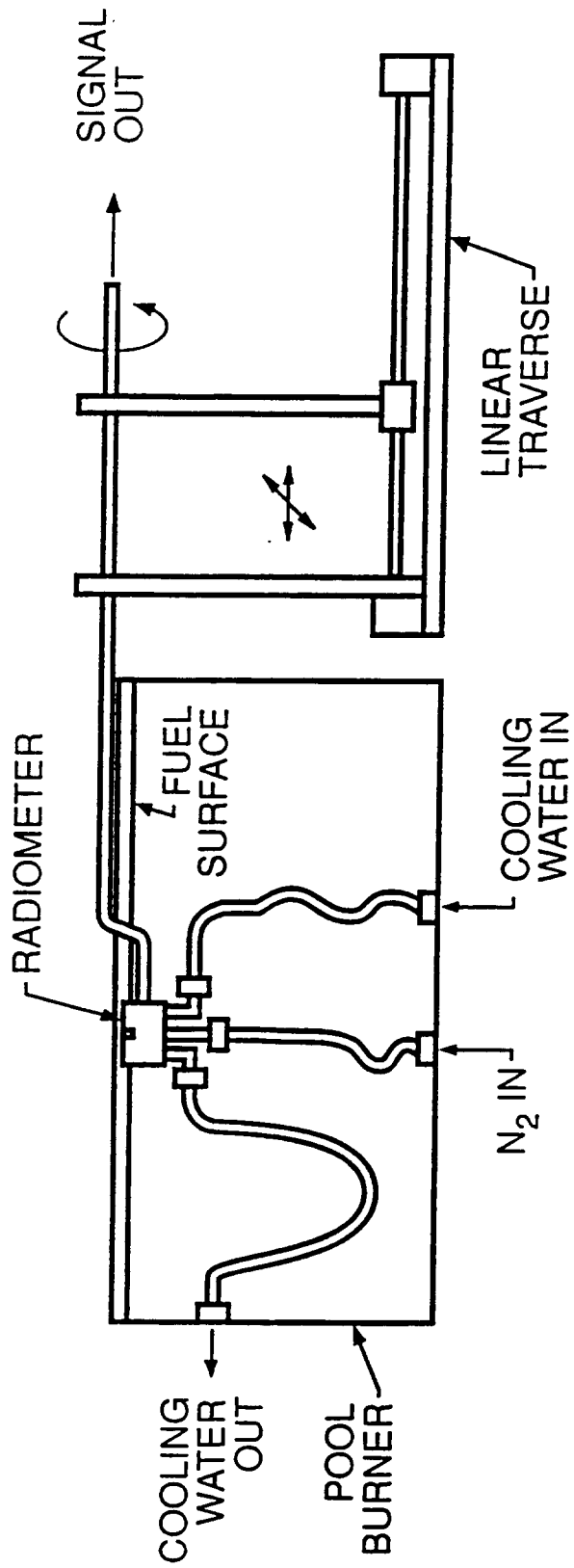


Fig. 3-2 Sketch of feedback radiometer traversing system

traversing the gauge, changing its view direction and delivering the purge and cooling water flows. Cooling water and the nitrogen purge were delivered to the gauge through tubing which ran through the fuel residing in the burner. This design allows for minimum intrusion of the gauge on the flame.

The signal from the radiometer was sent to a digital amplifier (gain = 500) and then sampled by a data acquisition computer. The sampling rate was 30 Hz. The signal was sampled for 90 seconds at each location. Effects on the signal by gauge heating were found by measurement of the baseline signal. This was accomplished by placing a water cooled cap over the radiometer (with nitrogen purge maintained) with the flame burning but the flame radiation blocked from the gauge. An uncertainty of 10% for the intensity measurements is estimated from repeated trials.

#### Radiometer Calibration

Calibration consisted of comparison of the voltage generated by the radiative feedback radiometer with that generated by a standard wide angle radiometer (150° field of view) in response to a known blackbody flux. Measurements of incident intensity from the black body were made as the feedback radiometer was rotated about the center of the top surface. These values were integrated using the technique described in section 3.3 and compared with the standard radiometer to obtain the calibration factor. Nitrogen purge and the appropriate water cooling were used during calibration.

#### 3.2.3 Data Analysis

Due to the narrow field of view, the feedback radiometer measured incident directional intensity at a given location on the fuel surface. The hemispherical radiant heat flux to a point is found by integrating all directional intensities intersecting a hemispherical surface placed over that point. Fig. 3-3 (following Siegal and Howell (1981)) indicates the geometry used in this integration. Intensity measurements are made at several positions about the surface of the hemisphere. These values are then integrated over the hemisphere using the trapezoidal rule utilizing (Siegal and Howell, 1981):

$$Q_{rad} = \iint [I(\theta, \phi)] \sin(\theta) \cos(\theta) d\theta d\phi \quad (3-1)$$

The quantity  $\sin \theta d\theta d\phi$  in Eqn. (3-1) describes the surface area on the unit hemisphere that the intensity in direction  $(\theta, \phi)$  intersects (Fig. 3-3).

Axial symmetry allowed the integration to be separated into two parts. The limits of integration over two quadrants of the hemisphere are defined by:

$$\begin{aligned} 0 \leq \theta \leq \pi/2 \quad \text{and} \quad \pi/2 \leq \phi \leq 3\pi/2 \\ 0 \leq \theta \leq \pi/2 \quad \text{and} \quad -\pi/2 \leq \phi \leq \pi/2 \end{aligned} \quad (3-2)$$

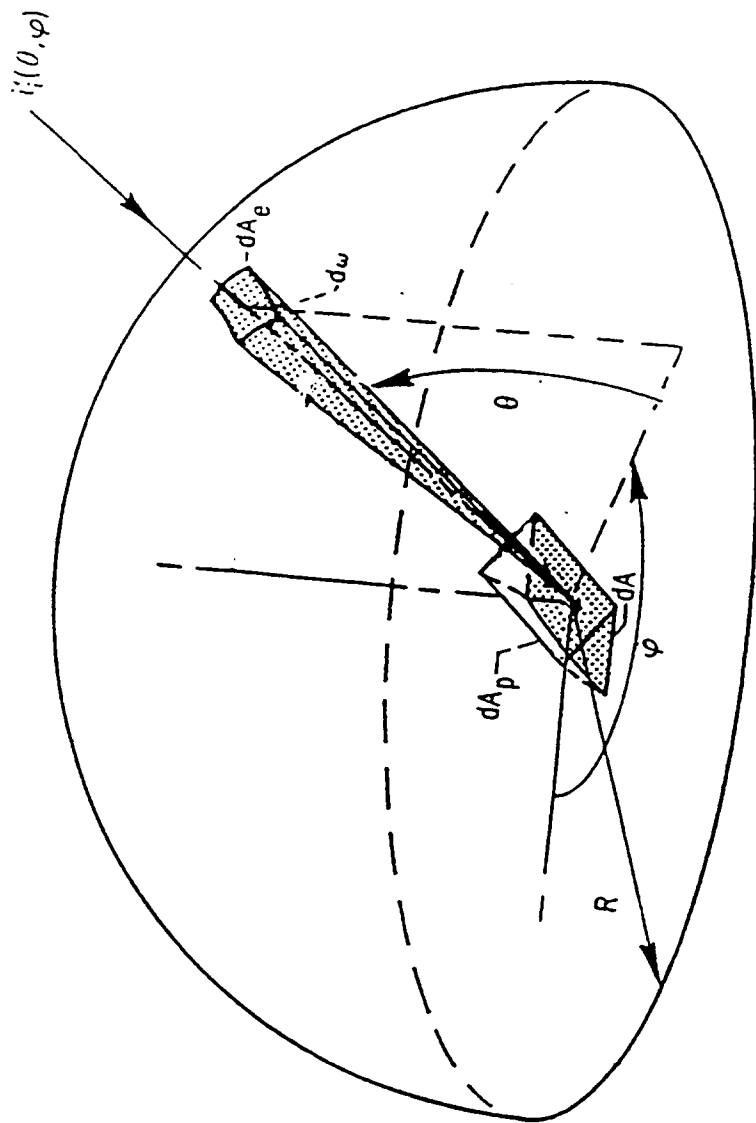


Fig. 3-3 Hemispherical coordinate system

where  $\theta = 0$ ,  $\phi = 0$  defines a ray parallel to the fuel surface towards the pool center and  $\theta = 90$ ,  $\phi = 0$  defines a ray normal to the fuel surface.

#### 3.3.4 Operating Conditions

Radiative feedback measurements were made for three fuels: toluene, heptane, and methanol. The test conditions are summarized in Table 3.1. Intensity measurements were made at a minimum of 8 radial positions across the pool surface. At most radial locations, angular distributions of a minimum of 11 pairs of angles ( $\theta, \phi$ ) were found (before assuming axial symmetry). Where direct measurements were not possible, linear interpolation was used to fit an intensity value for that position.

Tap water was used for cooling the feedback gauge during the heptane and methanol tests. In toluene, vapor condensation on the gauge surface occurred when cooling with tap water was utilized. Therefore, warm water (approximately 60°C) pumped from a water bath was used for cooling the gauge during these tests. As the water lines were routed through the liquid fuel, the temperature of the cooling water affected the fuel burning rate. This effect is noted in Table 3-1. Signal baseline changes were measured during each data collection session. The baseline did change with gauge angle but proved to be fairly insensitive to radial position along the fuel surface.

### 3.3 Results and Discussion

#### 3.3.1 Radiative Feedback in the 30 cm Burner

Figure 3-4 shows directional radiative intensity as a function of distance for the methanol pool fire for representative directions. The angular variation is shown for angles looking away from pool center ( $\phi = 0$ ). Figure 3-5 shows a similar figure for the heptane pool fires with the same representative directions as shown in Fig. 3-4. The burner center is located at  $r = 0$  cm. It was found for all fuels and radial positions, the peak intensity occurred at  $\theta = \pi/2$  when the radiometer was looking away from the pool center ( $\phi = 0$ ). When  $\phi = \pi$ , the intensities initially increased with distance from the pool center. This is due the increased radiation path length through the flame. Figure 3-6 shows the intensity distribution for the heptane flame at  $r = 0$  cm (pool center) for various angles of  $\theta$  at  $\phi = 0$  and  $\pi$ . Figure 3-7 shows a similar plot for heptane at  $r = 8$  cm. Significant intensities were measured from all directions.

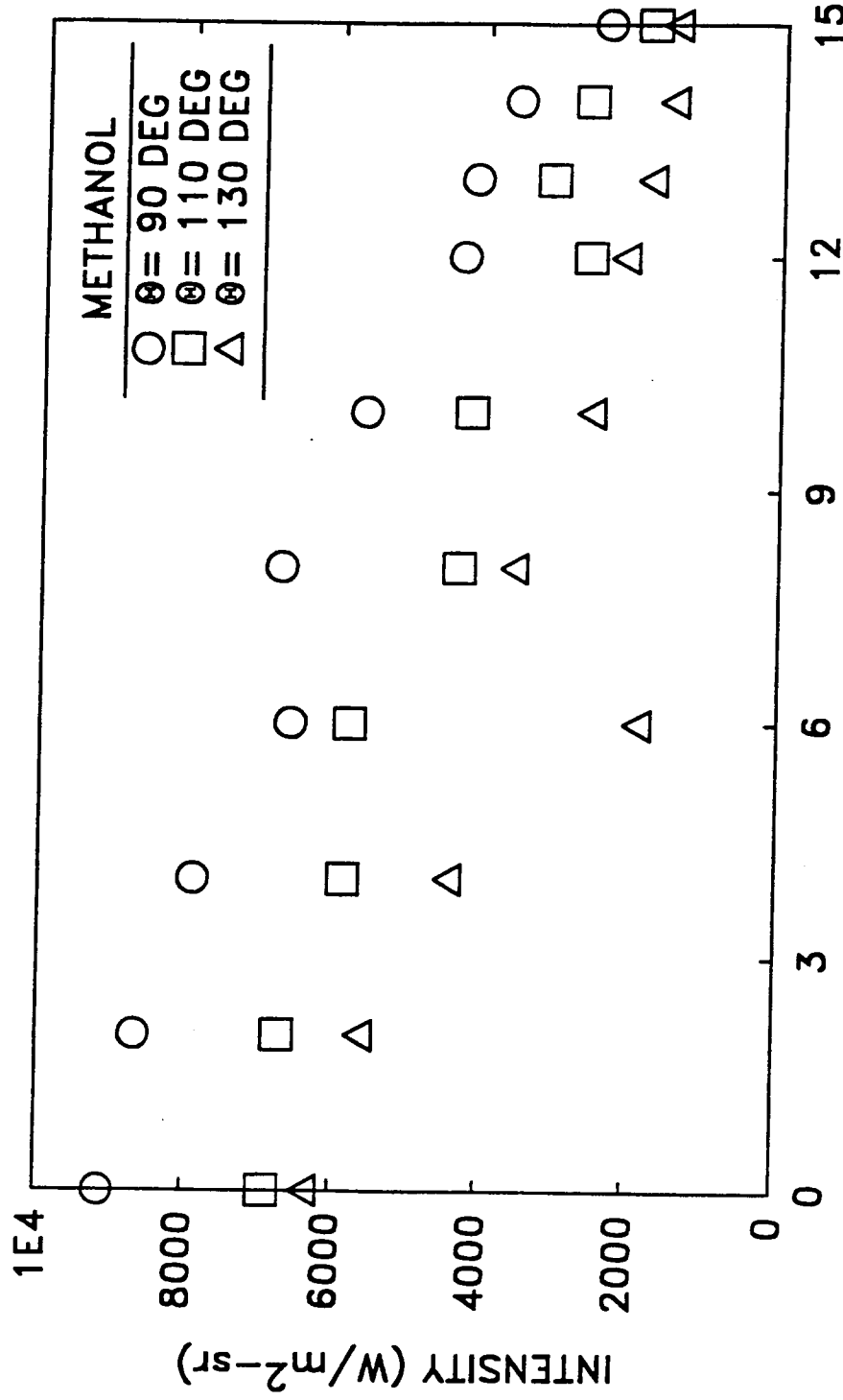
The intensities from the heptane flame are twice as large as those from the methanol flame for a given angle and radial position. This is due to contribution of continuum radiation from soot in the heptane flame, which is not present in the methanol flame. Toluene showed similar magnitudes of intensity as the heptane flames for directions normal to the fuel surface but received greater contributions from angles off the normal to the fuel surface.

FUEL	FUEL BURNING RATE (g/s)	HEAT RELEASE <sup>a</sup> (kW)
<b>30 cm Burner</b>		
METHANOL	0.81	18
HEPTANE	2.34	113
TOLUENE	4.05	166
<b>60 cm Burner</b>		
METHANOL	3.676	81
HEPTANE	16.76	747
TOLUENE	15.54	638
<b>100 cm Burner</b>		
METHANOL	10.78	238

<sup>a</sup>estimated based on complete combustion to stable gaseous products

Table 3-1. Operating Conditions for Radiative Feedback Measurements

# INTENSITY vs RADIAL POSITION VARIOUS ANGLES



**POOL CENTER**      **RADIAL POSITION (cm)**      **POOL EDGE**  
 Fig. 3-4 Directional radiative heat feedback as a function of angle and radial position in methanol

# INTENSITY vs RADIAL POSITION VARIOUS ANGLES

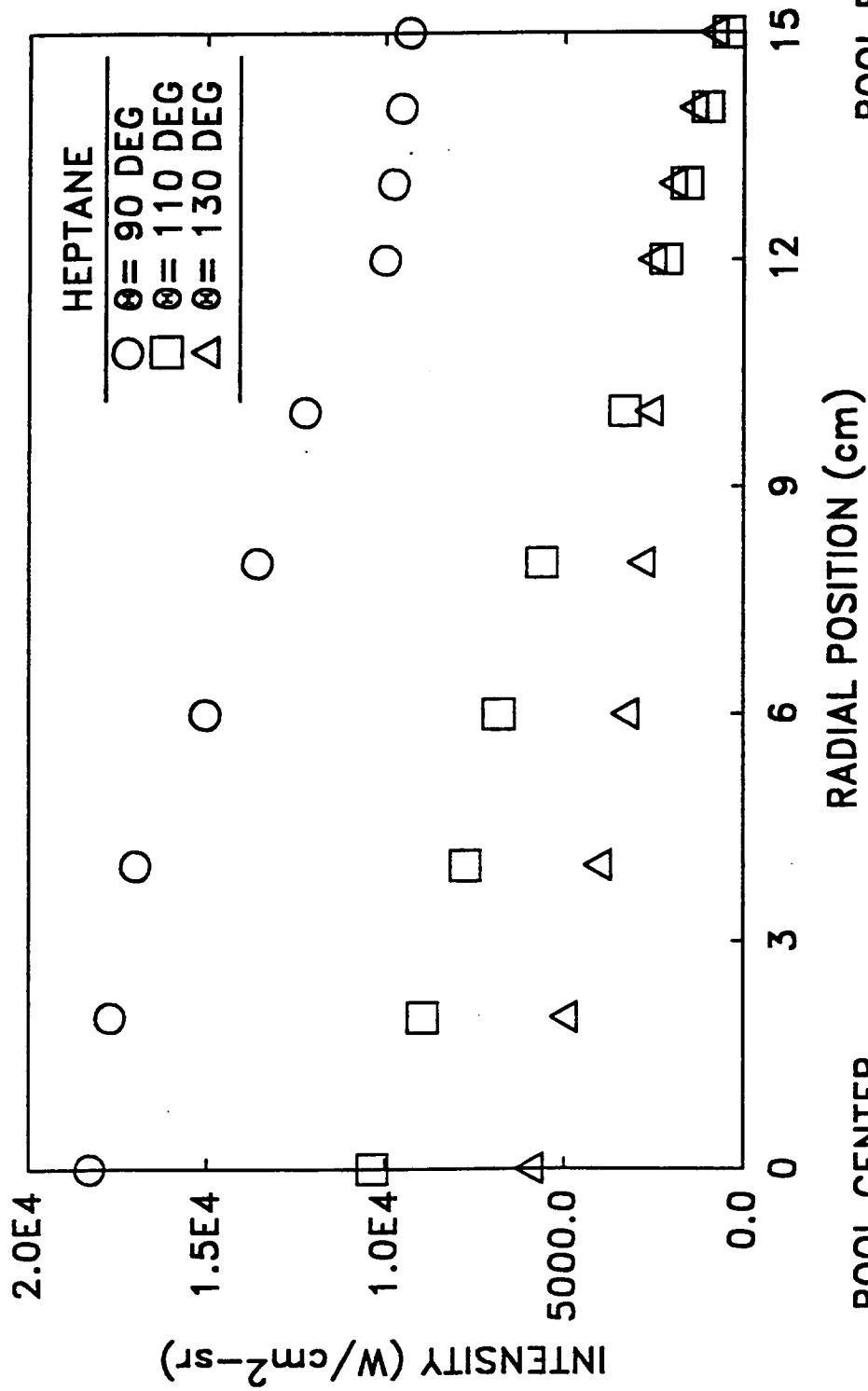


Fig. 3-5 Directional radiative heat feedback as a function of angle and radial position in heptane

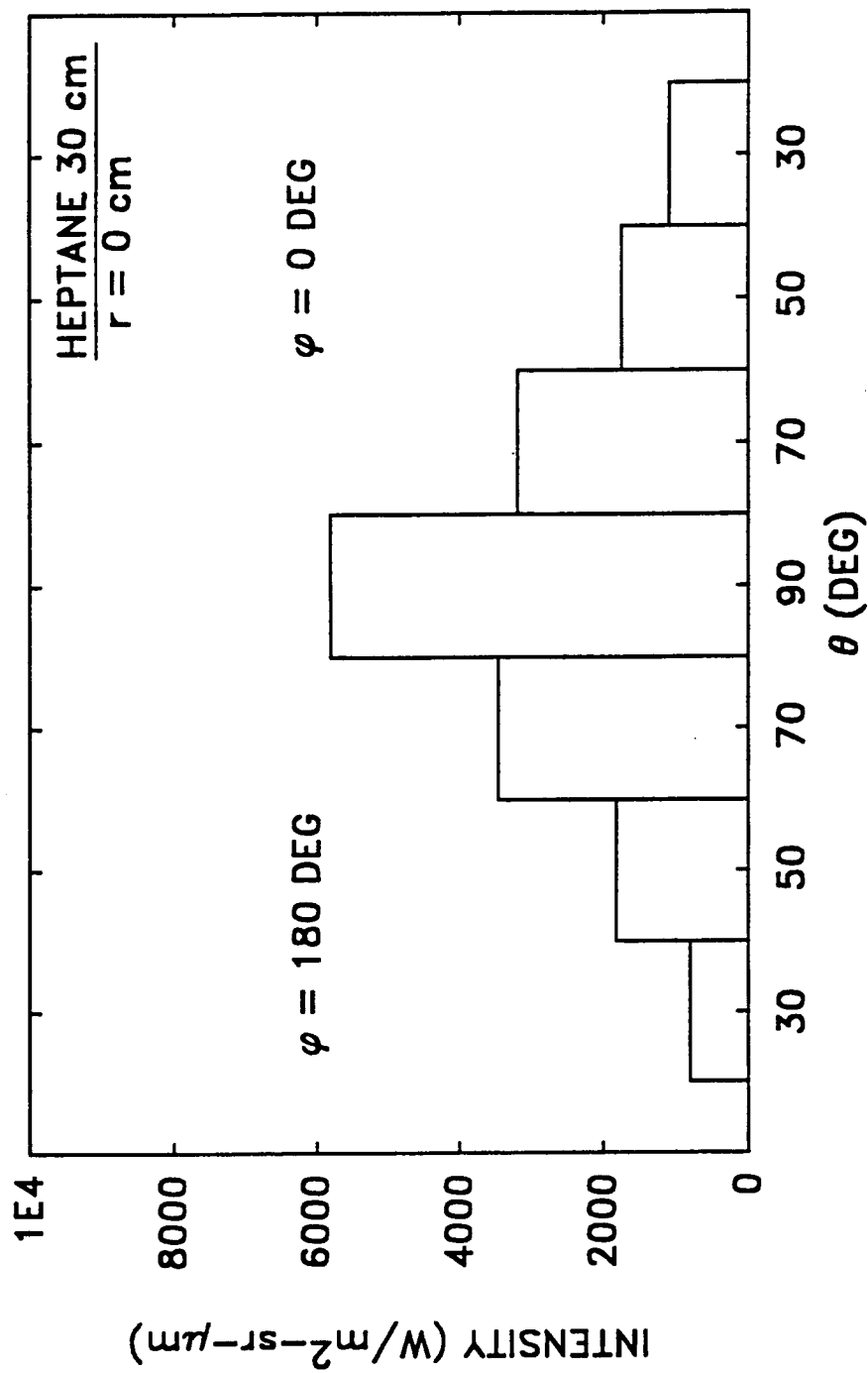


Fig. 3-6 Distribution of directional radiative heat feedback at  $r=0$  cm for heptane

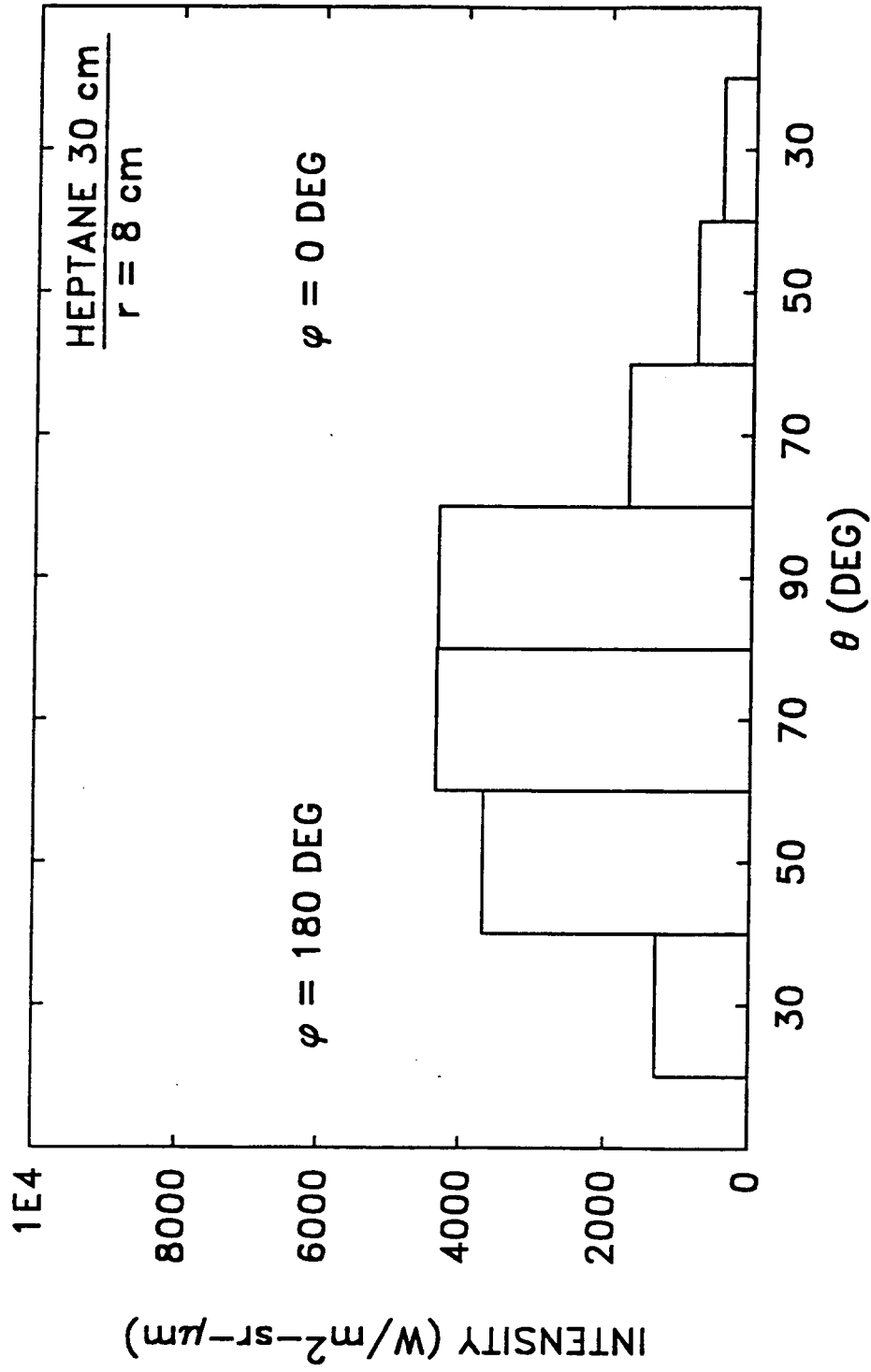


Fig. 3-7 Distribution of directional radiative heat feedback at  $r = 8 \text{ cm}$  for heptane

The incident intensity values are integrated over the hemispherical surface using the technique described in section 3.3. Figure 3-8 shows the incident radiative heat flux for toluene, heptane and methanol as a function of radial position. The radiative heat flux profiles for toluene and heptane are fairly flat profiles across the fuel surface. In heptane, the radiant heat flux drops slightly only at the edge of the pool. However, methanol flames have a large reduction in the radiant heat flux from the pool center ( $r = 0$  cm) to the pool edge. This result is evident in the flame shapes of the various flames. Toluene and heptane flames are quite broad at the base and neck towards the pool center approximately 5 cm above the burner. This shape provides a consistent radiation source across the majority of the fuel surface. The methanol flame swept across the fuel surface just above the burner lip, leaving a thin flame over the fuel at large radii. The flame begins to neck upwards only near the center of the burner.

Hamins (1992) measured burning rates in 30 cm concentric ring pool flames for methanol, heptane and toluene. The steady-state heat flux incident at the fuel surface in each ring was:

$$q_i'' - m_i'' (H_{fg} + C_p (T_s - T_a)) + q_w'' \quad (3-3)$$

where  $i$  is the ring number,  $q_i''$  is the average energy flux ( $\text{kW/m}^2$ ) incident on the  $i^{\text{th}}$  annular ring,  $m_i''$  is the average mass burning flux ( $\text{g/m}^2\text{-s}$ ) in the  $i^{\text{th}}$  annular ring,  $H_{fg}$  is the heat of vaporization,  $T_s$  is the pool surface temperature assumed to be equal to the boiling temperature,  $T_a$  is the ambient temperature, and  $q_w''$  is the sum of the energy lost to the surroundings and the increased sensible energy of the fuel resident in burner. The sensible energy increase was calculated from the temperature gradients measured in the liquid fuel. The energy lost to the surroundings was found by measuring the temperature change in the cooling water reservoir. The loss term  $q_w''$  was measured to be 1%, 5% and 8% of the incident energy ( $Q$ ) for the methanol, heptane, and toluene fires respectively.

Figure 3-9 compares the results from the radial variation of radiation feedback measurements normalized with the burning rate measurements of Hamins (1992). The radiative feedback results have been corrected for fuel burning rate differences caused by the presence of the radiometer. The experimental uncertainty of the normalization presented in Fig. 3-9 is estimated to be 20%, mainly due to the effects of different burning rates in the tests. Figure 3-9 shows that the heat feedback is dominated by radiation across the entire burner for toluene and heptane fires. Methanol also has a significant radiation component, even without the presence of soot. At the pool center, heat feedback in methanol fires is also dominated by radiation. Convection played a significant

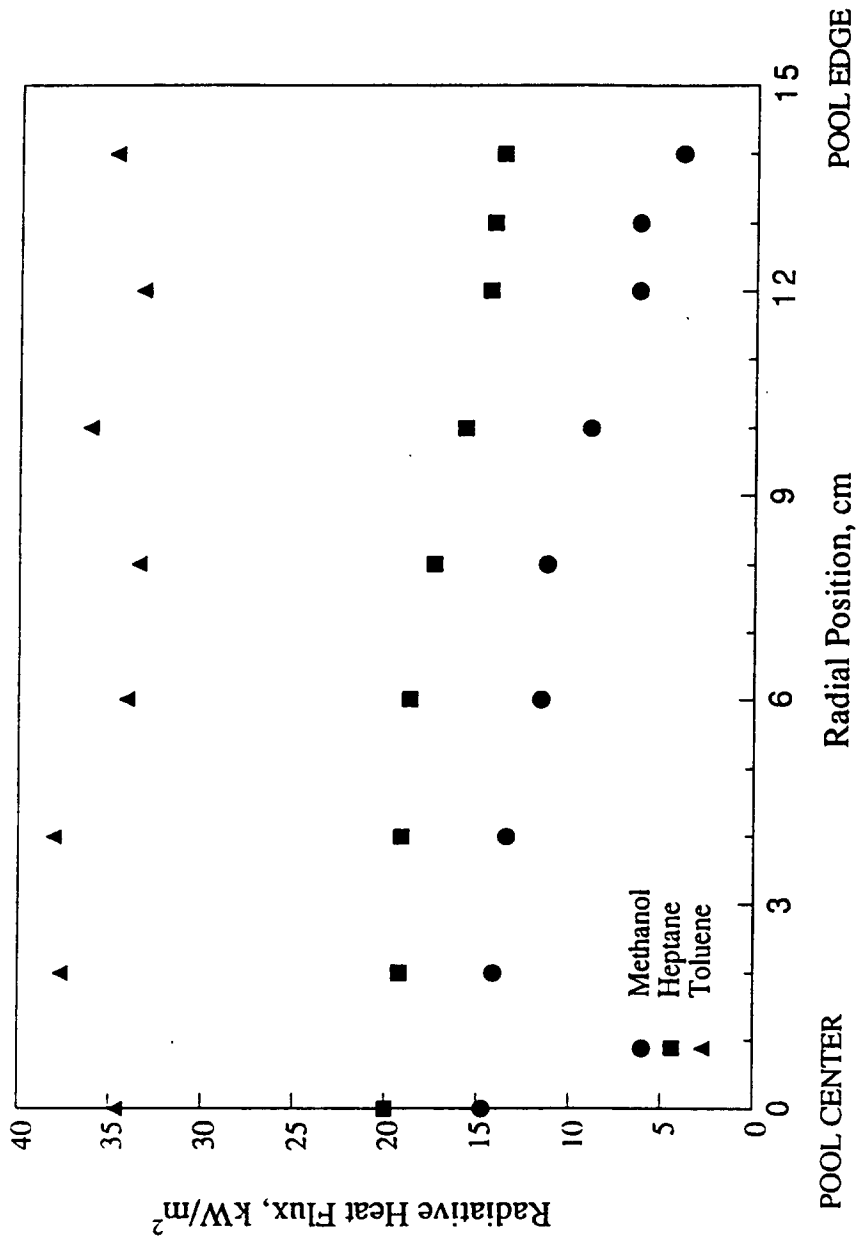


Fig. 3-8 Radiative heat feedback as a function of radial position for methanol, heptane and toluene

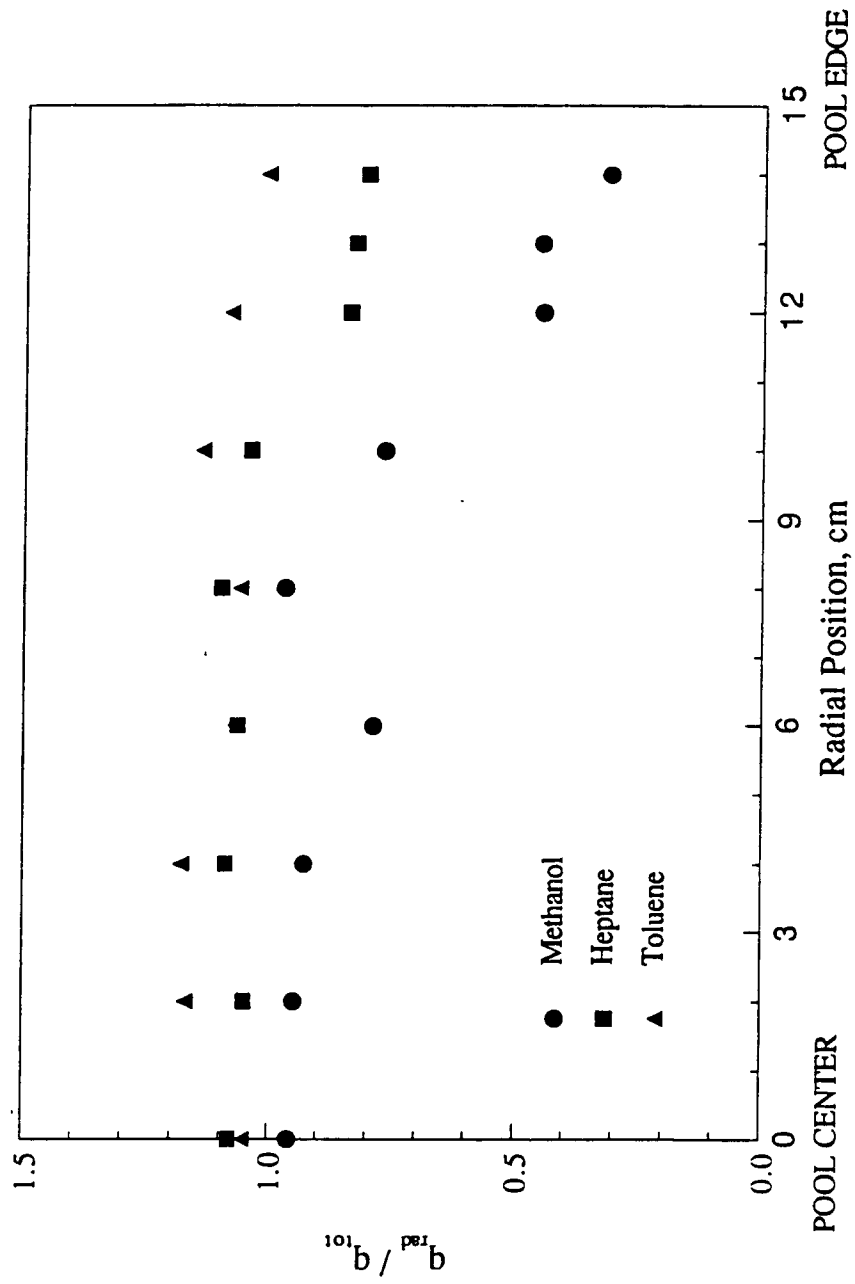


Fig. 3-9 Normalized radiative heat feedback as a function of radial position for methanol, heptane and toluene (uncertainty  $\pm 20\%$ )

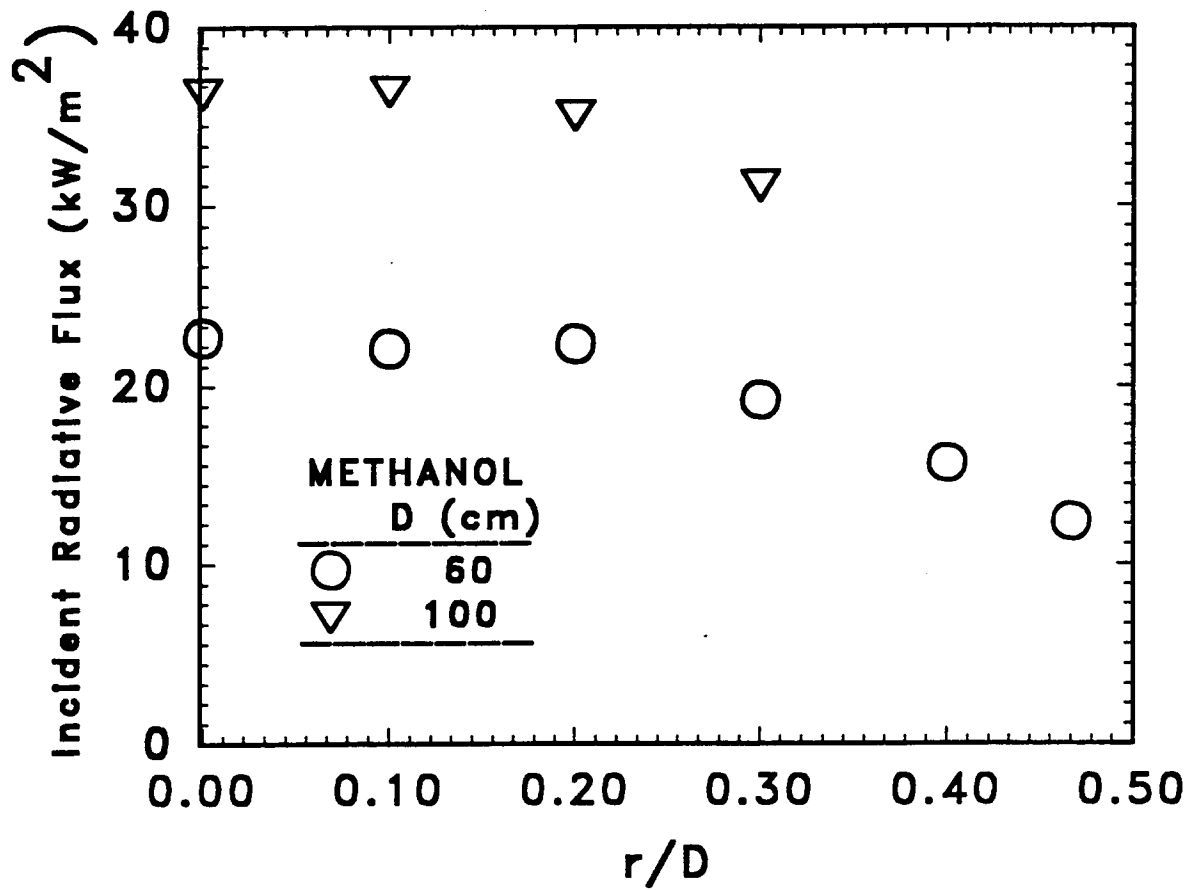


Fig. 3-10 Radiative heat feedback as a function of radial position for methanol in 60 and 100 cm burners

role near the pool edge, where radiation contributed 35% of the total heat feedback.

### 3.3.2 Radiative Feedback in 60 and 100 cm Burners

Measurements of incident radiative feedback to the fuel surface for methanol (60 and 100 cm) are presented in Fig. 3-10 as a function of radial position. As was found for methanol in the 30 cm burner, the incident radiation decreases as the distance from the pool center increases.

Measurements of incident radiation on the fuel surface at  $r/D = 0.0$  for toluene found  $47.6 \text{ kW/m}^2$ . This value is considerably higher than the average amount of energy necessary for vaporization of the fuel ( $28 \text{ kW/m}^2$  based on burning rate).

### 3.4 Conclusions

Radiative heat feedback was measured using a narrow-angle, nitrogen purged radiometer which was placed just above the fuel surface. Considerable care was taken to prevent fuel vapor condensation and soot deposition on the sensing element of the radiometer. The angular distribution of radiative feedback was found for positions across the radius of a 30 cm pool for fuels of differing flame luminosity and shape. The main conclusions from the radiative feedback measurements are as follows:

1. Considerable contributions to radiant feedback flux are found from all directions. Multi-ray calculations of radiative heat feedback must consider the intensity contributions from different directions.

2. Radiation was found to be a significant, heat transfer mechanism in medium and large scale pool flames of vastly different luminosity. The radiative feedback contributed almost the entire heat transfer to the fuel surface in toluene and heptane fires. Radiative heat feedback was also found to be large near the center of methanol pool fires, but the radiative contribution diminished considerably near the pool edge.

The measurements discussed in this chapter show the importance of radiative heat transfer for fuel vaporization in medium-sized pool flames. Measurements are available for the evaluation of predictions of radiative feedback using local flame emission and absorption characteristics. Such an evaluation is undertaken in Chapter 5.

## CHAPTER IV LOCAL EMISSION/ABSORPTION PROPERTIES

### 4.1 Introduction

Emission and absorption properties of liquid pool flames are of interest in fire safety applications due to their strong influence on the radiant heat loading and radiant heat feedback. Knowledge of heat feedback from flames to fuel surface is also relevant in other applications such as spray flames and solid rocket motors. The objective of the present work was to obtain and interpret simultaneous local measurements of spectral emission and absorption of radiation in liquid fueled pool flames. Toluene was selected as the fuel based on its frequent use as an industrial solvent and because of its strong sooting tendency which is common to most practical hazardous fires.

Experimental studies of pool flames date back to the work of Blinov and Khudiakov (1957) and Hottel (1958). These authors recognized the turbulent nature of pool fires at relatively small pool sizes. The importance of radiative heat transfer in determining the burning rates at relatively large scales was recognized (Hottel, (1958) and Burgess and Hertzberg, (1974)). The early models utilized an average flame emissivity, a shape factor and a constant flame temperature in the calculation of radiation heat flux (see Burgess and Hertzberg, (1974) for example). All of these parameters were obtained from experimental data regarding burning rates in conjunction with a homogeneous, gray flame assumption. Modak (1977) developed a method to obtain the individual shape factors for various radiation paths through the flames and treated the absorption coefficient and the effective radiation temperatures as properties of a complete radiation path. The effective temperature was obtained from Schmidt measurements and the local gray absorption coefficients were obtained from blackbody absorption data. Modak (1981) upgraded this method to include local measurements of mean temperatures and mean absorption coefficients obtained from path integrated blackbody emission and absorption data and subsequent deconvolution. Modak's models (1977, 1981) and other more recent global models (Shorki and Beyler, (1989) and Hamins et al. (1992)) rely on the assumption that the effects of fluctuations in temperature and absorption coefficients on the radiation heat flux (termed turbulence-radiation interactions-see Faeth et al. (1989) for example) can be treated using effective mean radiation properties. Orloff (1981) used Markstein's (1981) scanning radiometer measurements for obtaining effective temperature and absorption coefficients as a function of distance from the fuel surface. Variations in radiation intensity from different radial positions were assumed to originate from different view angles and flame shapes. The mean flame shapes were obtained by averaging instantaneous photographs similar to the work of Modak (1977, 1981).

Markstein (1981) obtained instantaneous measurements of emission intensity and absorption coefficients for arbitrary paths in pool fires. These data were processed to obtain moments of intermittency and spatial correlations of radiation intensity fluctuations. Markstein (1981) suggested that such information regarding turbulent properties was necessary for improved models of radiation from pool flames. Effects of turbulent fluctuations on radiative heat losses from gaseous jet and pool diffusion flames have been well-documented (see Kounalakis et al. (1988a,b), Sivathanu et al. (1990), Gore et al. (1991) and their references).

Fischer et al. (1987) measured the fluctuating temperature and mean absorption coefficient in a 0.5 m ethanol pool fire. Radiation predictions utilizing the measured mean properties were consistently lower than the experimental data. Enhanced predictions of intensity were obtained by incorporation of measured temperature fluctuations with the nonadiabatic fast chemistry approach. This further highlighted the need for including the effects of scalar fluctuations in radiation models.

The present study is focussed on determining the scalar property distributions including turbulent fluctuations in toluene-fired pool flames. The effects on heat feedback are of particular interest since the radiative flux in this case may originate in the visibly persistent flame zone near the liquid surface. Recently, Bouhafid et al. (1989) have detected intermittency in the visibly persistent zone. However, these authors suggest that the characteristics of the fluctuations near the liquid surface are those of an oscillatory laminar flame rather than a fully turbulent flame. It is therefore of interest to measure mean and turbulent scalar property distributions over an entire liquid-fired pool flame and then to evaluate the effects of fluctuations on heat flux incident at various locations including the fuel surface.

## **4.2 Experimental Methods**

### **4.2.1 Experimental Apparatus**

The details of the pool burners and fuel supply system are included in section 2.2. The emission/absorption measurements were made in the 7.1 cm burner. A constant level of fuel 3.5 mm below the burner rim was maintained in the pool burner.

### **4.2.2 Instrumentation**

Emission and absorption measurements resolved to 6 mm were obtained throughout the flame using the three-line technique described by Gore and coworkers (Sivathanu and Gore, (1992), Sivathanu et al. (1991) and Sivathanu and Gore (1991)). Wideband emission intensities were measured at  $0.9 \mu\text{m} \pm 50 \text{ nm}$  halfwidth and  $1.0 \mu\text{m} \pm 50 \text{ nm}$  halfwidth and transmittance of a laser beam was measured at  $0.632 \mu\text{m}$ .

The three-line probe was a slightly modified version of those used by Gore and coworkers (Sivathanu and Gore, (1992), Sivathanu et al. (1991) and Sivathanu and Gore (1991)) and is shown in Fig. 4-1. The local emission signals were collected by a 6 mm diameter tube which was slightly pressurized by a 1

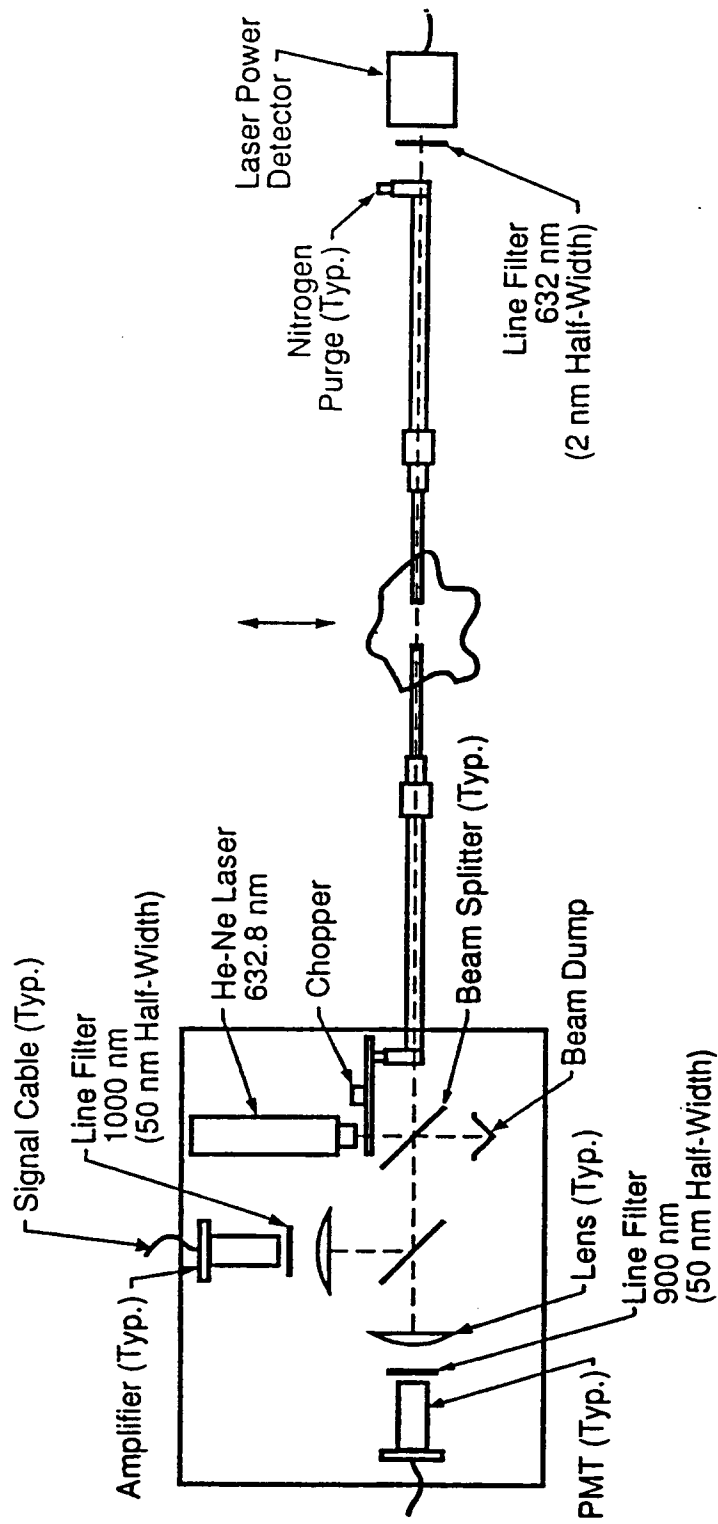


Fig. 4-1 Sketch of three wavelength emission/absorption probe

cc/min flow of nitrogen. The light passed through the window at the exit and through a pair of beam splitters. The first beam splitter only served to send the 0.632  $\mu\text{m}$  laser beam into the optical probe in an opposite direction. The second beam splitter separated the emission beam into two parts which were then incident on the two photomultiplier tubes equipped with the wide band monochromatic filters. The direction of the laser beam was reversed in order to allow the operation of the PMTs at high sensitivity in order to extend the range of temperature estimates to approximately 850 K. The wide band filters (particularly the one at 0.9  $\mu\text{m}$ ) have non-zero transmittance at 0.632  $\mu\text{m}$  leading to interference from the laser light when the PMTs were powered for high sensitivity. Reversing the direction of the laser beam avoided this interference. Since the laser transmittance data were not used in the interpretation of the emission signals, the reversed direction of the two light signals did not affect the results. The laser beam was collected by a second purged probe after passing through the probe volume.

Where ever possible, non-intrusive optical probes are preferred in comparison to the present intrusive probes. However, existing non-intrusive methods are not effective in the present optically thick unsteady flames. Therefore, the effects of the intrusive probes and purge flow on the local properties and effects of the probe heat up on the signal were evaluated by Sivathanu et al. (1991).

The local temperature and mean species concentrations were affected by less than 5% by the introduction of the probe as summarized in Sivathanu et al. (1991). The nitrogen purge flow was photographically observed to produce 1 mm thick dark zones on the surface of the probes. Measurements at representative locations with double the purge flow rate (2 cc/min) showed less than 5% differences in the emission intensities and absorption transmittances providing an estimate of the errors.

A stainless steel plate was used to cover the front end of the receiving probe to observe the effect of probe heat up with the flame in place on the signal at the end of each measurement. If the signal due to probe heat up exceeded 5 % of the local mean emission signal, the measurements were repeated with shorter data collection time but more repetitions. The maximum data collection times were less than 5 minutes due to the above probe heat up criterion.

The signals collected by the PMTs and the laser power meter were amplified and processed through eighth order antialiasing analog Butterworth filters set at 125 Hz before sampling by an A/D converter and a laboratory computer at 250 Hz for post-processing. A minimum of 5000 data points (occasionally from different realizations due to probe heat up limitations) were used to obtain averages. The sampling frequency was determined by power spectral analyses of the signals from representative locations. The sensitivity of the optics and the detectors was calibrated using a commercial blackbody operated at 1273 K before and after each test. The

two probes serve as relatively cold background for each other.

#### 4.2.3 Data Analysis

##### 4.2.3.1 Emission/Absorption Data

The laser transmittance signals were used to estimate the soot volume fractions using the Rayleigh limit for small particles. Past multiline measurements (Gore and Faeth, (1988)) have suggested that this approximation is adequate for the present flames. Following Tien and Lee (1982), the soot volume fractions were calculated as:

$$f_{va} = -\ln(I_\lambda/I_\lambda^0) \lambda / K_\lambda S \quad (4-1)$$

The argument of the natural log in Eqn. 4-1 is the measured transmittance. "S" is the separation distance between the probes. The separation distance was 10 mm. The constant  $K_\lambda$  in Eqn. 4-1 involves the complex refractive index of the soot particles ( $n-ik$ ) at the measurement wavelength (Dalzell and Sarofim (1969)):

$$K_\lambda = \frac{36\pi nk}{(n^2 - k^2 + 2)^2 + 4n^2k^2} \quad (4-2)$$

The complex refractive index of soot particles has been measured by several investigators and considerable discussion of the effects of temperature, fuel type and wavelength exists in the current literature (see Sivathanu et al. (1990) and Sivathanu et al. (1991) for example). Consistent with earlier work (see Sivathanu et al. (1990) and Sivathanu et al. (1991)), the values given by Dalzell and Sarofim (1969) were used resulting in  $K_\lambda = 4.89$  at a wavelength of  $0.632 \mu\text{m}$ . The soot volume fractions obtained from Eqn. 4-1 are designated as  $f_{va}$  to indicate that these were obtained from an absorption measurement.

The interference filters associated with the emission detectors have a relatively large spectral width ( $\pm 50 \text{ nm}$  at half peak) requiring the use of integration over the filter transmittance curve. The intensities measured by the emission detectors are related to the local properties as:

$$I_\lambda = \frac{\int_{\lambda_1}^{\lambda_2} (1 - \tau_\lambda) F_\lambda I_{b\lambda} d\lambda}{\int_{\lambda_1}^{\lambda_2} F_\lambda d\lambda} \quad (4-3)$$

where  $\tau_\lambda$  is the monochromatic transmittance of the material in the probe volume over the probe length  $L$ ,  $F_\lambda$  is the characteristic transmittance curve of the interference filter with lower and upper cutoff wavelengths of  $\lambda_1$  and  $\lambda_2$ .  $I_{b\lambda}$  is Planck's function at the probe volume temperature  $T$ :

$$I_{b\lambda} = \frac{2hc^2}{\lambda^5 (\exp(hc/\lambda k_B T) - 1)} \quad (4-4)$$

For the emission measurements at  $0.9$  and  $1.0 \mu\text{m}$ , the soot

particles in the probe volumes were the dominant contributors to the emission intensity and hence  $\tau_\lambda$ . Therefore for these two wavelengths the transmittance in Eqn. 4-2 was equated to the transmittance due to soot particles:

$$\tau_{\lambda s} = e^{-\frac{K_\lambda f_{ve} S}{\lambda}} \quad (4-5)$$

where  $K_\lambda = 5.58$  for  $\lambda = 0.9 \mu\text{m}$  and  $K_\lambda = 5.47$  for  $\lambda = 1.0 \mu\text{m}$  are constants dependent on the refractive index of soot [20]. Since  $h$ ,  $c$  and  $k_B$  are fundamental constants and  $K_\lambda$  for  $\lambda = 0.9 \mu\text{m}$  and  $\lambda = 1.0 \mu\text{m}$  are known, Eqns. 4-2- 4-4 for these two wavelengths were solved for the two unknowns - temperature  $T$  and soot volume fractions based on emission -  $f_{ve}$ . Due to the integral nature of Eqn. 4-2, an iterative solution must be obtained.

If the soot particles in the probe volume had a uniform temperature then the measurements soot volume fractions based on absorption and those based on emission would be identical. If the temperatures of the soot particles were different, then  $f_{ve}$  represents a Planck function weighted average of all the particles. Therefore,  $f_{ve}$  is biased towards the hottest soot particles in the probe volume while  $f_{va}$  is a measure of all soot particles.

As summarized in Sivathanu et al. (1991), the absolute uncertainties of the present data depend on the values of refractive indices for the soot particles. For a fixed set of refractive indices, the uncertainties in the mean temperatures are less than 40 K for  $f_{ve}$  above 0.1 ppm and increase to 80 K for  $f_{ve} = 0.01$  ppm. The uncertainties in  $f_{va}$  data are less than 10% at 10 ppm and increase to 40% at 0.01 ppm due to digitization errors. The uncertainties in the emission soot volume fractions are dominated by the choice of the refractive indices and are estimated to be 30 % at 1400 K and  $f_{ve} = 1$  ppm. The uncertainties in the measurements of RMS values were estimated by repeating the measurements at several representative locations. The uncertainties in RMS temperatures varied between 70 and 150 K, the uncertainties in RMS measurements of  $f_{va}$  varied between 25% at 10 ppm to 100 % at 0.01 ppm. The uncertainties in the RMS  $f_{ve}$  data are estimated to be less than 40% based on repeated measurements at representative locations.

At several axial locations in the flame, monochromatic radiation intensity measurements were completed for progressively larger probe volume lengths. These measurements were accomplished by increasing the distance between the probes, at intervals of 10 mm, from the initial distance of 10 mm until the entire flame width was within the probes. Mean and RMS monochromatic radiation intensities are then obtained as function of radiation path length. This procedure allows an examination of the individual terms in the equation of radiative transfer with emphasis on turbulence-radiation interactions.

#### 4.2.3.2 Turbulence-Radiation Interactions

The radiation intensity and heat flux to surrounding locations leaving the flame depend on the contributions from all the local segments. The local measurements were obtained with a resolution of 10 mm. Whether this spatial resolution is adequate for the estimate of radiation intensity depends on the local turbulence length scales.

If average temperature and soot volume fractions are used in the calculation of the emission intensity using Eqn. 2, the effects of nonlinear dependence of Planck's function on temperature and the nonlinear dependence of transmittance on soot volume fractions can cause significant errors. Furthermore, cross correlations between  $\tau_{\lambda}$  and  $I_{b\lambda}$  are neglected by this approach. The relative importance of these nonlinearities needs to be examined for pool fires.

A third consideration of the turbulent properties involves the spatial correlations between the scalar properties at adjoining and separated segments. Since instantaneous, multi-point data are not available, only inferences concerning the adequacy of the present single point data can be drawn.

#### 4.2.3.3 Frequency Analysis

In order to examine these mechanisms, the instantaneous equation of radiative transfer is averaged to obtain equations for mean and mean square intensities at various points. The results of these equations were compared with experimental data for a representative diametric radiation path at  $x/D = 0.8$  in the flame. Fig. 4-2 shows the representative radiation path highlighting the contribution of intensity emitted at segment M to the intensity leaving segment N.

The instantaneous equation of transfer is represented as:

$$I_{\lambda}(N) = \sum_{M=1}^N I_{\lambda_e}(M) \prod_N^{J=M+1} \tau_{\lambda_e}(J) \quad (4-6)$$

where "N" represents the intensity measurement position and "M" represent the individual radiation segments. This formulation requires that the cross correlation between  $\tau_{\lambda_e}$  and  $I_{\lambda_e}$  be known. In order to treat the effects of turbulence on the radiation intensity reaching the detector location "N" accurately, simultaneous estimates of emissive power at the segment "M" and absorption transmittances at all intervening segments "M+1" to "N" would also be required. For the purpose of calculating average intensity, estimates of length scales and two-point correlation coefficients between  $I_{\lambda_e}(M)$  and  $(\tau_{\lambda_e}(J), J=M+1, N)$  are sufficient. However, measurements of these quantities are unavailable. To overcome this deficiency, the length of the radiation segments must be chosen such that it exceeds the local integral length scale.

In order to study the mean square intensity fluctuations, the instantaneous emission intensity for segment M and the instantaneous emission transmittance for segment J are transformed following the Reynolds' decomposition more commonly used in fluid dynamics:

$$\begin{aligned}
I_{\lambda_e}(M) &= \overline{I_{\lambda_e}(M)} + I'_{\lambda_e}(M) \\
\tau_{\lambda_e}(J) &= \overline{\tau_{\lambda_e}(J)} + \tau'_{\lambda_e}(J)
\end{aligned}
\tag{4-7}$$

For clarity, the transmittance across the radiation segment length is taken as:

$$\tau_{\lambda_e}(M, N) = \prod_{J=M+1}^N \tau_{\lambda_e}(J)
\tag{4-8}$$

After Reynolds' averaging, the mean equation of transfer becomes:

$$\overline{I_{\lambda}(N)} = \sum_{M=1}^N \overline{I_{\lambda_e}(M)} \overline{\tau_{\lambda_e}(M, N)}
\tag{4-9}$$

and that for mean squared intensity fluctuations becomes:

$$\begin{aligned}
\overline{(I'_{\lambda})^2(N)} &= \sum_{M=1}^N \overline{((I'_{\lambda_e})^2(M))} [\overline{\tau_{\lambda_e}(M, N)}]^2 + [\overline{I_{\lambda_e}(M)}]^2 \overline{(\tau'_{\lambda_e}(M, N))^2} \\
&\quad + \overline{I'_{\lambda_e}(M)^2 (\tau'_{\lambda_e}(M, N))^2} + 2 \overline{I'_{\lambda_e}(M)^2 (\tau'_{\lambda_e})(M, N)} \overline{\tau_{\lambda_e}(M, N)} \\
&\quad + 2 \overline{I_{\lambda_e}(M) I'_{\lambda_e}(M) (\tau'_{\lambda_e})^2(M, N)} + 2 \overline{I_{\lambda_e}(M) I'_{\lambda_e}(M) (\tau'_{\lambda_e}(M, N))} \overline{\tau_{\lambda_e}(M, N)}
\end{aligned}
\tag{4-10}$$

Turbulence-radiation interactions in flames originate in the non-linearities inherent in the processes of radiative transfer (Eqns. 4-4 and 4-5). The non-linearity in the equation of transfer is a result of Planck's function ( $I_{b\lambda}$ ) and of monochromatic transmittance ( $\tau_{\lambda}$ ) (see Eqn. 5) that determines the local emission properties. The calculation of mean spectral intensity (Eqn. 4-9) is comprised of the mean transmittance of local mean spectral emission intensity along the radiation path length. Any effects of the fluctuation of emission properties on mean spectral intensity would become important only if the fluctuations change the mean transmittance and mean emission intensity. The calculation of the RMS equation of transfer (Eqn. 4-10) includes two 2<sup>nd</sup> moment terms, three 3<sup>rd</sup> moment terms and one 4<sup>th</sup> moment term. Fluctuating emission properties are seen in every term of this equation and should be an important element in the calculation of RMS intensity. The equations of the mean and RMS equation of transfer (Eqns. 4-9 and 4-10) will be examined to assess the validity of the assumption used to overcome the lack of spatial correlations for the transmittance and the assumption that  $I'_{\lambda_e}(M)$  and  $\tau'_{\lambda_e}(J)$  are independent. Predictions of mean and RMS monochromatic intensity using Eqns. 4-9 and 4-10 and local flame emission data are evaluated by comparison with monochromatic intensity measurements for segments of diametric radiation path shown in Fig. 4-2.

#### 4.2.3.4 Frequency Content of Emission Properties

The turbulence radiation interactions originate in

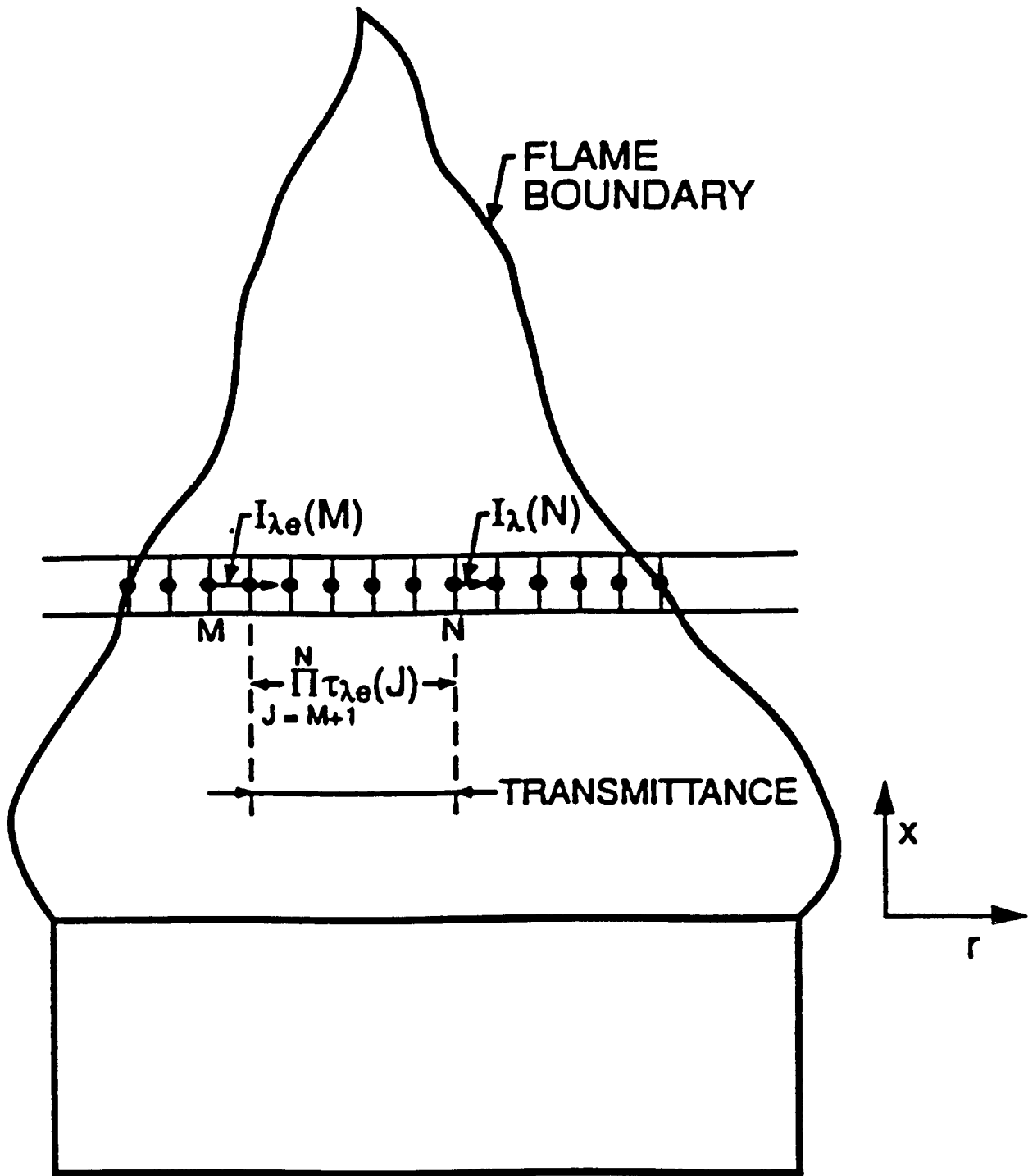


Fig. 4-2 Sketch of a radiation path and discretization grid for the equation of radiative transfer.

fluctuating quantities  $I'_{\lambda e}$  and  $\tau'_{\lambda e}$  and indirectly in  $T'$  and  $f'_{ve}$ . These fluctuations have a frequency content determined by the local state of turbulence. Fluctuations within a range of frequencies are expected to contribute significantly to the effects on mean and RMS intensities. For deciding the time resolution needed for numerical simulations and experimental measurements, knowledge regarding this range of frequencies is important. Gaussian filters were used to find the influence of frequency content of local transient data on mean and RMS intensities for the representative path.

Data with low frequency content are obtained by using a weighted average of neighboring data points. For example, intensity at time  $t$  is obtained by:

$$I_{\lambda e}(t) = \sum_{\Xi-t-J\Delta t}^{\Xi-t+J\Delta t} W(J) I_{\lambda e}(\Xi)$$

where the weight  $W(J)$  has a Gaussian form given by:

$$W(J) = \frac{1}{\sqrt{2\pi\sigma^2}} \exp\left[-\frac{(J\Delta t)^2}{2\sigma^2}\right]$$

where  $\Delta t = 1/(\text{sampling frequency of the data})$  and  $\sigma$  is the standard deviation. The value of  $\sigma$  determines the cutoff frequency of the filter.

Fig. 4-3 shows the effect of different  $\sigma$  on the frequency content of filtered white noise. Normalized power spectral densities (PSD) are used to determine the frequency cut off level corresponding to each  $\sigma$ . This cutoff is taken as the frequency where the energy content of the PSD begins to drop sharply. From Fig.4-3, the frequency cutoffs for  $\sigma = 3, 10,$  and  $15$  were found to be  $21 \text{ Hz}, 10 \text{ Hz},$  and  $8 \text{ Hz}$  respectively. Having characterized the filter for different  $\sigma$ , its effect on turbulent radiation interactions can now be studied.

#### 4.2.4 Operating Conditions

The operating conditions are described in Table 2-2. Toluene was the fuel used due to its strongly radiating nature. The relatively low velocities of the vapor at the liquid surface result in complete dominance of the flame by buoyancy. The Froude numbers for the present flames at the burner surface are higher by over two orders of magnitude compared to the acetylene-fired pool flames of Sivathanu et al. (1991) and Sivathanu and Gore (1992) allowing a study of flame radiation in a different regime. Use of toluene as the fuel also separates the effects resulting from peculiar chemistry of acetylene from those resulting from strong radiative heat loss. The mass burning rates were measured by monitoring the output of a load cell mounted under the fuel reservoir. The heat release rate is based on complete combustion to stable products. The global radiative loss fraction is much lower than those of the acetylene/air pool flames in spite of comparable soot volume fractions.

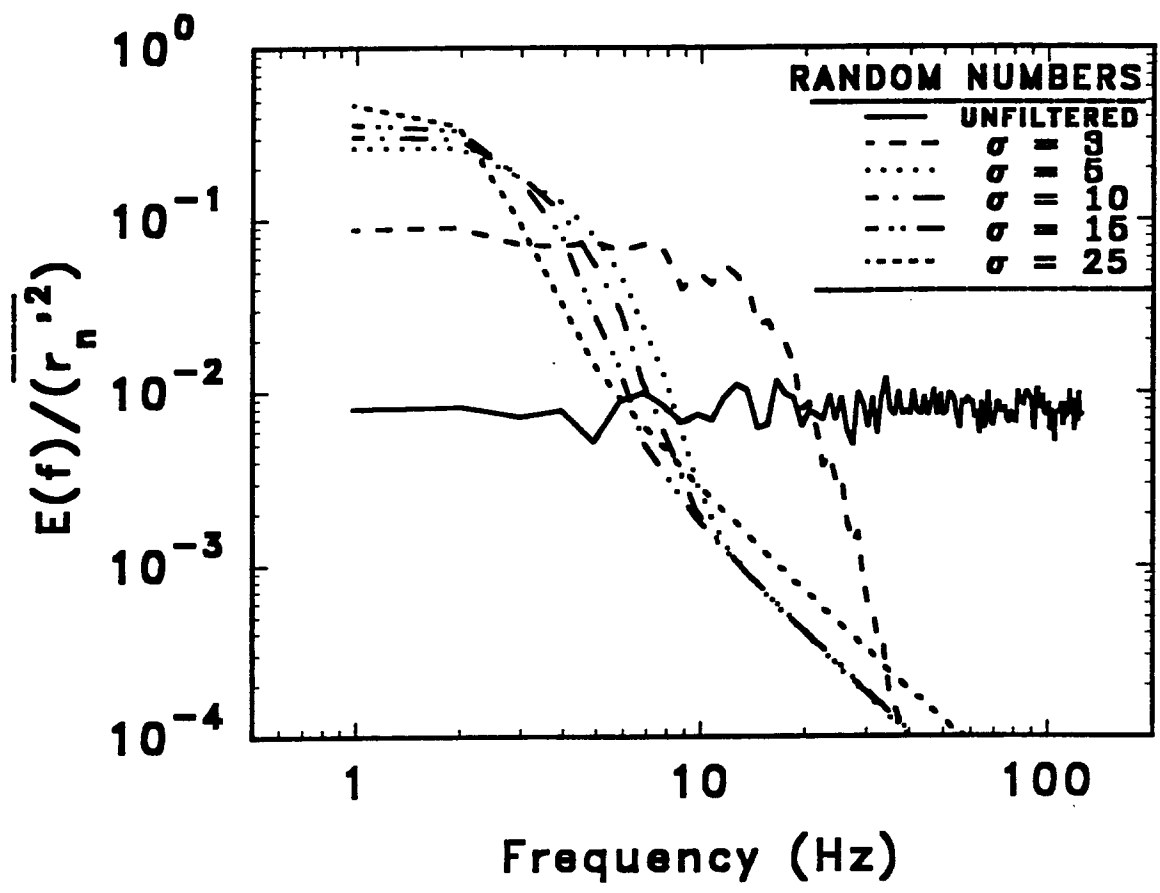


Fig. 4-3 Power spectral density of filtered white noise

### 4.3 Results and Discussion

#### 4.3.1 Mean and RMS Properties

The mean and RMS intensities at 0.9 and 1.0  $\mu\text{m}$  and transmittance at 0.632  $\mu\text{m}$  are discussed prior to the temperatures and soot volume fractions in the flame.

Fig. 4-4 shows mean and RMS emission intensities at 0.9 and 1.0  $\mu\text{m}$  as a function of normalized distance from the geometric axis of the pool for three positions ( $x/D = 0.2, 0.4$  and  $0.8$ ) relatively close ( $H_f/D = 4.2$ ) to the liquid surface. These three locations are in the visually persistent flame region. The mean intensities at 1.0  $\mu\text{m}$  are higher than those at 0.9  $\mu\text{m}$  consistent with the expected flame temperature limits. At  $x/D = 0.2$ , a narrow flame sheet appears near the pool edge (pool edge at  $r/D = 0.5$ ; flame sheet at  $r/D = 0.42$ ). The local emission intensities near the pool center are very low for this lowest axial station. The region of high intensity is quite narrow at this position. The RMS values near the peak intensity are approximately 50% for  $\lambda = 1.0 \mu\text{m}$  and 60% for  $\lambda = 0.9 \mu\text{m}$ . These are high RMS values and probably originate from the flapping of the flame sheet near the liquid surface. As the distance from the liquid surface is increased the high intensity region moves closer to the pool center. The peak mean intensities at  $x/D = 0.4$  are approximately 25% lower than those at  $x/D = 0.2$ . The reduction can be attributed to two different reasons, first, the increased RMS values due to increased visible flame motion (over 100% for both 0.9 and 1.0  $\mu\text{m}$ ) and second the larger time available for heat loss by radiation to the surroundings. The region of measurable emission intensities broadened by a factor of 2 between these two stations. At  $x/D = 0.8$ , the maximum mean intensity decreases to 75% of that at  $x/D = 0.4$ . For both positions, the RMS fluctuations are close to 100% near the center and well over 100% for the edge locations. The decrease in the maximum mean intensity between  $x/D = 0.4$  and  $x/D = 0.8$  appears to be due to the effect of radiative cooling. The width of the measurable mean intensity zone now extends across the entire flame width possibly signifying a transition from a nearly laminar flapping flame sheet at the lower positions to a turbulent ensemble of flamelets moving across the entire width of the jet.

Fig. 4-5 shows the mean and RMS intensities at 0.9 and 1.0  $\mu\text{m}$  for three positions above the persistent flame region. Two of the positions are just below the mean visible flame height ( $H_f/D = 4.2$ ) while the third is just beyond this location. The flame at these farther locations is wider than the three positions shown in Fig. 4-4 (note the different scale of  $r/D$  on the abscissa). For  $x/D = 2.5$  and  $3.5$  positions, the peak mean intensities are comparable to those seen at the three lower positions. At  $x/D = 4.5$ , the peak mean intensity has decreased substantially, characteristic of the sharp visible flame edge exhibited by these flames. The RMS fluctuations are much higher at all three positions varying between 100% and 250% of the mean intensities. These high RMS values are direct

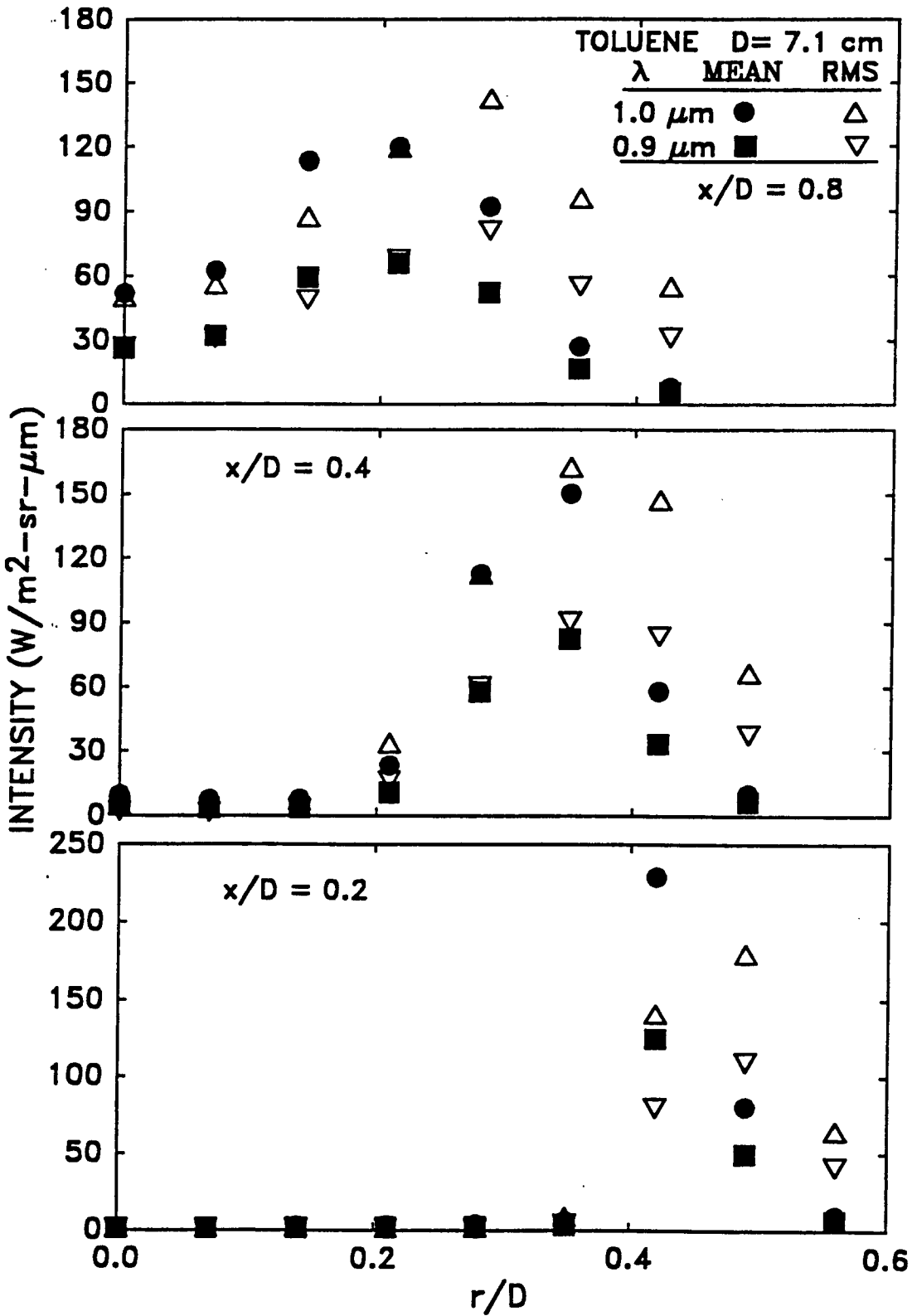


Fig. 4-4 Radial distributions of mean and RMS wideband spectral radiation intensity at  $\lambda = 0.9$  and  $1.0 \mu\text{m}$  for locations near the flame base

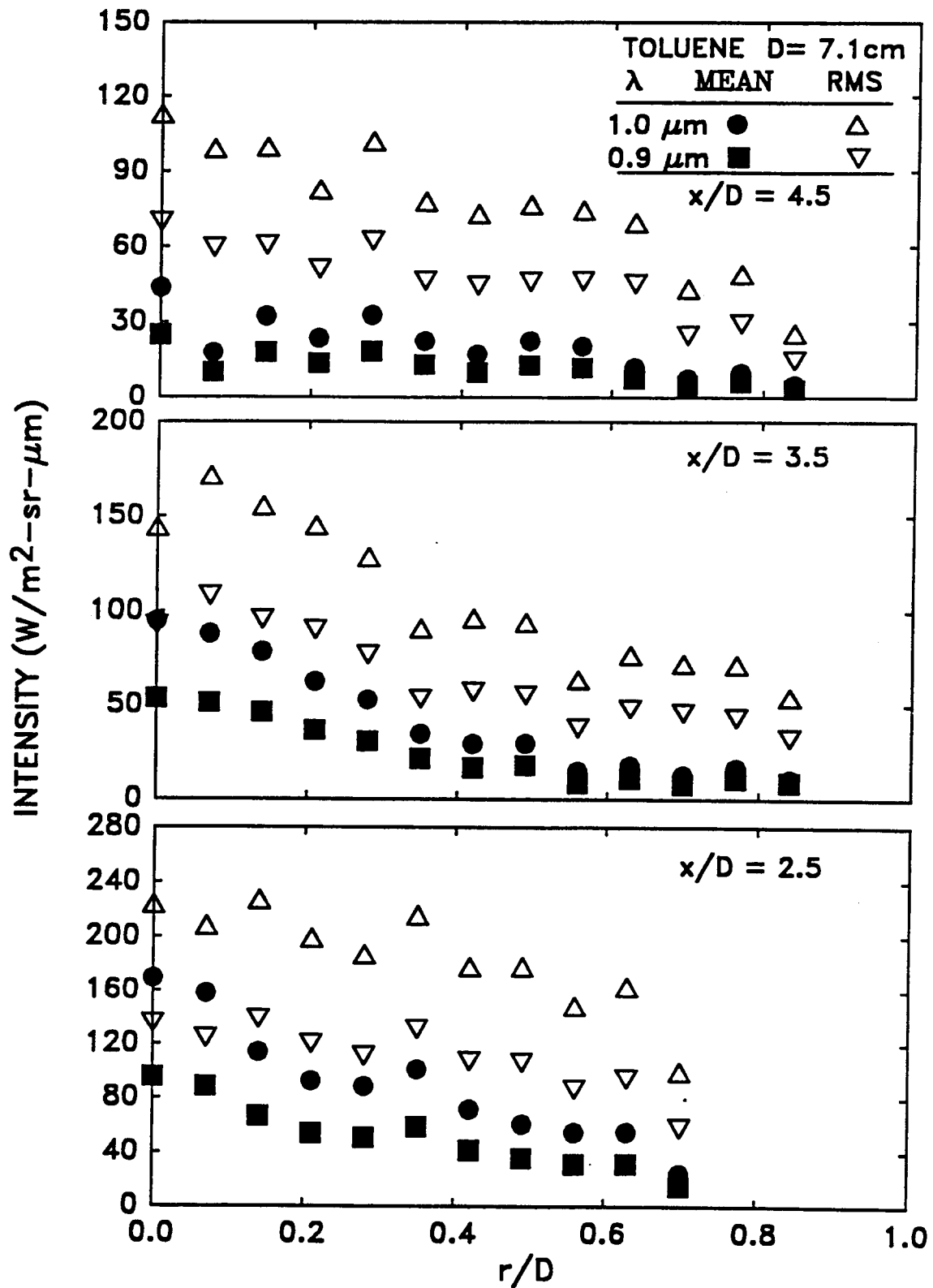


Fig. 4-5 Radial distributions of mean and RMS wideband spectral radiation intensity at  $\lambda = 0.9$  and  $1.0 \mu\text{m}$  for locations near the flame tip

evidence of the effects of turbulent fluctuations on local emitted intensities in the highly buoyant flames.

Fig. 4-6 shows the radial distributions of mean and RMS transmittance for three stations ( $x/D = 0.2, 0.4$  and  $0.8$ ) in the persistent flame region. Consideration of identical stations in Figs. 4-4 and 4-6 allows a comparison of the similarities and differences in the local absorption and emission properties. The mean transmittance at the position near the liquid surface is less than unity for positions inside of the flame sheet. Visually, a cloud of soot particles was observed to move up and down with a low frequency motion at this station. These particles do not emit visible radiation as seen in Fig. 4-4 and therefore appear to be relatively cold. As the region near the flame sheet ( $r/D = 0.42$ ) is approached, the transmittance decreases rather sharply to around 0.6 indicating the presence of soot particles. It is noted that these particles appear to contribute to the emission intensity based on a peak at this location observed in Fig. 4-4. Comparison of the transmittance and emission-intensity distributions at  $x/D=0.4$  is even more interesting. At the first four radial positions near the center at this axial station, the mean transmittance based on absorption is near 0.5 and relatively constant indicating the presence of a large volume fraction of soot. A comparison of these data with those of emission intensity (shown in Fig. 4-4) indicates that these soot particles are emitting very low intensity light. At the radial locations ( $r/D = 0.35$ ) where the emission intensities do increase considerably (change of a factor of over 30), the transmittance based on absorption also increases to 0.8. This behavior indicates a negative correlation between  $f_{ve}$  and temperature. The next measurement location ( $r/D=0.42$ ) has an absorption transmittance of 0.95 but still a relatively high emission intensity (factor of 10 higher than the central region) based on Fig. 4-4. At the last measurement station in the persistent flame region ( $x/D=0.8$ ), the transmittance is lowest at the center (similar to that at  $x/D=0.4$ ) and then increases continuously towards the edge. The mean transmittance of 0.4 observed at the center-line at this position is the lowest measured mean transmittance in this flame. Comparison of the radial distribution of mean transmittance at this position with that of the visible emission intensities (Fig. 4-4) shows that near the centerline, the lowest intensity occurs with the lowest transmittance. The transmittance and the intensity increase with radius until the intensity reaches a peak value at  $r/D=0.2$ . At positions farther than  $r/D=0.2$  from the axis, the mean intensity decreases while the mean transmittance continues to increase and as expected reaches a value of 1 in the region outside the flame. Based on the structure of diffusion flames, it is expected that temperature (and emission intensity) would reach a maximum at a certain mixture fraction and decrease on both fuel rich and fuel lean side. However, whether the distributions seen in Figs. 4-4 and 4-6 can be explained by

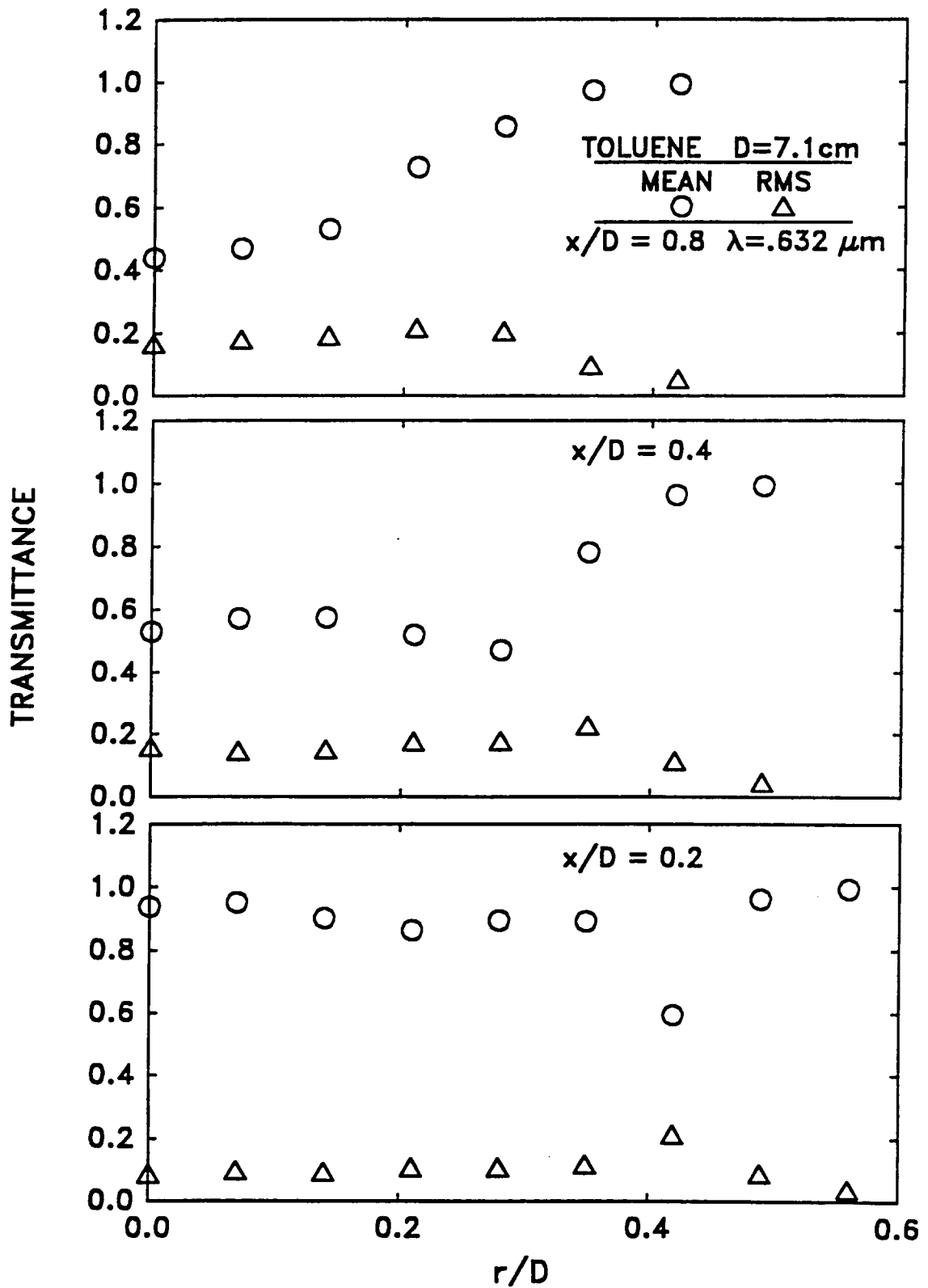


Fig. 4-6 Radial distributions of mean and RMS wideband spectral radiation intensity at  $\lambda = 0.632 \mu\text{m}$  for locations near the flame base

the conventional diffusion flame structure (which does not account for the strong local radiative heat loss for highly sooty regions) is not clear. The RMS fluctuations in transmittance are between 0.1 and 0.2 which ranges between 10 to 50 % of the mean. The reason for these lower values compared to the RMS values of emission intensity is discussed later.

Fig. 4-7 shows the radial distribution of transmittance for the three axial locations nearer the flame tip. The transmittance values are much higher than those seen in Fig. 4-6 for the positions in the persistent flame region. The mean transmittances vary slowly with radial position consistent with the emission intensity profiles seen in Fig. 4-5. For this region near the flame tip, a comparison of the emission intensity and transmittance profiles shows that the emission intensity and transmittance change inversely with each other. This behavior originates from the higher sensitivity of emission intensity to temperature than soot volume fractions and is typical of the fuel lean regions in Figs. 4-4 and 4-6 as well. It is noted that the RMS fluctuations in transmittance are approximately 10-25% which are considerably lower than the RMS fluctuations in emission intensity (100 - 300%) seen in Fig. 4-5 for these axial stations. These data imply that the emitting material exists in the probe volume much more intermittently than the absorbing material.

The emission intensity measurements summarized above in terms of mean and RMS values are interpreted in terms of emission temperatures and soot volume fractions based on emission in Figs. 4-8 to 4-11. The transmittance data based on absorption are interpreted in terms of the soot volume fractions in Figs. 4-10 and 4-11.

Fig. 4-8 shows the radial distribution of mean emission temperature at the three axial positions in the persistent flame region. In calculating the mean and RMS emission temperatures, the readings below the detection limit of the PMTs (850 K) have been set to 300 K. This procedure causes a downward bias in the mean temperatures and an upward bias in the RMS temperatures in the regions of high intermittency in the emission signal.

For radial positions lower than  $r/D = 0.3$  at the lowest axial station shown in Fig. 4-8, the emission intensity never goes above the detection limit of the PMTs. Therefore, this region can be classified as relatively cold (at a mean temperature of 300 K as per the present technique). The mean temperature increases to approximately 1200 K near  $r/D = 0.42$  which is the mean location of the flame sheet. At  $x/D = 0.4$ , the mean temperature near the center is again close to 300 K and increases to approximately 1000 K near the flame sheet position at  $r/D = 0.35$ . At this axial station, the radial distance traversed by the flame sheet is larger than that at  $r/D = 0.2$ . The RMS temperature fluctuations increase to 40% as a result of this motion. Towards the end of the persistent flame region at  $x/D = 0.8$ , the mean temperature varies between 900 K and 1100 K for a radial distance of  $r/D = 0.2$  before

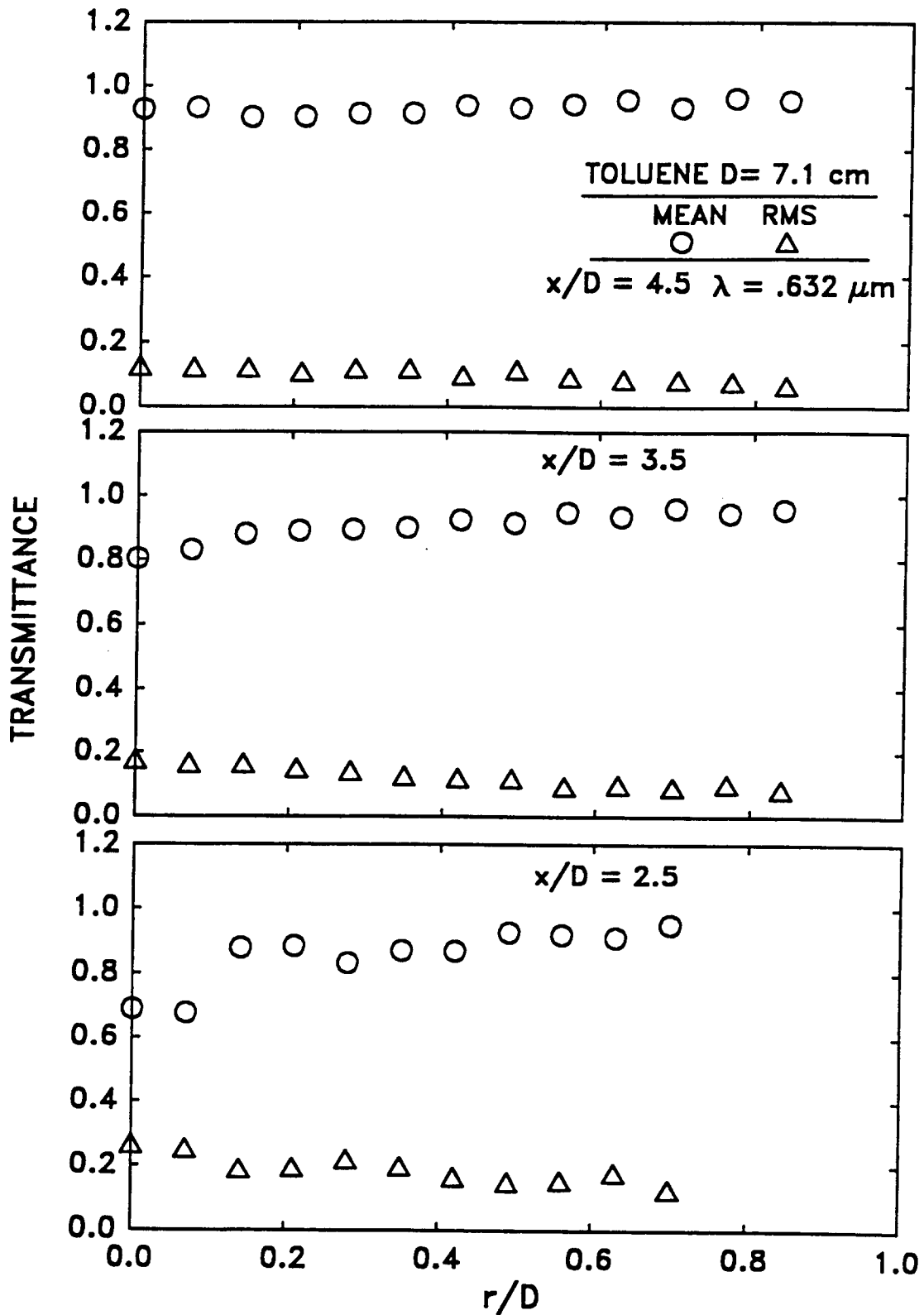


Fig. 4-7 Radial distributions of mean and RMS wideband spectral radiation intensity at  $\lambda = 0.632 \mu\text{m}$  for locations near the flame tip

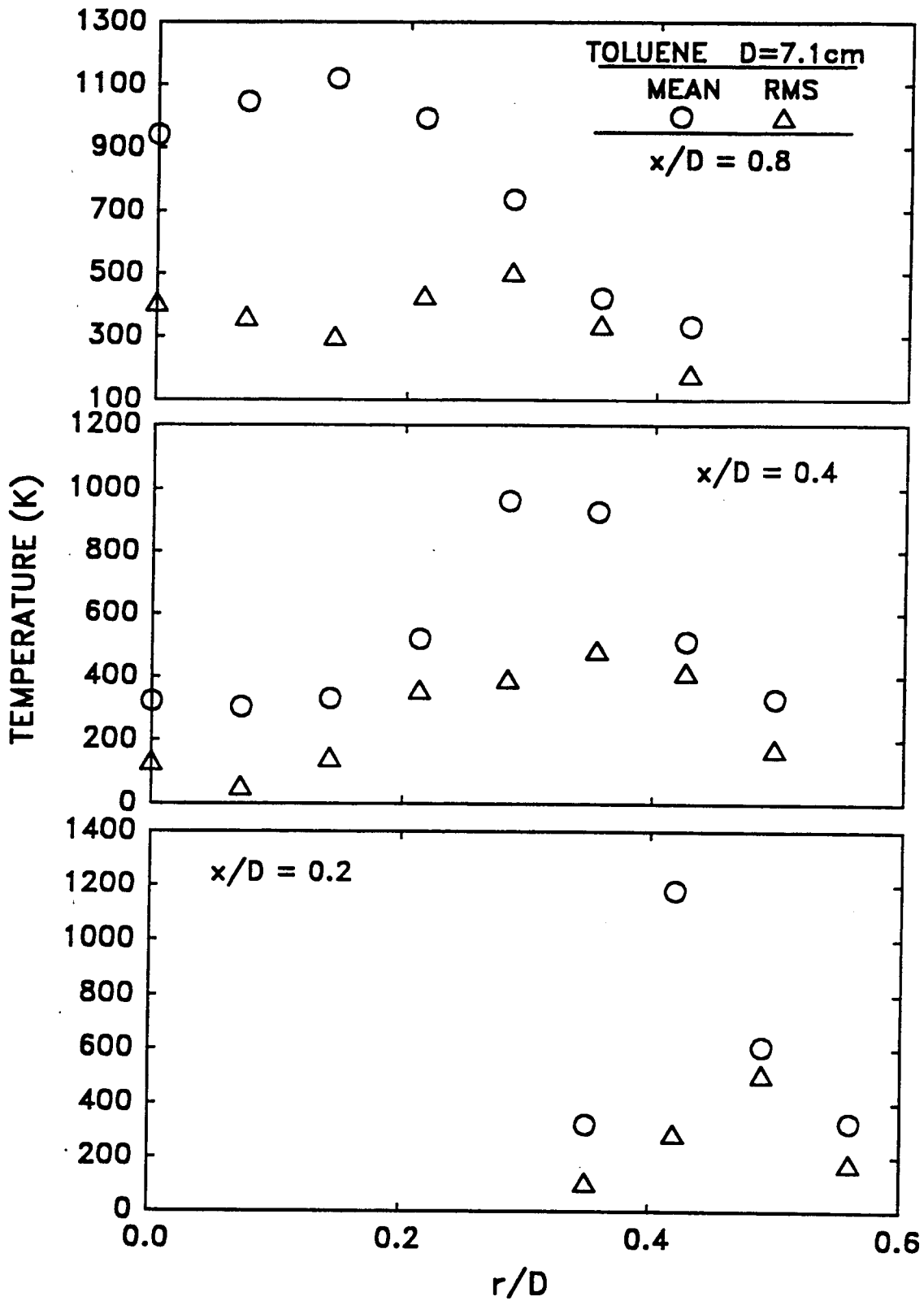


Fig. 4-8 Radial distributions of mean and RMS two line emission temperatures for locations near the flame base

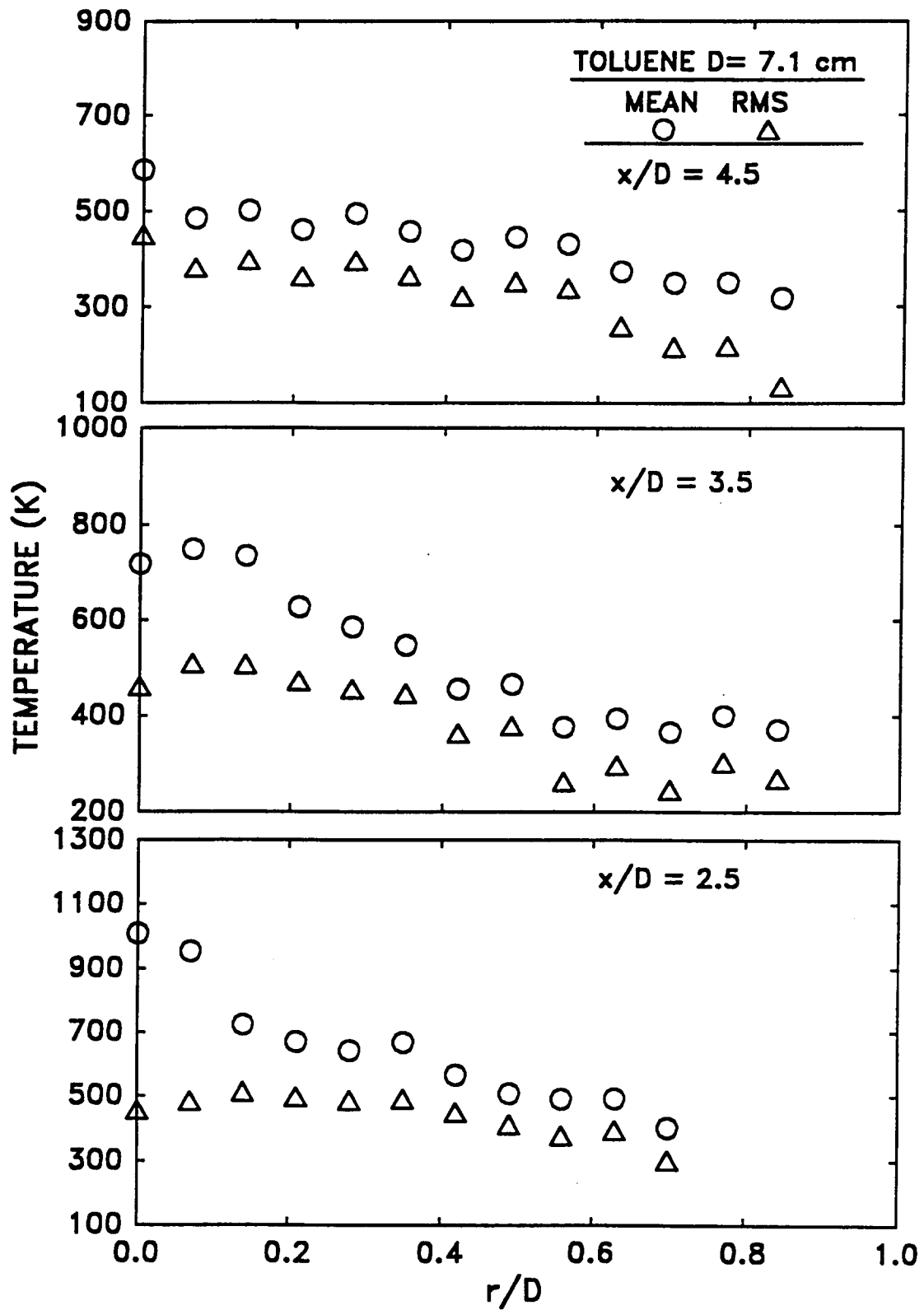


Fig. 4-9 Radial distributions of mean and RMS two line emission temperatures for locations near the flame tip

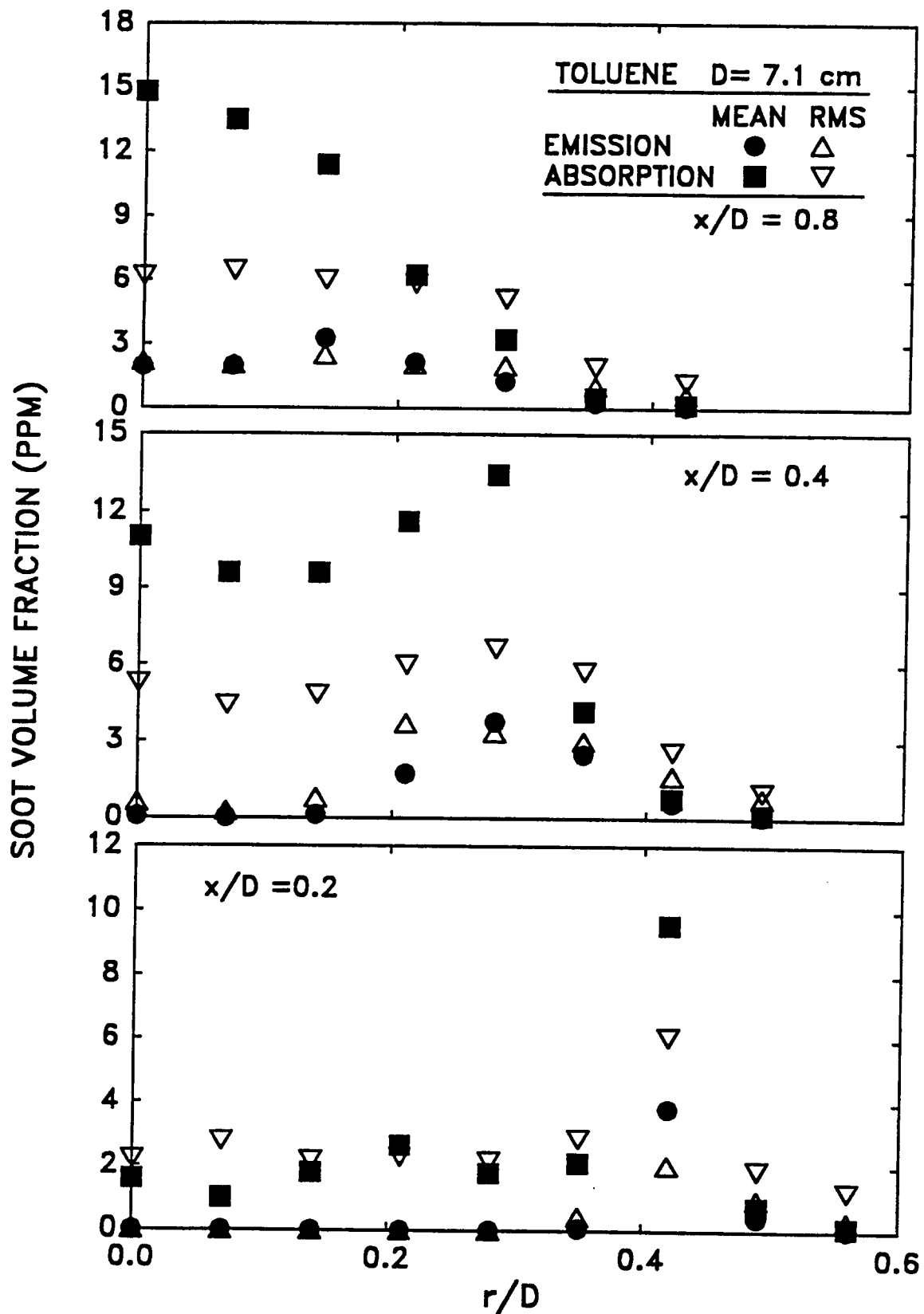


Fig. 4-10 Radial distributions of mean and RMS soot volume fractions based on emission and absorption data near the flame base

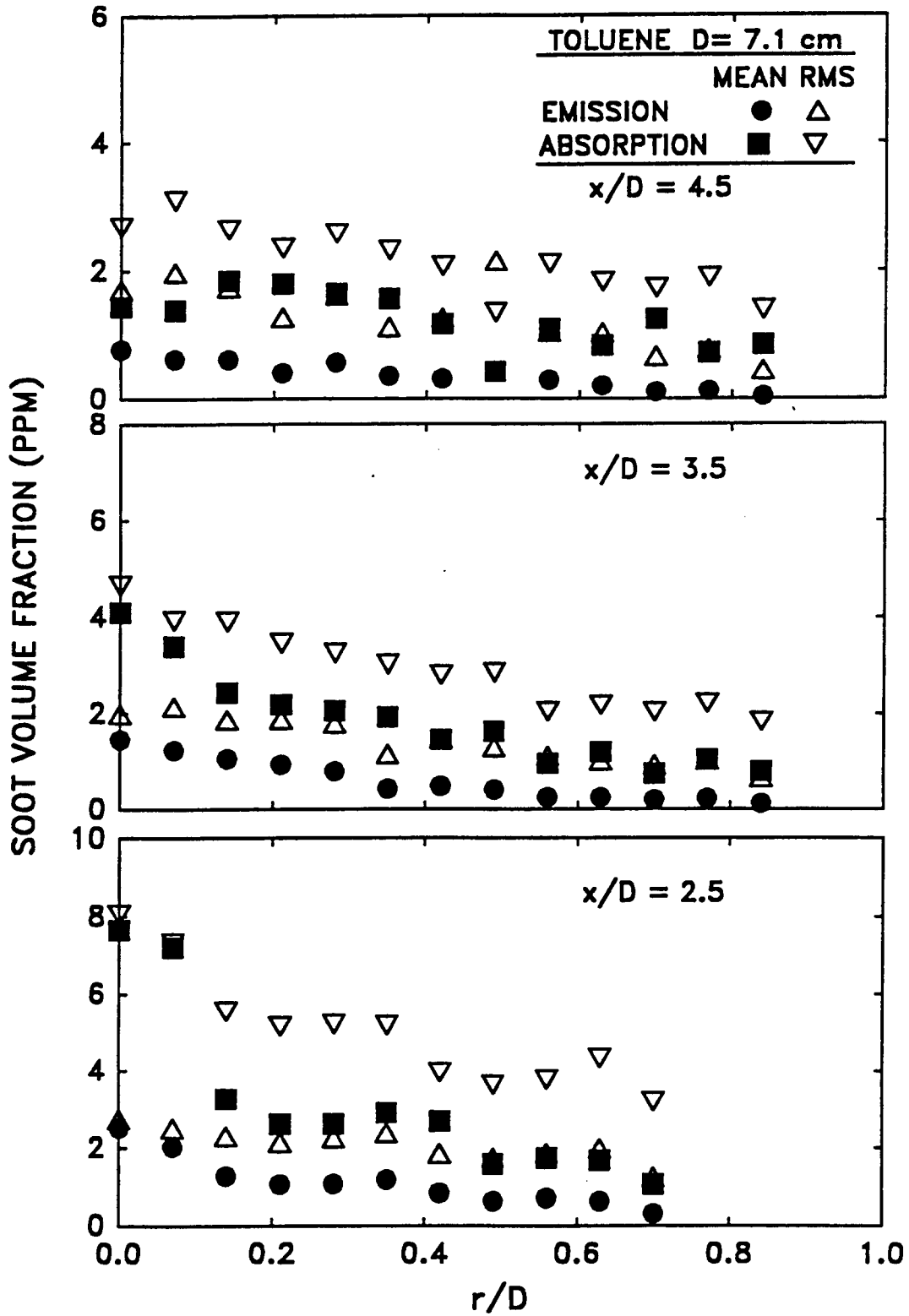


Fig. 4-11 Radial distributions of mean and RMS soot volume fractions based on emission and absorption data near the flame tip

beginning a fast decline in the edge region. The RMS fluctuations in temperature vary between 400 K to 500 K. As seen in Fig. 4-4, these translate into up to 100% RMS variations in the emission intensities.

The mean and RMS temperature distributions at three axial positions nearer to the flame tip are plotted as a function of normalized radial position in Fig. 4-7. The temperatures peak near the axis for all three positions and decrease continuously to the edge. The RMS of temperature fluctuations are around 500 K at all three positions. At the highest position ( $x/D = 4.5$ ) these happen to be almost 80% of the mean temperature level leading to the large variations in intensities that were observed in Fig. 4-5. These large fluctuations occur due to intermittent behavior of the fire at these axial positions.

Fig. 4-10 shows the radial profiles of mean and RMS soot volume fractions based on emission and absorption for the three positions closer to the fuel surface. The absorption soot volume fractions are a true measure of the volume fraction of soot particles in the probe volume while the emission soot volume fractions are a measure of volume fractions of relatively hot soot particles. If all soot particles in the probe volume are at the same temperature, the absorption and emission soot volume fractions data should collapse within experimental uncertainty limits. Fig. 4-10 shows that at all positions in the persistent flame region, the soot volume fractions based on absorption are substantially larger than those based on emission indicating that a large portion of the soot particles are at temperatures too low to contribute significantly to the emission intensity. At the lowest positions ( $x/D = 0.2, 0.4$ ), the soot particles near the axis seen by the absorption probe (mean of 2 and 11 ppm) are not seen by the emission probes at all. These particles appear as a dark layer near the liquid surface and are relatively cold. Presence of large quantities of cold soot particles near the surface are expected to affect the heat feedback due to blockage. The RMS fluctuations in soot volume fractions are typically close to 100 %. Such high fluctuations suggest a large level of intermittency in the appearance of soot particles associated with soot streaks.

The radial distributions of mean and RMS soot volume fractions based on absorption and those based on emission at three positions in the region near the flame tip are shown in Fig. 4-11. At all three positions ( $x/D = 2.5, 3.5$  and  $4.5$ ) the values of soot volume fractions based on absorption are substantially higher than those based on emission indicating the presence of large amounts of relatively cold soot in these regions. The differences between the two measurements decrease with axial position probably because the hot soot particles that contribute to the emission soot at positions near the liquid surface are now at a lower temperature due to preferential radiation heat loss. Far away from the flame tip, it is expected that the soot particles in the exhaust stream reach an isothermal condition with low temperature. Under such

conditions the differences between the measurements of soot volume fractions based on absorption and emission will increase again since  $f_{ve}$  will approach zero and  $f_{va}$  will attain a value corresponding to the soot emitted in the exhaust stream. The RMS values of soot volume fractions shown in Fig. 4-11 are comparable to those in Fig. 4-10. This results from a combined effect of mixing with ambient air that diffuses the soot streaks and the increased turbulence intensity in this far-field region.

#### **4.3.2 Emission Statistics**

##### **4.3.2.1 Flame Properties**

Figs. 4-12 and 4-13 present the character of the local emission properties of intensity and temperature at  $x/D = 0.8$ . The probability density function (PDF) of intensity for three radial locations is presented in Fig. 4-12. In the region near the pool center ( $r/D = 0.0$  to  $r/D = 0.14$ ), the PDFs of intensity are approximately log-normal. The large dynamic range of intensities is made clear by the long tail of the PDF curves. The abundance of low intensity points at  $r/D = 0.28$  is due to flame intermittency at this position. Fig. 4-13 presents the PDF of emission temperatures. The detectable emission temperatures occur within the range of 1000 to 1700 K. The large spike at 300 K, especially at  $r/D = 0.28$ , is indicative of the large amount of low emission intensity realizations at this axial position.

##### **4.3.2.2 Turbulence Radiation Interactions**

Predictions and measurements of mean and RMS intensity ( $\lambda = 1.0 \mu\text{m}$ ) for increasing radiation path length are shown in Fig. 4-14. The measured intensity increases rapidly with increasing path length due to the increased amount of radiating material in the probe volume. At the longer path lengths, the intensity levels off due to the effects of self absorption and intermittency.

In order to test the importance of the different nonlinear processes, predictions of monochromatic intensity for various path lengths were made utilizing: (1) the instantaneous measurements of local temperature and soot volume fraction and (2) the instantaneous measurements of local intensity and soot volume fraction. The results are shown in Fig. 4-14. The results indicate that the local emission measurements resolved the turbulence scales necessary for radiation predictions and that the lack of information regarding spatial correlations can be overcome with the appropriate choice of radiation segment length.

Fig. 4-15 presents predictions of intensity which utilized the filtered instantaneous intensity and emission soot volume fraction measurements. The elimination of fluctuations had little effect on the mean intensity levels along the path. As turbulence-radiation interactions are inherent within the intensity measurements themselves, the removal of the high frequency fluctuations would have the greatest effect on the non-linear transmittance term. Since

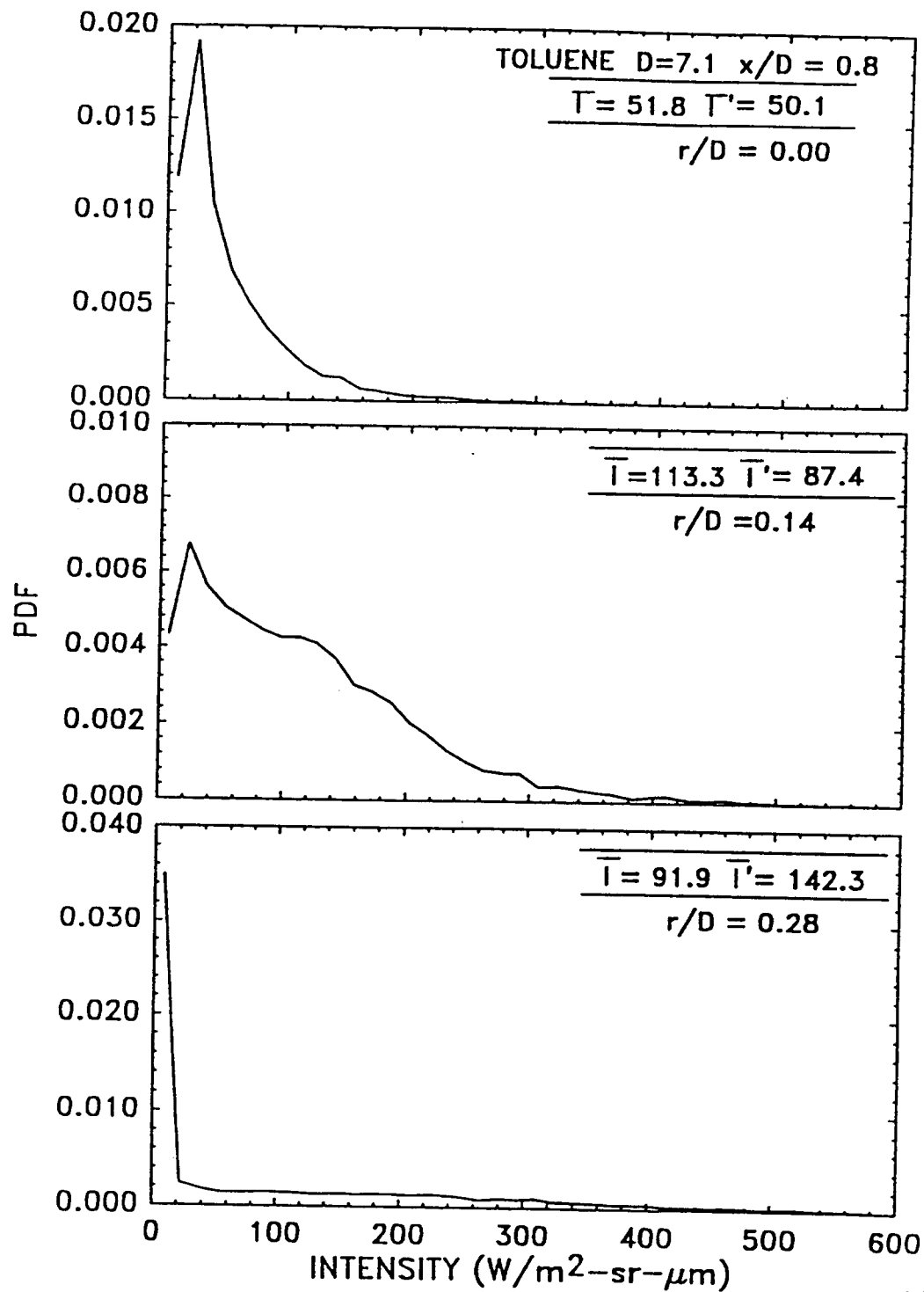


Fig. 4-12 PDFs of emission intensity as a function of radial position at  $x/D = 0.8$

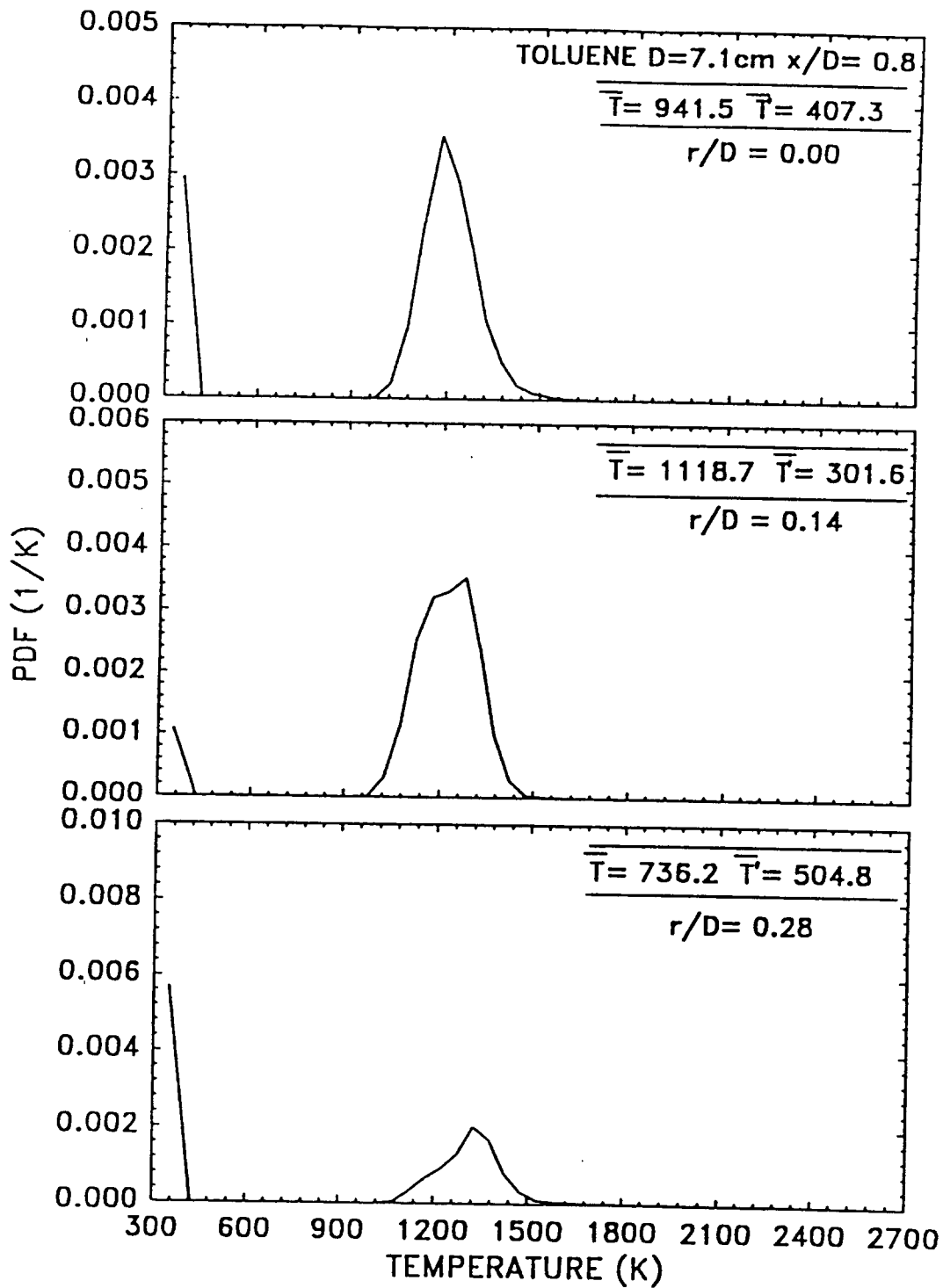


Fig. 4-13 PDFs of emission temperature as a function of radial position at  $x/D = 0.8$

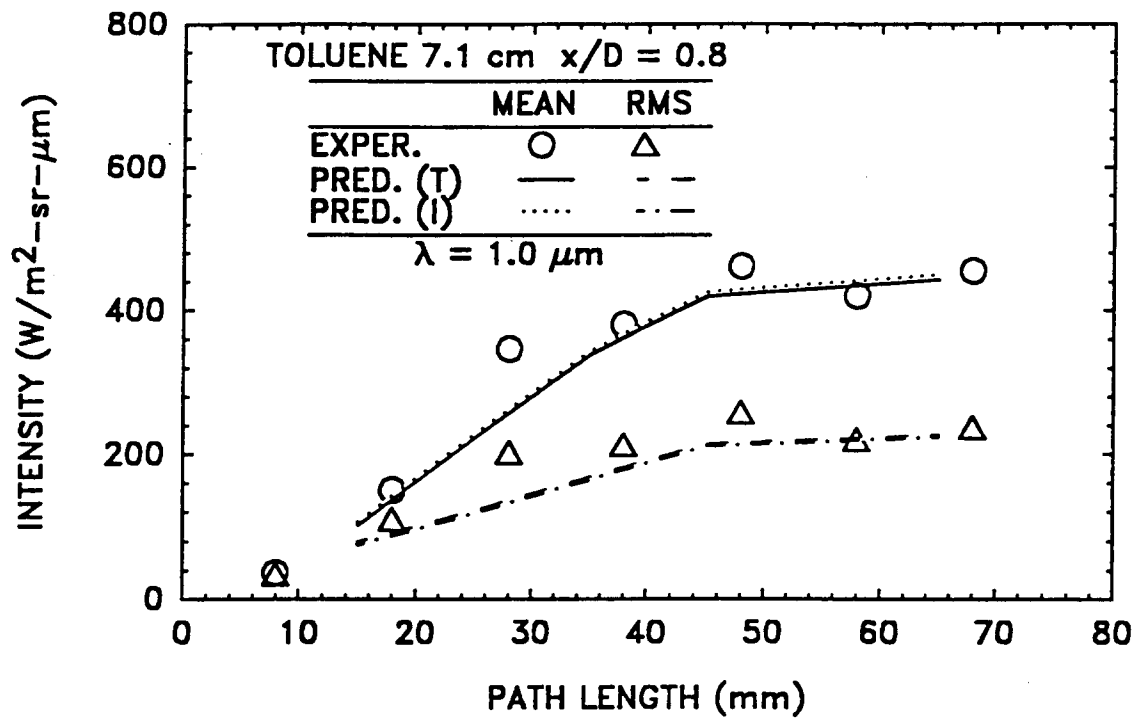


Fig. 4-14 Predictions and measurements of monochromatic intensity ( $\lambda = 1.0 \mu\text{m}$ ) at  $x/D = 0.8$

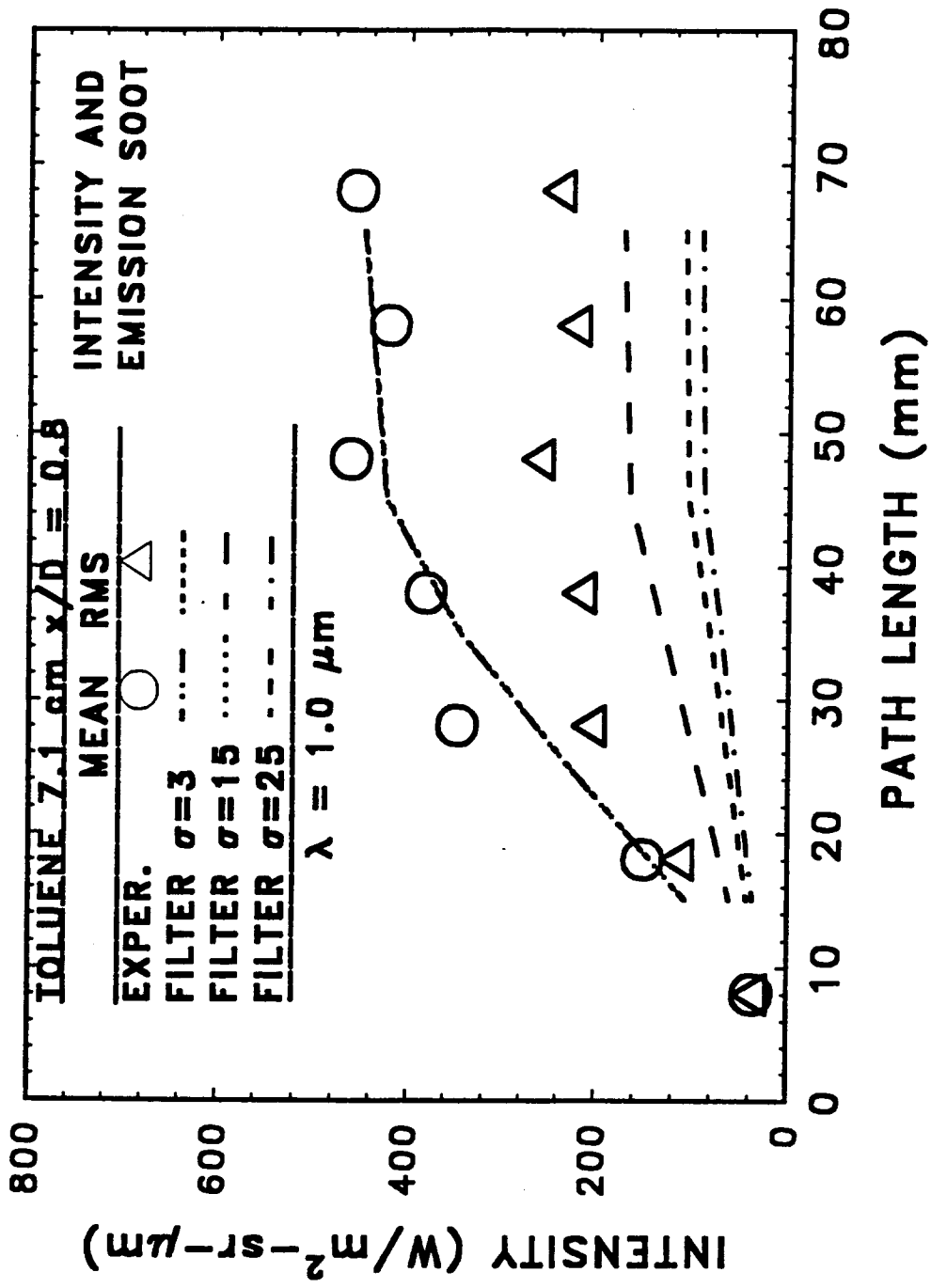


Fig. 4-15 Predictions of monochromatic intensity ( $\lambda = 1.0 \text{ } \mu\text{m}$ ) using filtered emission intensity and soot volume fraction

even heavy dampening of the fluctuations had no effect on the mean intensity predictions, the non-linearity of the transmittance was not significant in radiative transfer. The predictions of intensity RMS are affected much more by the removal of the high frequency fluctuations. Examination of Eqn. 4-10 indicates that fluctuations should play a more direct role in the calculation of the RMS of intensity, and that is seen by the underprediction of this quantity, even when predictions of mean intensity are quite good.

Fig. 4-16 shows the predictions of intensity using filtered instantaneous temperatures and emission soot volume fractions. Small reductions in temperature fluctuations ( $\sigma=3$ ) led to significant underpredictions of both mean and RMS intensity. This effect on the mean intensity predictions is not seen in Fig. 4-16 and demonstrates the importance of the fluctuating quantities when using the nonlinear Planck's function for determining the emission intensity term ( $I_{\lambda e}$ ). When the fluctuations of the emission properties are severely reduced ( $\sigma=15$  and  $25$ ), the mean and RMS intensity levels drop quite dramatically. In fact, the predictions are quite similar to those made using mean temperature and emission soot properties.

Fig. 4-17 shows the effect of cutoff frequency on the intensity across a 15 mm path length. The mean and RMS intensity levels are not affected until approximately a cutoff frequency of 11 Hz, which corresponds to the frequency of large-scale motion in this flame.

#### 4.4 CONCLUSIONS

Use of an existing measurement technique in a liquid fired pool flame has resulted in considerable new information regarding the mean and RMS distributions of temperature and soot volume fractions. These distributions suggest new features of strongly radiating flame structure that must be considered in the analysis of heat transfer and pollutant emission from flames. Predictions of monochromatic emission intensity using local emission properties were made. Two distinct procedures were used in the treatment of emission intensity. The first used local transient emission intensity data while the second used local transient temperatures. For the unfiltered signals, the results of the two methods are identical. However, effects of filtering on the method involving temperatures are strong. The specific conclusions that can be drawn from the present study are as follows:

(1) Considerable fluctuations in local emission intensities and transmittance measurements based on absorption exist in all regions of the present pool flames.

(2) A layer of cold soot particles with large volume fractions exists near the liquid surface in the present toluene fired pool flame. Based on visual observations these particles are probably transported to the cold central region

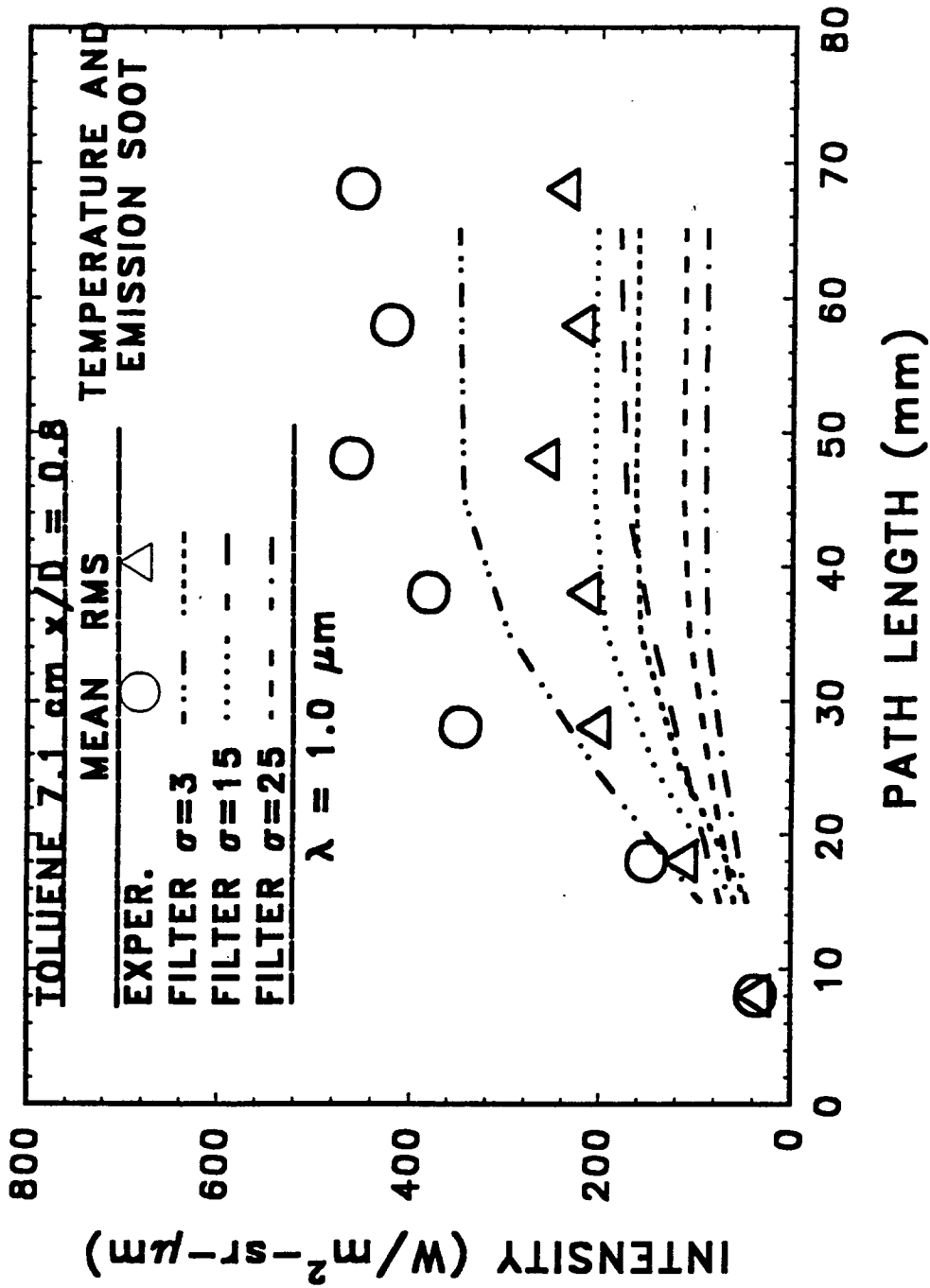


Fig. 4-16 Predictions of monochromatic intensity ( $\lambda = 1.0 \mu\text{m}$ ) using filtered emission temperature and soot volume fraction

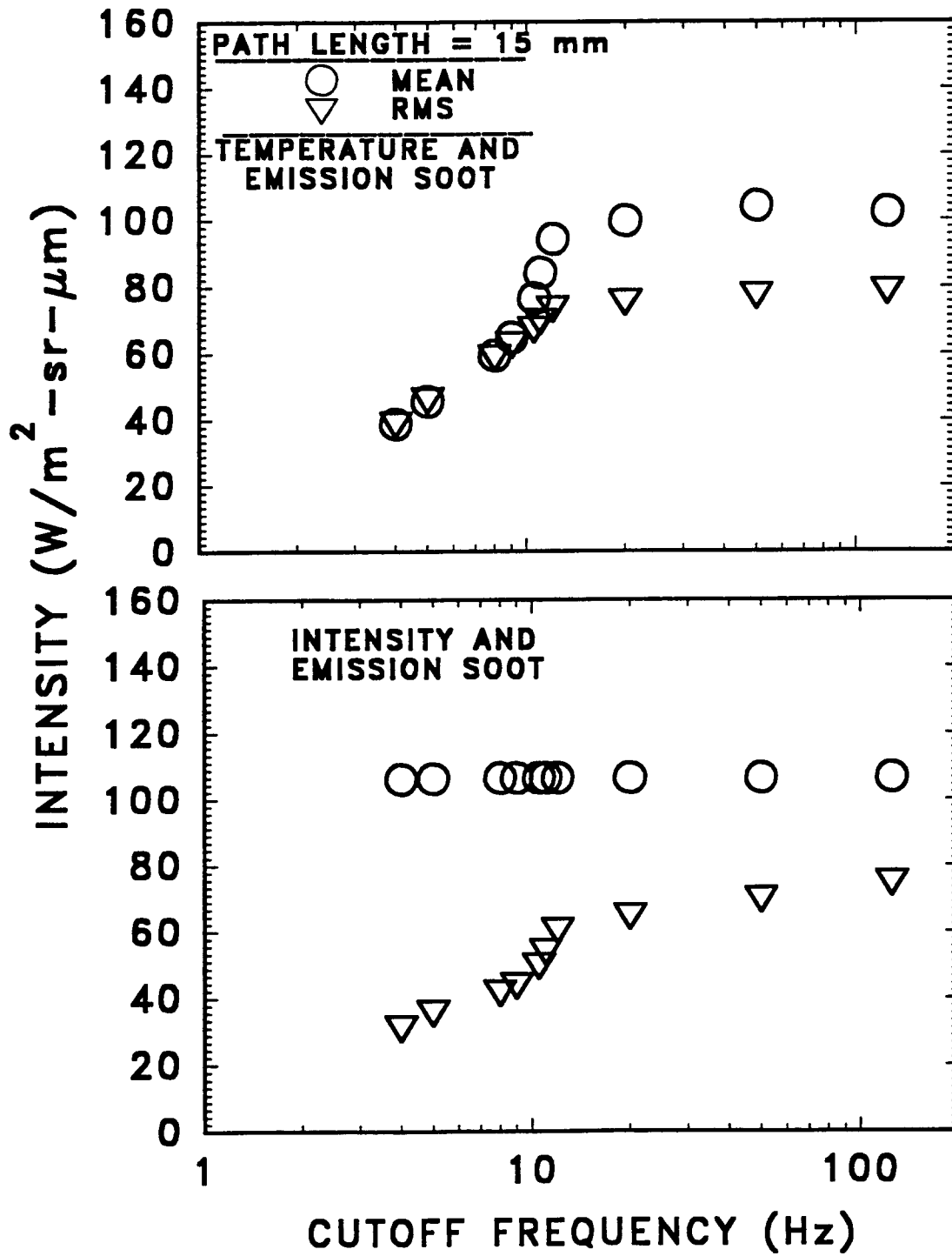


Fig. 4-17 Effect of cutoff frequency on predictions of monochromatic intensity ( $\lambda = 1.0 \mu\text{m}$ )

near the liquid surface by convective velocities and thermophoresis.

(3) The measurements of emission and absorption based soot volume fractions in all regions of the flame suggest that a considerable portion of the soot particles seen by the laser absorption probe are relatively cold and do not contribute to emission. The existence of such particles implies a flame structure resulting from a balance between radiative heat loss and convection and diffusion of energy to regions of high soot concentrations.

(4) Lack of spatial correlations information can be overcome with the selection of appropriate radiation length scales.

(5) Turbulence-radiation interactions analysis has provided insight into the important physical processes in the equation of transfer. A filtering technique involving Gaussian distributions along with experimental measurements of emission properties was used to verify this analysis. Little effect was seen on the mean and RMS intensity levels until all frequencies above that of large scale motion for the flame were removed. The fluctuations of local emission temperature proved to have the most significant effect on the monochromatic radiation intensity leaving the flame.

The present measurements indicate that the result of such a balance is a relatively low soot layer temperature for the heavily sooting toluene flames. The resulting flame structure is substantially different from that of weakly radiating flames.

## CHAPTER V PREDICTIONS OF RADIATIVE FEEDBACK

### 5.1 Introduction

Studies of radiative heat feedback to the fuel surface in liquid pool flames are motivated by the dominant role played by this mechanism in the determination of burning rates (Burgess and Hertzberg, 1974). This portion of the investigation details the local emission/absorption measurements in the 30 cm toluene and heptane pool flames. The local scalar measurements were used in predictions of radiative heat feedback to the fuel surface which will be compared with the measurements of this quantity detailed in Chapter 3. Many practical fires are heavily sooty and measurements of radiative heat feedback under such conditions are important.

Early methods of calculating radiative feedback utilized an average flame emissivity, an average shape factor and a constant temperature for the entire fire (Burgess and Hertzberg, 1974). Multi-ray methods based on the use of measurements of local mean absorption coefficients and mean temperatures were introduced by Modak (1977). Orloff (1981) used Markstein's (1981) scanning radiometer data to obtain effective mean temperatures and absorption coefficients as a function of height above the pool surface. Variations in radiation intensity from different radial positions were assumed to originate from different view angles and flame shapes. The mean flame shapes were obtained by averaging instantaneous photographs similar to the work of Modak (1977).

Based on measurements of mean and higher moments of emission intensity and absorption coefficient for arbitrary paths in the pool fires, Markstein (1981) suggested that information regarding turbulent fluctuations was necessary for obtaining improved models of radiative heat transfer.

Turbulent fluctuations in temperature and soot concentrations are known to cause mean radiative heat fluxes to the surroundings to be much larger than estimates based on average values (Grosshandler and Joulain, 1986, Gore and Faeth, 1986, Sivathanu et al. 1990, Sivathanu 1990). Past methods of accounting for turbulent fluctuations have relied on stochastic simulations. Some of these studies have used a calibrated turbulence model in conjunction with state relationships for soot concentrations (Gore and Faeth, 1986), while others (Sivathanu et al., 1990, Sivathanu, 1990) have avoided these uncertainties by using in-situ absorption and emission measurements.

Sivathanu et al. (1990) and Sivathanu (1990) used two-point absorption measurements in conjunction with a soot volume fraction-temperature correlation to calculate radiation intensity from gas-fired pool flames. The temperature was selected between overfire- and underfire- levels based on a

threshold for emission intensity at one wavelength. The results were very sensitive to the selection of the underfire temperature. The discrepancies between measurements and estimates obtained using low underfire temperatures were between 15 and 100%.

Recently, Sivathanu et al. (1991) have found that a large portion of the soot particles measured by absorption probes are at relatively low temperatures and do not contribute significantly to the emission of radiation. Therefore, a measure of volume fraction of the hot emitting soot particles was obtained by utilizing the emission data. A highly negative cross-correlation between temperatures and soot volume fractions based on emission was observed. A bivariate stochastic simulation was successfully applied to the prediction of spectral radiation intensity using measured temperatures (Sivathanu, 1991).

The stochastic methods of treating turbulence-radiation interactions are computer intensive. Therefore, these have been applied only to the calculation of directional monochromatic radiation intensities leaving the flames along few specific directions (Gore and Faeth, 1986, Sivathanu et al., 1990, Sivathanu, 1990, Sivathanu et al., 1991). However, for engineering applications, estimates of total hemispherical intensity and resulting heat flux at points of interest are needed.

Based on this background, the specific objectives of this part of the investigation are: (1) to complete local measurements of soot volume fractions based on emission (representing hot soot particles) and absorption (representing all soot particles) and temperatures based on emission in 30 cm toluene flames; (2) to use new treatment of the equation of radiative transfer described in Chapter 4 to account for the effects of turbulent fluctuations on the total hemispherical heat feedback to the fuel surface; and (3) compare the predicted directional and total hemispherical radiative feedback with the measurements detailed in Chapter 3.

## **5.2 Experimental Methods**

### **5.2.1 Experimental Apparatus**

The details of the pool burners and fuel supply system are described in Chapter 2. All measurements were made in the 30 cm diameter burner. A constant fuel level of 5 mm below the lip of the burner was maintained.

### **5.2.2 Instrumentation**

The emission-absorption probe has been described in detail in section 4.2.2. The two 6 mm diameter purged tubes aligned with 20 mm distance between them defined the measurement volume and served as cold background for each other. The left side tube collected the emission signal from the fire. A beam splitter sent the emission signal to photomultipliers equipped with filters with central wavelengths of 900 nm and 1000 nm and half-bandwidth of  $\pm 50$  nm. A second beam splitter guided a laser beam through the

measuring volume. The transmitted beam was collected by the right hand side purged tube and sent to a laser power meter.

The signals collected by the calibrated PMTs and the laser power meter were amplified and processed through antialiasing filters before collection by a laboratory computer. The signals were sampled at 250 Hz by the computer after being filtered at 125 Hz.

Incident directional radiative heat feedback was measured 2 mm above the fuel surface using a nitrogen-purged, water radiometer. The radiometer and the measurement technique are detailed in section 3.2.1.

### 5.2.3 Data Analysis

The methods used to obtain emission temperature, emission soot volume fraction and absorption soot volume fraction are detailed in section 4.3. If emission intensities were below the detection limit of the instrumentation, the emission temperature was arbitrarily assigned a value of 300 K and the emission soot volume fraction was assigned a value of 0 ppm. The technique used to obtain hemispherical radiative heat feedback based on directional intensity measurements is described in section 3.3.

### 5.2.4 Radiation Predictions

The radiative heat feedback is obtained by integrating directional spectral radiation intensities over the relevant wavelength interval and over the hemisphere. As shown in Fig. 5-1, an imaginary hemisphere on the aperture of the purged radiometer is divided into several segments by individual rays. Radiation intensity along these rays is calculated analogous to the measurements obtained by the narrow angle radiometer described in the previous section.

The calculations involved integration of the equation of transfer using discrete radiation segments 1 to N as shown in Fig. 5-1 for a representative path. The radiation intensity is dominated by soot particles in the present fires. Therefore, the mean local spectral intensity emitted by a segment "M" along a radiation path is obtained as:

$$\overline{I_{\lambda_e}(M)} = (1 - \overline{\tau_{\lambda_e}(M)}) \overline{I_{\lambda_b}(M)} \quad (5-1)$$

where  $\overline{I_{\lambda_b}(M)}$  is the instantaneous Planck's function defined in Eqn. (4-4) and  $(1 - \overline{\tau_{\lambda_e}(M)})$  is the instantaneous emissivity based on the transmittance defined by Eqn. (4-5). The overbar indicates that average of the product of the Planck's function and the emissivity is obtained in order to treat the effects of turbulent fluctuations on these non-linear functions of T and  $f_{ve}$ . The basis for the present calculations is that T(M) and  $f_{ve}(M)$  are independent of the measurement wavelengths as verified by Sivathanu et al.<sup>12</sup> by making measurements at several different wavelengths. The  $K_1$  for all wavelengths between 0.5 and 10  $\mu\text{m}$  are obtained from Dalzell and Sarofim (1969). The fraction of the energy emitted by the segment "M"

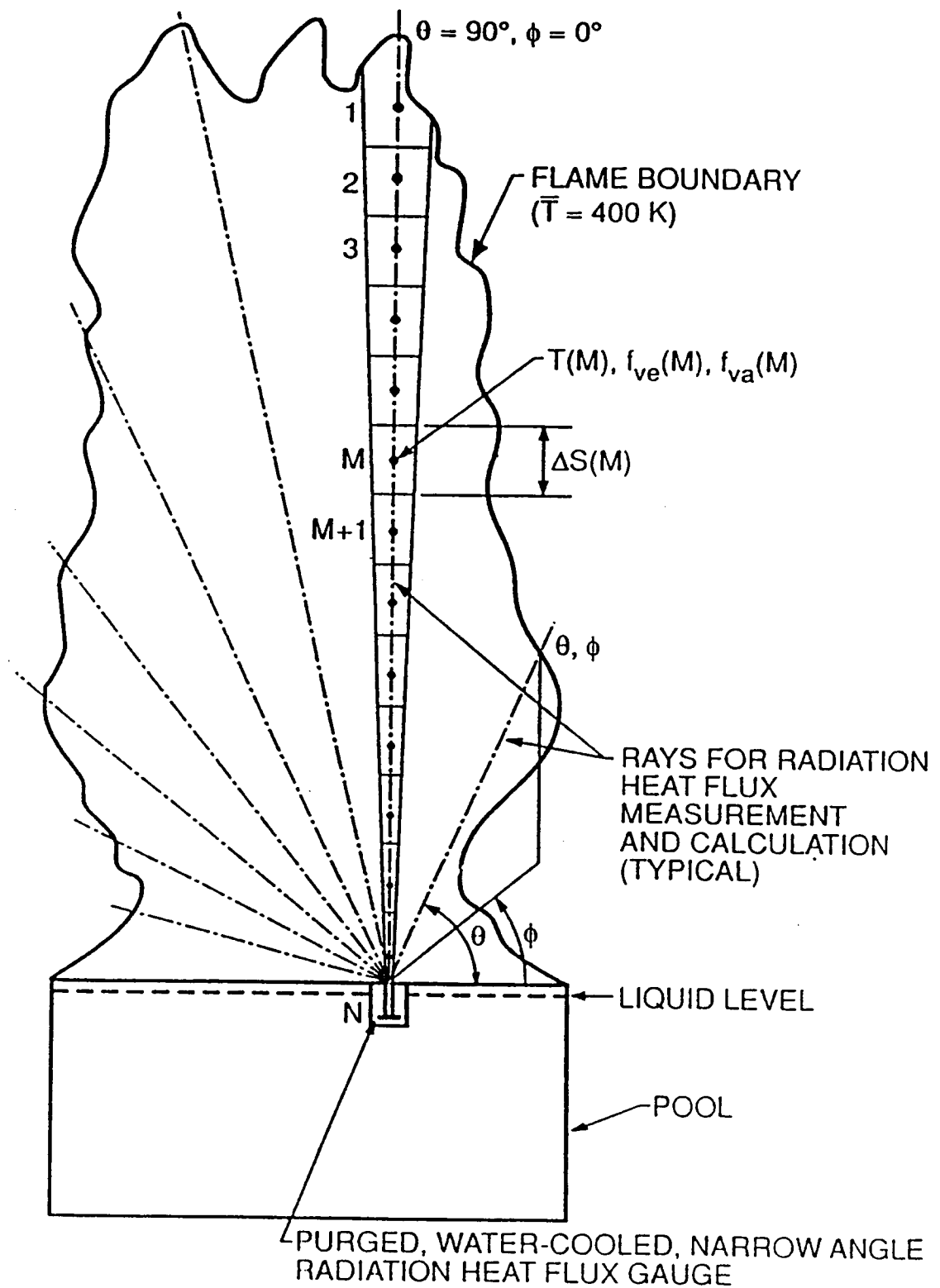


Fig. 5-1 Sketch of the rays and flame segments used in the calculations of radiative heat feedback

that is incident on the fuel surface (location "N") can be calculated as:

$$I_{\lambda M}(N) - I_{\lambda e}(M) \prod_{J=M+1}^N \tau_{\lambda a}(J) \quad (5-2)$$

In order to treat the effects of turbulence on the radiative heat flux reaching the location "N" accurately, simultaneous estimates of emissive power at the segment "M" and absorption transmittances at all intervening segments "M+1" to "N" would be required. For the purpose of calculating average heat flux, estimates of length scales and two-point correlation coefficients between  $I_{\lambda e}(M)$  and  $(\tau_{\lambda a}(J), J=M+1, N)$  are sufficient. However, measurements of these quantities are unavailable. It was found earlier that the effects of length scales and cross correlations can be treated effectively by replacing  $\tau_{\lambda a}(J)$  by  $\tau_{\lambda e}(J)$  and then equating the mean intensity to the product of the averages of the terms on RHS in Eqn. (5-2) (Sivathanu, 1991). As seen from the results, this approximation was found to be applicable in the present flames indicating that the flame dynamics lead to simultaneous occurrence of high  $I_{\lambda e}(M)$  and high  $(\tau_{\lambda e}(J), J=M+1, N)$ . The directional spectral radiation heat flux for a ray can be obtained as:

$$I_{\lambda}(N) - \sum_{M=1}^{M-N} I_{\lambda M}(N) \quad (5-3)$$

Using these for all rays, the total hemispherical radiative heat flux reaching the fuel surface at location "N" is calculated as (Siegal and Howell, 1981):

$$q(N) - \int_{\theta=0}^{\pi/2} \int_{\phi=0}^{\pi} \left( \int_{\lambda=0}^{\infty} I_{\lambda}(N) d\lambda \right) \sin\theta \cos\theta d\phi d\theta \quad (5-4)$$

The spectral intensities were integrated over 40 segments in the wavelength interval 0.5 to 10  $\mu\text{m}$ . The resulting directional total intensities were integrated over discrete rays. The number of rays were varied between 2 and 450 and it was found that the total heat flux changes by less than 15% between 22 and 450 rays. It is noted that the measurements obtained by the gauge correspond to the integral over wavelength in Eqn. (5-4). The integration over the hemisphere is applied to both calculated and measured intensities to obtain the radiative heat feedback. With the above formulation, the distributions of mean emissive power and emission transmittance are needed for calculating the heat feedback including the effects of turbulence.

### 5.2.5 Operating Conditions

The test conditions for local emission/absorption measurements of toluene and heptane in the 30 cm burner are included in Table 2-2. Radial measurements of local emission/absorption properties were made at 10 axial locations in the flame in the toluene flame and 8 axial positions in the heptane. The axial locations spanned the entire length of the

flame. Limited test times (less than 10 minutes) were used to control the effects of probe heatup to within 5% of the mean emission signal. Measurements along the radial direction crossed the entire half width of the flame at each axial location. The operating conditions for the radiative feedback measurements in toluene are described in section 3.4.

### 5.3 Results and Discussion

#### 5.3.1 Toluene

Fig. 5-2 shows the radial distributions of the measurements of mean and RMS temperatures for 5 axial positions. The lowest axial position ( $x/D = 0.1$ ) is in the conical region near the liquid surface. The flame structure at this station involves a relatively thin sheet near  $r/D = 0.55$  where the measured mean temperature reaches approximately 1000 K. The RMS temperature fluctuations in this region are 400 K probably caused by the flapping motion of the flame sheet. At all other radial locations ( $0 < r/D < 0.5$ ) at this station, the mean emission temperatures are very low as expected for the fuel rich locations near the liquid surface.

At positions farther away from the liquid surface, the measurements of mean emission temperatures (see measurements for  $x/D = 0.4$  shown in Fig. 5-2 for example) show that the structure involves the occasional arrival of high temperature material at all radial positions between  $r/D = 0$  and  $r/D = 0.25$ . The mean temperatures are between 1200 K and 1300 K in this region with the  $r/D = 0.2$  location showing the highest value. The RMS temperatures are near 400 K suggesting relatively high fluctuation intensities leading to significant effects on radiation heat flux.

Temperature distributions at three axial locations in the upper region of the fire are also shown in Fig. 5-2. This region is characterized by the highest mean temperature at the centerline which decreases due to mixing with ambient air as the axial position is increased and very high turbulence intensities with the RMS temperature fluctuations approaching 50% of the mean value. The last position shown in Fig. 5-2 ( $x/D = 4.3$ ) has a mean temperature of 450 K at the centerline.

Fig. 5-3 shows the measurements of emission soot volume fractions,  $f_{ve}$ , for the same axial positions as in Fig. 5-2. Recall that  $f_{ve}$  are a good measure of the hot soot particles. At the lowest station, the mean and RMS  $f_{ve}$  are negligible due to the low temperatures. Near the flame sheet, the mean  $f_{ve}$  increase to 2 PPM, and the RMS  $f_{ve}$  are over 100%. In the region beyond the conical zone near the surface, the  $f_{ve}$  increase to 9 PPM and are relatively constant at radial locations between  $r/D=0$  and  $r/D=0.15$ . As the region of highest mean temperatures is approached near the  $r/D = 0.2$  location, the  $f_{ve}$  to approximately 5 PPM. This is due to oxidation of the soot layer in the highest temperature region. Once again the RMS fluctuations in the measured  $f_{ve}$  are very high suggesting significant turbulence-radiation interactions. The

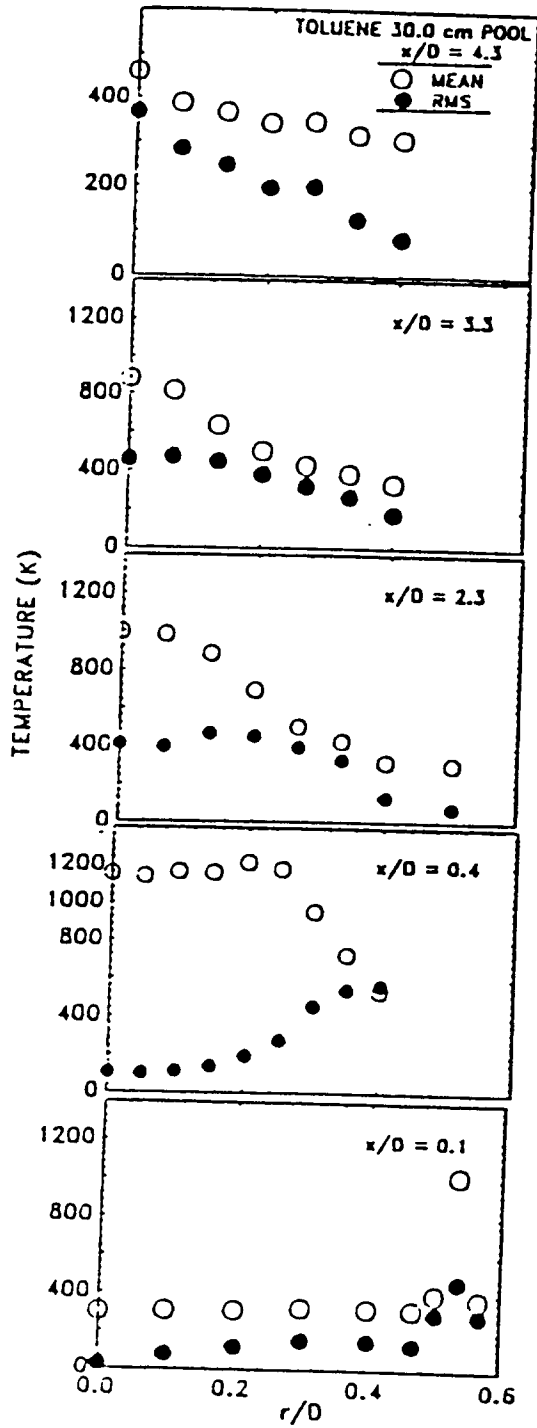


Fig. 5-2 Radial distributions of measurements of mean and RMS temperatures based on emission at two wavelengths in a 30 cm toluene pool fire

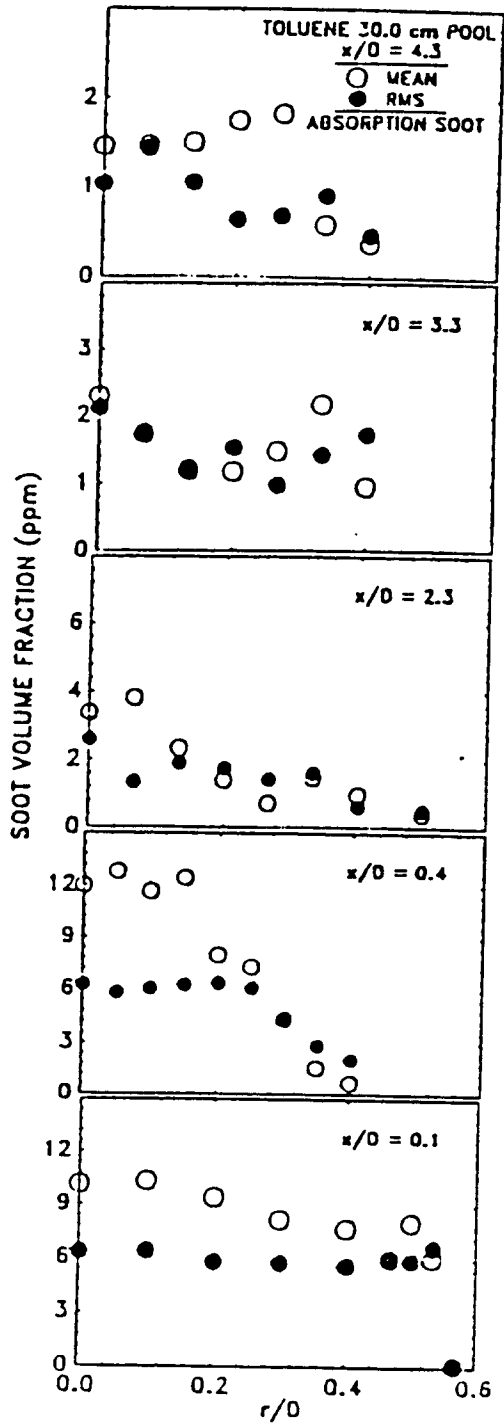


Fig. 5-3 Radial distributions of measurements of mean and RMS soot volume fractions based on absorption ( $\lambda = 0.632 \mu\text{m}$ ) in a 30 cm toluene pool fire

measurements in the upper region show that the  $f_{ve}$  decrease continuously as the temperature decreases. Finally, at the  $x/D=4.3$  location, the mean  $f_{ve}$  approach 0.2 PPM with over 400% RMS fluctuations.

Radial distributions of soot volume fractions based on absorption,  $f_{va}$ , are shown in Fig. 5-4 for the same 5 axial locations. At the lowest position the mean  $f_{va}$  reach their peak value (10 PPM) at the center and remain relatively high in the core region up to  $r/D=0.2$  and then slowly decrease near the flame sheet to approximately 6 PPM. Visual observations indicate that soot particles are carried to the central cold region near the fuel surface by the complex hydrodynamics of the entrainment and fire induced flow. The existence of cold soot particles near the liquid surface probably leads to substantial blockage of radiative heat feedback. It is noted that even at the location of highest mean temperature, the measurements of  $f_{va}$  are approximately 3 times those based on emission suggesting the presence of relatively cold soot near the flame sheet. The RMS  $f_{va}$  are very high even in the region near the fuel surface similar to the observations of Bouhafid et al. (1989).

The mean  $f_{va}$  are higher than  $f_{ve}$  at almost all the axial stations. At  $x/D=2.3$ , the mean  $f_{va}$  and  $f_{vp}$  are close suggesting local mean homogeneity of the material in the probe volume at this axial station. As this material cools by mixing with surrounding air and by radiative heat loss,  $f_{va}$  exceed  $f_{ve}$  substantially. Finally, the soot particles observed by the absorption probe at  $x/D=4.3$  represent the thick dark smoke that is visually observed in the region above the fire.

The measurements and calculations of directional total radiative heat flux are plotted as a function of radial position on the pool surface for three representative rays in Fig. 5-5. The ray marked  $\theta = 90^\circ$ ,  $\phi = 0^\circ$  is in the direction of gravity and shows the highest measured heat flux. The ray marked  $\theta = 110^\circ$ ,  $\phi = 0^\circ$  is directed at  $20^\circ$  to the direction of gravity and starts away from the fire axis. The ray marked  $\theta = 130^\circ$ ,  $\phi = 0^\circ$  is directed at  $40^\circ$  to the direction of gravity and starts away from the fire axis. Due to the shorter path length in the fire, this ray shows the lowest heat flux. The calculated directional heat fluxes are in reasonable agreement with the measurements considering the uncertainties in soot refractive indices, length scales and spatial cross correlations in soot concentrations and temperature. Discrepancies larger than the uncertainties occur for the ray in the direction of gravity at  $r/D=0.2$ . However, the overall performance of the radiation analysis is encouraging.

Fig. 5-6 shows measurements and predictions of total hemispherical radiation heat flux to the surface of the toluene pool obtained by integrating directional fluxes similar to those shown in Fig. 5-5. The data were obtained from the integration of 22 directional fluxes with appropriate weights. Calculations based on 22 to 450 rays were performed

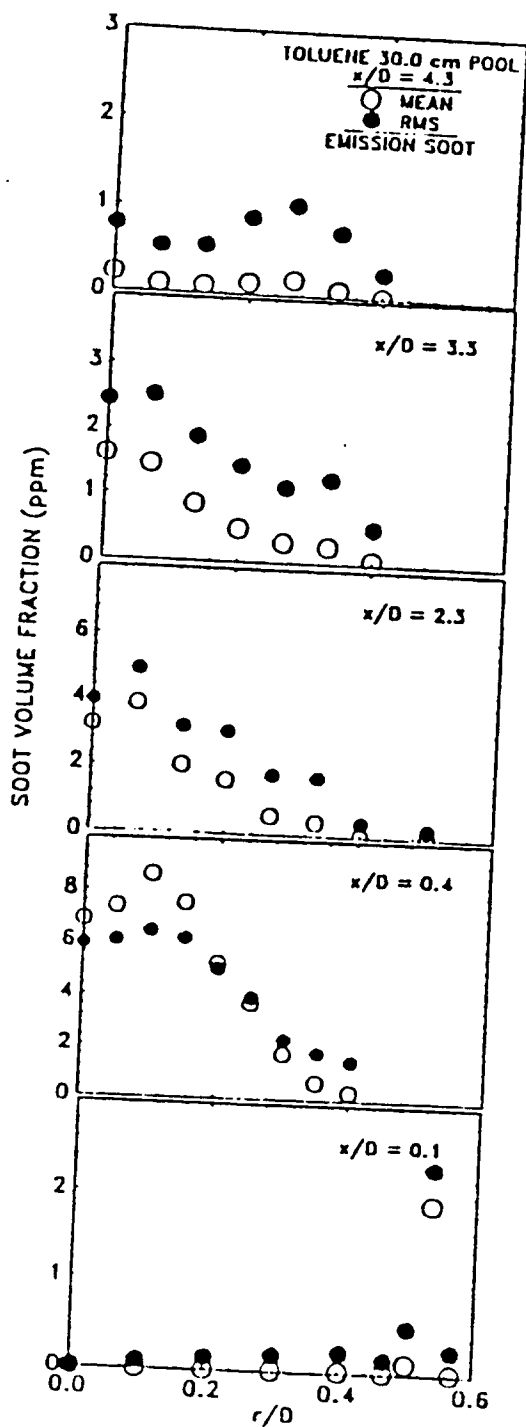


Fig. 5-4 Radial distributions of measurements of mean and RMS soot volume fractions based on emission at two wavelengths in a 30 cm toluene pool fire

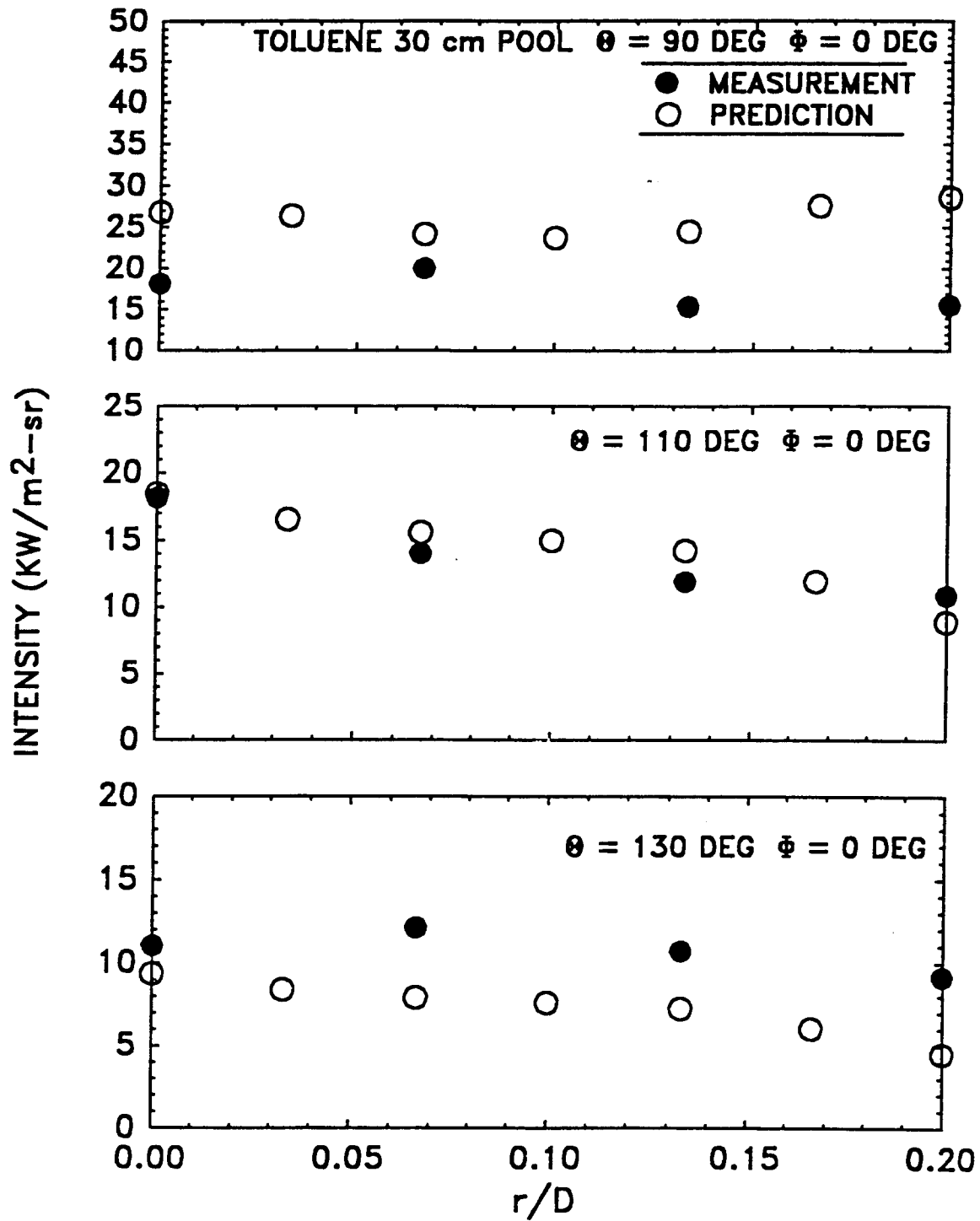


Fig. 5-5 Measurements and calculations of hemispherical radiative intensity incident the liquid surface as a function of radial location and view angle

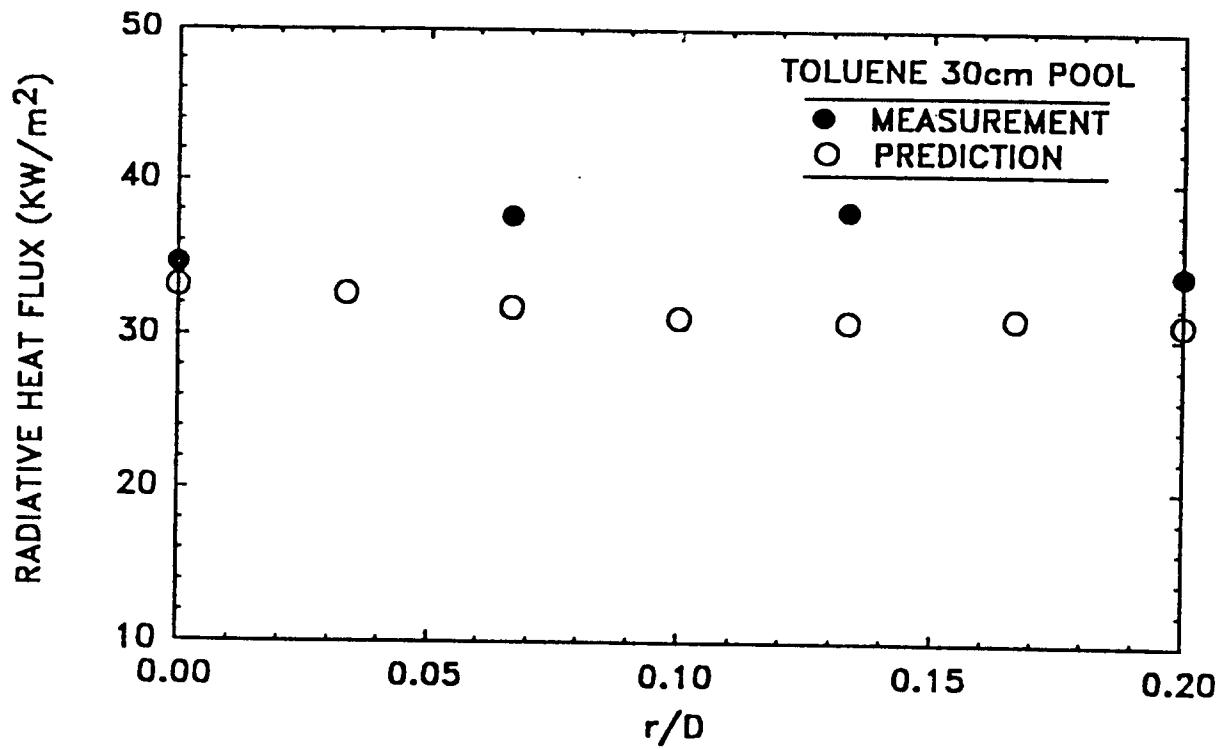


Fig. 5-6 Measurements and calculations of hemispherical radiative heat flux incident the surface of a 30cm toluene pool fire as a function of radial location

and showed 15% variation. The results reported in Fig. 5-6 are based on 450 rays. The agreement between measurements and calculations of heat feedback is good supporting the present method. Based on an energy balance at the liquid surface, the radiative heat flux of approximately  $30 \text{ kW/m}^2$  is sufficient to maintain the observed burning rate. Thus the fire is dominated completely by radiative heat feedback.

### 5.3.2 Heptane

Measurements of the absorption/emission properties in heptane show a different flame structure than that seen in toluene. Temperatures in the lower region of the flame ( $x/D = 0.2$ ) as seen in Fig. 5-7 show that mean temperatures are much higher than seen in the toluene flame at a similar axial position. Even at higher axial locations (e.g.  $x/D = 2.3$ ) the mean temperatures are generally greater than found in the toluene flame.

Fig. 5-8 presents the radial distribution of emission soot volume fractions at three different axial locations. As seen in the previous flames, the RMS values of this quantity are quite large, sometimes double that of the mean soot volume fraction. The largest amount of emission soot occurs at a much higher location in the heptane flame ( $x/D = 1.5$ ) as compared to the toluene flame ( $x/D = 0.4$ ).

Fig. 5-9 shows measurements and predictions of total hemispherical radiation heat flux to the surface of the toluene pool obtained by integrating directional fluxes. The calculations are based only on soot emission and neglect the contribution of gas band radiation, which should be considerable in the heptane flame. Calculations of radiative heat flux to region near the burner edge ( $r/D > 0.2$ ) were quite low due to the coarseness of the grid of emission/absorption measurements, especially near the fuel surface.

Fig. 5-10 shows the contribution of radiant heat flux to the pool center from various axial distances from the fuel surface based on predictions. The results indicate that only radiation from the region near the fuel surface ( $x/D < 1.0$ ) contributed to the feedback. Radiation from regions above  $x/D = 1.0$  does not reach the fuel surface due to absorption. The contribution of radiation heat flux from different axial locations in heptane is also predicted. Measurements of the emission and absorption properties were made in the manner as described in Section 5-3. The predictions of heptane feedback are only based on soot emission, though gas emission is thought to be important. Contributions to the radiation incident on the fuel surface are seen from most axial heights in heptane though the largest contribution does originate from near the fuel surface. The self absorption seen in toluene is not as important in the heptane flame, due to lower amount of soot present.

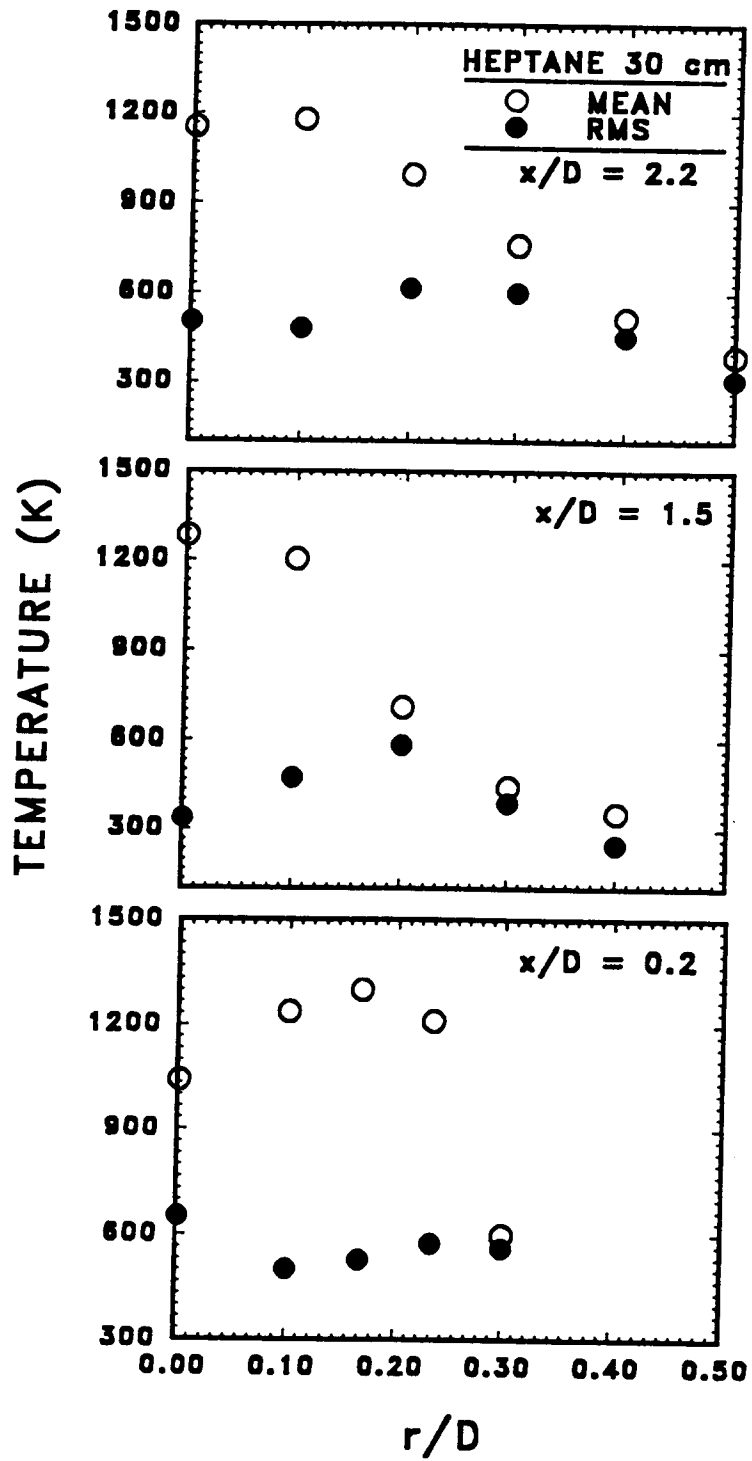


Fig. 5-7 Radial distributions of measurements of mean and RMS temperature based on emission at two wavelengths in a 30 cm heptane pool fire

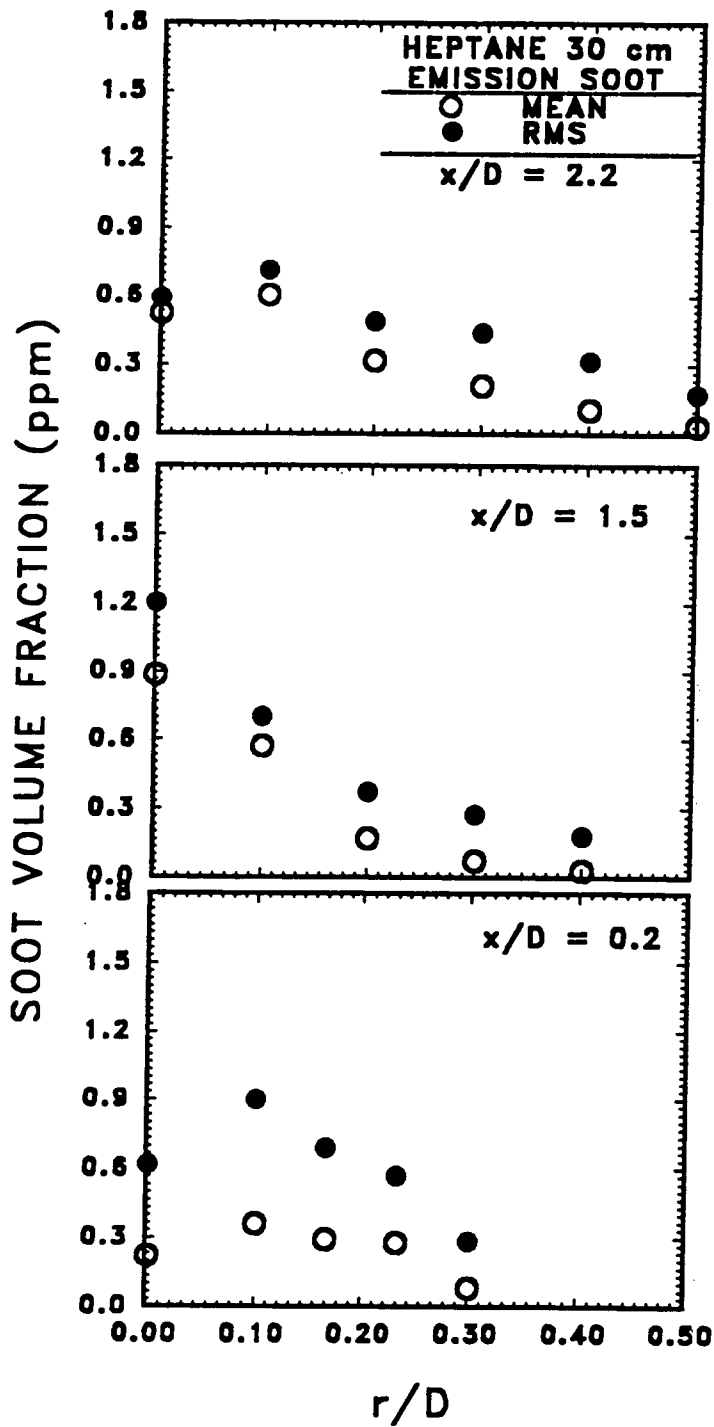


Fig. 5-8 Radial distributions of measurements of mean and RMS soot volume fractions based on emission at two wavelengths in a 30 cm heptane pool fire

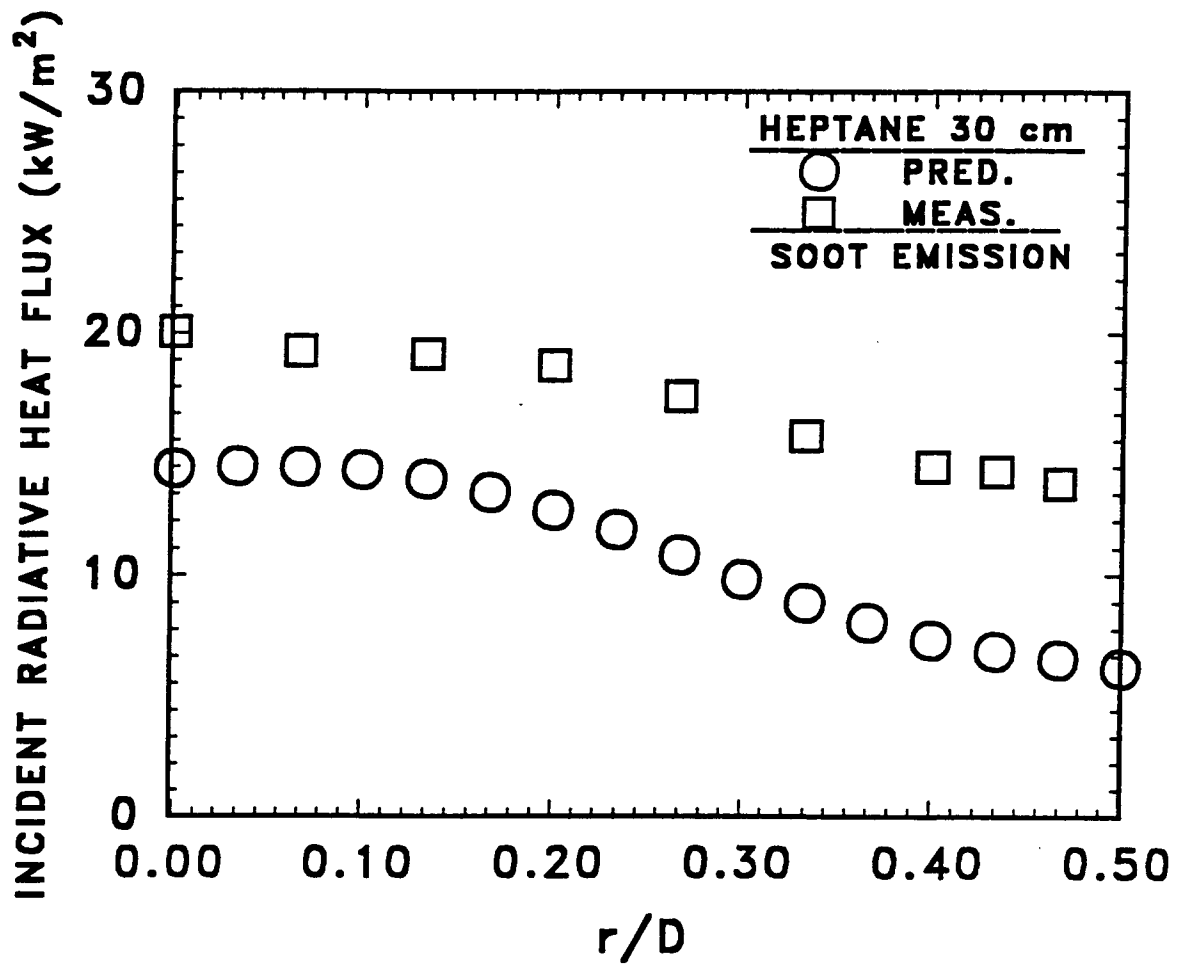


Fig. 5-9 Measurements and calculations of hemispherical radiative heat flux incident on the surface of a 30 cm heptane pool fire as a function of radial location

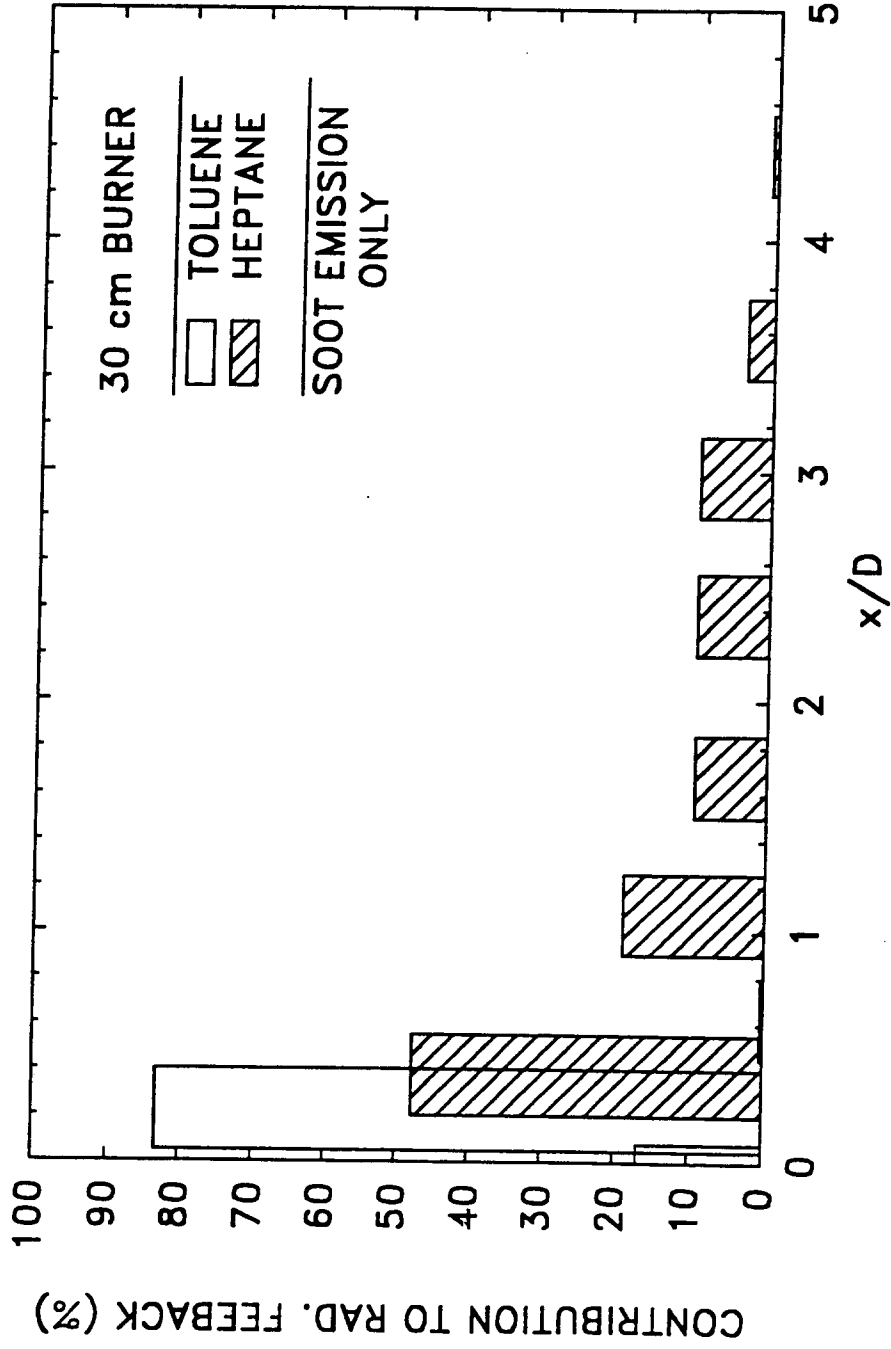


Fig. 5-10 Calculations of the contribution of radiative heat flux from different axial locations in 30cm toluene and heptane pool fires

#### 5.4 Conclusions

Detailed emission and absorption measurements as well as directional and hemispherical total heat feedback measurements in 30 cm toluene fires have shown that:

(1) Large fluctuation intensities in temperatures and soot volume fractions based on absorption and emission exist in all regions of the fire. This is similar to the structure seen in the toluene flame for the 7.1 cm burner (Chapter 4) and that observed in earlier studies (Bouhafid et al., 1989; Fischer et al., 1987).

(2) A transient layer of cold soot particles exists near the liquid surface. The role of this layer in blocking the radiative heat feedback can be treated within the present radiation analysis.

(3) A significant fraction of soot particles at most locations in the flames are at relatively low temperatures and do not contribute to the radiative feedback.

(4) The radiation analysis based on transient measurements of temperature and soot volume fractions can be applied successfully in conjunction with a simplified treatment of turbulence radiation interactions to estimate directional total and hemispherical total heat feedback to the fuel surface. However, predictive models for obtaining the necessary transient distributions are sparse.

## **CHAPTER VI SUMMARY AND CONCLUSIONS**

### **6.1 Summary**

The overall objective of the present study was to improve the understanding of radiation from liquid fueled pool flames. Particular emphasis was placed on investigating the mechanism of radiative heat feedback in pool flames. The effect of fuel type and scale on burning rates and flame radiation was studied for a variety of alcohol, paraffin, and aromatic fuels. A multi-location method was used to measure total radiative output from these flames. Measurements were made of the radiative energy incident on the fuel surface. Local emission and absorption properties were determined for all regions of luminous pool fires. Predications of directional and hemispherical radiative heat feedback were made using the local emission/absorption properties. The effects of turbulence-radiation interactions on radiation predictions of radiative heat feedback and monochromatic intensity were investigated.

### **6.2 Conclusions**

In addition to the conclusions presented at the end of each section, the significant observations and contributions of the present study are as follows:

1. The total radiative heat loss fractions for a particular fuel were found to be constant for the scales investigated. Families of fuels were also found to have comparable radiative heat loss fractions.

2. Measurements of radiative heat feedback showed that radiation is a significant heat transfer mechanism in sooting flames but also in non-luminous flames. Radiation contributed almost the entire heat transfer to the fuel surface in toluene and heptane flames. Radiative heat feedback was significant in the center of methanol flames.

3. The emission/absorption properties of pool flames were found to have a large dynamic range. Significant fluctuations of scalars were found in all regions of the flames. Large amounts of non-emitting soot were found in all regions of a strongly radiating pool flame. This finding explains the similarity in radiative loss fractions for fuels of different sooting tendencies.

4. The importance of turbulence-radiation interactions in radiative heat transfer was shown. Fluctuations in scalar properties were shown to be important for predictions of radiative heat feedback and monochromatic intensities.

### **6.3 Recommendations for Further Research**

The present study concentrated on the local emission properties of soot dominated, strongly radiating flames. In optically thin flames, radiation from combustion gases must be considered. Simultaneous measurements of radiating gas concentrations in pool flames must be made. Planar measurements of emission properties, as opposed to the single point measurements made in this study, would give additional information about turbulence-radiation interactions in pool flames.

APPENDICES

## APPENDIX A

### FUEL PROPERTIES

FUEL	H <sub>v</sub> Heat of vaporization (kJ/kg)	H <sub>c</sub> Heat of combustion (kJ/kg)	C <sub>p</sub> Specific Heat (kJ/kg-K)	T <sub>boil</sub> Boiling Temperature (K)
Methanol	1088	22317	2.67	338
Ethanol	876	27972	2.71	351
Hexanol	494	38600	2.40	361
Heptane	316	48181	2.26	372
MMA	311	27699	2.0	373
Toluene	365	41079	1.73	384
Styrene	340	41314	1.59	418
30% Toluene + 70% Ethanol	712	32146	2.40	361

\* Values obtained from Daubert and Danner, (1984)

**APPENDIX B**

**TOTAL RADIATIVE OUTPUT**

HEPTANE 7.1 cm TOTAL RADIATIVE OUTPUT CALIBRATION CONST = 0.208 W/cm<sup>2</sup>-mv  
 hep2vert.dat hep2rad.dat  
 axial radial

SIGNAL (v)	POS (cm)	SIGNAL (v)	POS (cm)
.69580E-01	00	.36820E+00	00
.73890E-01	2.54	.36820E+00	6.35
.75290E-01	5.08	.27100E+00	8.89
.76820E-01	7.62	.20090E+00	11.43
.79360E-01	10.16	.16200E+00	13.97
.82290E-01	15.24	.14600E+00	16.51
.79000E-01	17.78	.11050E+00	19.05
.80230E-01	20.32	.90590E-01	21.59
.80430E-01	22.86	.79230E-01	24.13
.80620E-01	25.40	.67600E-01	26.67
.74660E-01	27.94	.57470E-01	29.21
.69750E-01	30.48	.46230E-01	31.75
.65350E-01	33.02	.34980E-01	34.29
.65190E-01	35.56		
.59980E-01	38.10		
.54900E-01	40.64		
.50600E-01	43.18		
.47360E-01	45.72		
.41070E-01	48.26		
.38130E-01	50.80		
.34320E-01	53.34		
.31040E-01	55.88		
.28130E-01	58.42		
.25560E-01	60.96		
.23330E-01	63.50		
.20250E-01	66.04		
.19090E-01	68.58		
.17340E-01	71.12		
.15920E-01	73.66		
.13650E-01	76.20		
.13090E-01	78.74		
.12120E-01	81.28		

SIDE FLUX= 249.0908W BOTTOM FLUX=189.1772W

TOTAL FLUX= 4.382681E-01 kW  
 HEPTANE 30 CM TOTAL RADIATIVE OUTPUT

HAX12.DAT

HRA12.DAT

HEPTANE 100 cm TOTAL RADIATIVE OUTPUT

hep#6xrc.dat  
AXIAL

hep#6xrr.dat  
RADIAL

Q, W/cm2	POS (cm)	Q, W/cm2	POS (cm)
0.36700E+00	0.00	0.33340E+01	0.00
0.42638E+00	50.00	0.33340E+01	60.00
0.44623E+00	100.00	0.15395E+01	122.00
0.46634E+00	150.00	0.31405E+00	250.00
0.42952E+00	222.00	0.62672E-01	285.00
0.36206E+00	290.00	0.50996E-01	345.00
0.28639E+00	350.00	0.16600E-01	442.00
0.19455E+00	400.00		
0.00000E+00	555.00		

SIDE FLUX= 470250 W      BOTTOM FLUX= 164269.0W

TOTAL FLUX= 634.519kW



HEXANOL 7.1 cm TOTAL RADIATIVE OUTPUT CALIB. CONST = .208 W/cm2-mv

HEXALCVT.RAD  
AXIAL

HEXALC1B.RAD  
RADIAL

SIGNAL (v)	POS (cm)	SIGNAL (v)	POS (cm)
.35450E-01	.00	.28490E+00	.00
.35340E-01	2.54	.28490E+00	6.35
.38220E-01	5.08	.18860E+00	8.89
.37120E-01	7.62	.12430E+00	11.43
.38080E-01	10.16	.87020E-01	13.97
.36570E-01	12.70	.67150E-01	16.51
.36110E-01	15.24	.49440E-01	19.05
.37820E-01	17.78	.36000E-01	21.59
.36920E-01	20.32	.29190E-01	24.13
.32100E-01	22.86	.22880E-01	26.67
.29810E-01	27.94	.19380E-01	29.21
.26800E-01	33.02	.15690E-01	31.75
.20470E-01	38.10	.11410E-01	36.82
.15620E-01	43.18	.50850E-02	41.91
.91480E-02	53.34		
.45620E-02	63.50		
.00000E+00	73.61		

SIDE FLUX= 214.788800W BOTTOM FLUX= 84.783150W

TOTAL FLUX= 2.995719E-01kW

MASS FLOW RATE= 2.32 g/min

METHANOL 7.1 cm TOTAL RADIATIVE OUTPUT

METFLUXV.AVG  
axial

METFLXRB.AVG  
radial

SIGNAL (v)	POS (cm)	SIGNAL (v)	POS (cm)
.40920E-01	.00	.19296E+00	.00
.44989E-01	2.54	.19296E+00	6.35
.47375E-01	5.08	.11949E+00	8.89
.50509E-01	7.62	.80454E-01	11.43
.50366E-01	10.16	.59800E-01	13.97
.51605E-01	12.70	.44879E-01	16.51
.52936E-01	15.24	.36288E-01	19.05
.52350E-01	17.78	.28638E-01	21.59
.45364E-01	20.32	.24460E-01	24.13
.44866E-01	22.86	.20701E-01	26.67
.45951E-01	25.40	.18175E-01	29.21
.37820E-01	27.94		
.35079E-01	30.48		
.29864E-01	33.02		
.28021E-01	35.56		
.28443E-01	38.10		
.25831E-01	40.64		
.23932E-01	43.18		
.20620E-01	45.72		
.17984E-01	48.26		
.16657E-01	50.80		
.00000E+00	67.55		

SIDE FLUX= 189.4828W BOTTOM FLUX= 48.27W

TOTAL FLUX= 2.377575E-01kW

RADIATION FRACTION= 2.0E-01 MASS FLOW RATE= 3.54 g/min

METHANOL 30 cm TOTAL RADIATIVE OUTPUT

m2ax.dat  
axial

m2ra.dat

radial

Q, (W/cm2)	POS (cm)	Q, (W/cm2)	POS (cm)
.56400E-01	.00	.26871E+00	.00
.60967E-01	5.00	.26871E+00	33.65
.62800E-01	10.00	.17226E+00	38.65
.65772E-01	15.00	.12019E+00	43.65
.63060E-01	20.00	.87388E-01	48.65
.65616E-01	25.00	.63150E-01	52.65
.62014E-01	30.00	.47510E-01	57.65
.61195E-01	35.00	.36852E-01	62.65
.62186E-01	40.00	.28524E-01	67.65
.57051E-01	45.00	.24192E-01	72.65
.53792E-01	50.00		
.48065E-01	60.00		
.39170E-01	70.00		
.33486E-01	80.00		
.26143E-01	90.00		
.22318E-01	100.00		
.17692E-01	110.00		
.15746E-01	120.00		
.00000E+00	162.17		

SIDE FLUX= 2535.563W BOTTOM FLUX=876.90W

TOTAL FLUX= 3.412463kW

RADIATION FRACTION= 0.17 MASS FLOW RATE= 0.9 g/s

METHANOL 100 cm TOTAL RADIATIVE OUTPUT

met#8xrc.dat

met#8xrr.dat

AXIAL

RADIAL

Q, W/cm2	POS (cm)	Q, W/cm2	POS (cm)
0.22973E-01	0.00	0.41005E+00	0.00
0.35090E-01	50.00	0.41005E+00	60.00
0.32085E-01	100.00	0.46911E-01	125.00
0.31711E-01	150.00	0.15743E-01	192.00
0.22722E-01	222.00	0.68980E-02	230.00
0.16869E-01	292.00	0.11580E-02	275.00
0.00000E+00	446.00	0.65500E-03	330.00

SIDE FLUX= 19418.5W BOTTOM FLUX= 8024.07W

TOTAL FLUX= 27.4425kW

TOLUENE 7.1 cm TOTAL RADIATIVE OUTPUT CALIB. CONST = 0.208 W/cm<sup>2</sup>-mv

tol2vert.ave  
axial

tol2rad.ave  
radial

SIGNAL (v)	POS (cm)	SIGNAL (v)	POS (cm)
.18150E+00	.00	.14390E+01	.00
.19440E+00	2.54	.14390E+01	6.35
.19020E+00	5.08	.84520E+00	8.89
.19930E+00	7.62	.53660E+00	11.43
.20990E+00	10.16	.39880E+00	13.97
.20550E+00	12.70	.32060E+00	16.51
.21190E+00	15.24	.25450E+00	19.05
.21620E+00	17.78	.20440E+00	21.59
.20980E+00	20.32	.14940E+00	26.67
.20630E+00	22.86	.10070E+00	31.75
.19900E+00	25.40	.72190E-01	38.10
.18830E+00	27.94	.66490E-01	39.37
.16750E+00	33.02		
.15180E+00	38.10		
.13440E+00	43.18		
.11500E+00	48.26		
.97830E-01	53.34		
.84510E-01	58.42		
.63910E-01	66.04		
.00000E+00	88.31		

SIDE FLUX= 1415.985W BOTTOM FLUX= 448.3577W

TOTAL FLUX= 1.864343kW

RADIATION FRACTION= 0.312 MASS FLOW RATE= 8.73 g/min

TOLUENE 100 CM TOTAL RADIATIVE OUTPUT

tol#4xrc.dat

tol#4xrr.dat

AXIAL		RADIAL	
Q, W/cm2	POS (cm)	Q, W/cm2	POS (cm)
0.33871E+00	0.00	0.41444E+01	0.00
0.39228E+00	50.00	0.41444E+01	60.00
0.40000E+00	100.00	0.14938E+01	122.00
0.40878E+00	150.00	0.13703E+00	250.00
0.33666E+00	222.00	0.44808E-01	285.00
0.19149E+00	350.00	0.19740E-01	345.00
0.11855E+00	400.00	0.84190E-02	442.00
0.00000E+00	502.00		

SIDE FLUX= 366777 W BOTTOM FLUX= 154290 W

TOTAL FLUX= 521.067 kW

**APPENDIX C**

**DIRECTIONAL RADIATIVE FEEDBACK**

METHANOL 30 cm DIRECTIONAL RADIATIVE FEEDBACK (W/m<sup>2</sup>-sr)

THETA (PHI = 90 DEG)	THETA (DEG)	(PHI=180 DEG)	THETA (DEG)	(PHI = 0 DEG)
90	110	130	150	30
8K/ 2365.079	2057.93	2206.349	1904.761	2206.349
0	12158.73	10101.58	8713.492	8571.428
2	11539.68	9095.238	8412.698	7744.444
4	10513.49	8445.238	8372.222	7544.444
6	8785.714	7341.269	7769.841	7277.777
8	8976.190	6523.809	7198.412	7873.015
10	7476.190	5428.571	5817.460	6744.444
12	5735.714	4333.333	4086.507	6211.111
13	5531.746	3571.428	3816.666	7563.492
14	4761.904	3174.603	3571.428	3968.253
15	3174.603	2380.952	2777.777	3174.603

HEPTANE 30 cm DIRECTIONAL RADIATIVE FEEDBACK (W/m<sup>2</sup>-sr)

	THETA (PHI = 90 DEG)	/	THETA (DEG)	(PHI=180)	/	THETA (DEG)	(PHI = 0 DEG)						
	90	110	130	150	30	50	70	90	50	70	90	50	30
BK/	1093.117	0	-809.716	-1497.97	-1174.08	-728.744	-931.174	1093.117	-404.048	-1076.92	-1294.33		
0	23481.78	12400.80	7219.433	3449.392	3238.866	7378.137	13995.95	23481.78	12927.53	7100.404	4385.020		
2	22753.03	11093.11	6829.554	3514.170	3594.736	8140.080	14840.48	22753.03	11144.53	5891.902	4006.477		
4	21862.34	13271.25	6165.991	2672.064	4194.331	9576.923	16560.32	21862.34	9616.599	4567.611	3209.716		
6	19299.59	12672.06	5633.603	2510.121	4717.408	13322.26	17952.22	19299.59	8448.178	3727.530	2167.611		
8	17546.55	11838.05	4618.623	2429.149	5240.080	14965.99	17607.28	17546.55	6927.530	3157.894	1829.149		
10	15854.25	10121.45	3473.684	2348.178	5763.157	16609.71	17871.25	15854.25	4028.744	2895.141	1634.817		
12	13000	8340.080	3008.097	2226.720	6286.234	18253.84	18135.22	13000	2570.850	2778.542	1631.174		
13	11572.87	9238.866	2834.008	2125.506	6547.368	19075.70	18267.61	11572.87	1840.890	2062.348	1656.275		
14	10145.74	8944.534	2429.149	2024.291	6808.906	19897.57	18399.59	10145.74	1110.931	1346.153	1627.530		
15	8718.623	8650.607	2024.291	1923.076	7070.445	20719.43	18531.57	8718.623	380.9716	629.9595	1625.910		

TOLUENE 30 cm DIRECTIONAL RADIATIVE FEEDBACK (W/m<sup>2</sup>-sr)

	THETA (PHI = 90 DEG)	THETA (DEG)	(PHI=180)	THETA (DEG)	(PHI = 0 DEG)	THETA (DEG)	(PHI = 0 DEG)	THETA (DEG)	(PHI = 0 DEG)					
	90	110	130	150	165	15	30	50	70	90	110	130	150	165
8K/	2040	1868.9	917.7	-363.1	-2381.4	43.55	-471.3	1169.8	2629.7	2040	-177.5	195	-1219	-2546
0	20199.3	17411.2	13513.6	8612.6	4300	6708.5	10645.7	15098.1	18091.8	20199.3	18194.6	11030	5994	6377.5
2	22032	19694	15637	9665.4	4357.4	7265.6	10837.9	17696	18169.8	22032	14044.9	12129.2	6417.4	5170.9
4	17412.1	19996	18291.8	10371.4	4445.4	7859.8	11295.8	18317.2	18939	17412.1	11922.1	10712.3	5654.1	4731.7
6	17588	14972.9	13973.1	10469.3	4361.1	9422.5	11663.8	20730.2	18390.4	17588	10859.1	9172.8	4405.9	3271.4
8	18357.1	14567.7	11277.8	10060.5	4700	10898.2	13149.3	22242	21534.3	18357.1	10047.2	8069.1	4723.5	3383
10	18407.5	13101.4	10973.2	9022.8	4816	12373.9	14634.6	23753.8	19408.7	18407.5	9582.8	7576.3	5183.5	3891.2
12	19501.4	11545.2	10731.5	7516.8	4900	13849.5	16119.5	25265.7	28612.9	19501.4	8869.9	6056	5360.8	3650.2
14	15990.2	10415.4	10000	7000	4900	15325.2	17604.8	26777.5	32152.3	15990.2	6786.5	6000	5000	3504.2

APPENDIX D

EMISSION/ABSORPTION PROPERTIES  
TOLUENE 30 cm

30 cm TOLUENE EMISSION/ABSORPTION PROPERTIES  
 x/D = 0.08

POS (mm)	TEMPER K	EMISS SOOT PPM	ABSORP SOOT PPM	INTEN( $\lambda = 1.0\mu\text{m}$ ) PPM	INTEN( $\lambda = 0.9\mu\text{m}$ ) PPM	W/m <sup>2</sup> -sr- $\mu\text{m}$	W/m <sup>2</sup> -sr- $\mu\text{m}$			
	MEAN	RMS	MEAN	RMS	MEAN	RMS	MEAN	RMS		
0	301.68	28.815	0.011	0.02085	10.115	6.3645	1.3645	5.4275	0.4875	2.3581
30	308.055	80.805	0.00625	0.09675	10.309	6.3895	2.5525	14.214	1.37165	7.658
90	323.805	157.355	0.0129	0.1866	8.163	5.751	5.8525	24.533	2.735	14.6055
120	323.000	155.145	0.01615	0.22695	7.6445	5.604	5.2965	11.571	2.88985	6.085
140	317.58	134.3	0.0134	0.1596	6.004	6.045	6.461	12.937	3.574	7.07
150	399.855	298.325	0.1255	0.51465	8.0115	5.8995	21.1415	69.1625	11.7525	40.4025
160	1016.91	466.395	1.90845	2.32275	6.06515	6.62535	329.1275	318.1425	187.361	194.545
170	375.91	288.21	0.02	0.2618	0.083	0.0511	13.118	12.678	7.106	7.896

X/D = 0.37

POS (mm)	TEMPER K	EMISS SOOT PPM	ABSORP SOOT PPM	INTEN( $\lambda = 1.0\mu\text{m}$ ) PPM	INTEN( $\lambda = 0.9\mu\text{m}$ ) $\text{W/m}^2\text{-sr-}\mu\text{m}$	MEAN	RMS	MEAN	RMS	MEAN	RMS
0	1155.625	106.34	6.8677	5.95435	11.9858	6.28945	196.11	156.3015	97.942	93.4075	
15	1142.9	101.925	7.3858	6.09985	12.8004	5.834	186.2765	155.04	91.6165	90.564	
30	1168.13	116.485	8.6308	6.45905	11.66625	6.0605	275.2285	212.581	139.2155	128.6545	
45	1163.935	140.735	7.5722	6.20665	12.43745	6.24865	252.182	234.562	130.851	142.903	
60	1217.19	195.51	5.2602	5.0546	7.98025	6.37265	375.4065	313.898	205.247	193.0195	
75	1183.52	279.645	3.7562	3.9657	7.3122	6.11395	340.986	311.458	189.052	192.144	
90	954.39	456.18	1.7696	2.3355	4.33635	4.3475	226.988	286.052	127.412	172.4195	
105	724.33	541.535	0.6844	1.8105	1.5504	2.8474	121.9355	281.4045	72.1955	174.425	
120	534.495	564.135	0.32025	1.5113	0.67245	2.0316	30.791	132.255	237.327	84.681	

X/D = 0.8

POS (mm)	TEMPER K	EMISS SOOT PPM	ABSORP SOOT PPM	INTEN( $\lambda = 1.0\mu\text{m}$ ) PPM	INTEN( $\lambda = 0.9\mu\text{m}$ ) $\text{W/m}^2\text{-sr-}\mu\text{m}$	MEAN	RMS	MEAN	RMS	MEAN	RMS
0	1143.26	282.01	6.0228	5.0127	6.1039	4.1356	404.062	334.842	210.565	197.788	
15	1134.07	273.63	6.0986	5.2581	6.3214	3.8671	375.781	352.435	195.867	210.187	
30	1124.17	289.75	6.1026	5.2535	5.4956	3.851	371.158	329.532	191.55	194.876	
45	1030.33	313.055	5.9362	5.8818	3.965	2.6328	214.1275	269.7445	106.48	156.1685	
60	553.61	428.53	0.8205	1.9747	6.16965	4.1107	94.7015	233.4435	51.496	137.7955	
75	549.59	425.06	0.82455	2.05065	5.07855	2.3719	85.422	218.9695	46.089	129.0245	
90	511.12	389.3	0.5619	1.54585	3.5036	2.08515	69.5395	181.657	38.927	104.421	
105	333.45	164.98	0.1001	0.6924	3.7685	1.49755	10.3065	54.862	6.1245	30.1245	

x/D = 2.3

POS (mm)	TEMPER K	EMISS SOOT		ABSORP SOOT		INTEN( $\lambda = 1.0 \mu\text{m}$ )		INTEN( $\lambda = 0.9 \mu\text{m}$ )		
		PPH	RMS	PPH	RMS	PPH	RMS	PPH	RMS	
		MEAN	RMS	MEAN	RMS	MEAN	RMS	MEAN	RMS	
0	997.7	411.88	3.2154	3.9464	3.37975	2.5857	201.756	239.5575	105.1875	139.047
20	984.36	399.25	3.8761	4.9266	13.8921	1.3491	196.0125	228.1685	100.6275	133.6185
40	885.1	469.565	2.03845	3.2126	2.34845	1.9058	139.07	216.4775	73.4965	126.4415
60	694.635	456.32	1.6144	3.0792	1.4031	1.7469	93.0525	171.6965	47.299	98.068
80	502.655	396.535	0.5942	1.795	0.72395	1.42865	40.048	130.27	21.73	74.8705
100	426.72	328.29	0.4239	1.73995	1.486	1.62145	28.895	125.959	15.8505	72.979
120	317.22	131.22	0.0415	0.4277	0.9822	0.629	7.9405	41.4745	2.87	24.525
150	305.865	75.88	0.01345	0.2765	0.40335	0.5086	5.3745	23.8155	1.5695	14.173

x/D = 3.3

POS (mm)	TEMPER K	EMISS SOOT		ABSORP SOOT		INTEN( $\lambda = 1.0 \mu\text{m}$ )		INTEN( $\lambda = 0.9 \mu\text{m}$ )		
		PPH	RMS	PPH	RMS	PPH	RMS	PPH	RMS	
		MEAN	RMS	MEAN	RMS	MEAN	RMS	MEAN	RMS	
0	880.99	459.7	1.6112	2.43745	2.2851	2.1205	110.82	149.2055	57.8715	84.9255
20	818.13	475.085	1.45875	2.5257	1.73115	1.7565	100.078	158.678	52.4455	90.729
40	635.965	450.015	0.86745	1.90465	1.18945	1.23105	56.8715	116.718	29.3615	65.2525
60	502.03	384.59	0.5009	1.4616	1.178	1.53065	32.439	89.608	16.683	49.2695
80	429.47	322.98	0.30495	1.13945	1.48255	0.9802	19.0465	69.7125	9.929	38.4725
100	385.64	268.51	0.2634	1.2734	2.1804	1.4315	14.595	72.711	7.556	41.446
120	337.29	181.065	0.0749	0.54415	0.95215	1.72605	5.4215	28.031	2.727	15.211

X/D = 3.7

POS (mm)	TEMPER K	EMISS SOOT PPM		ABSORP SOOT PPM		INTEN( $\lambda = 1.0\mu\text{m}$ ) PPM		INTEN( $\lambda = 0.9\mu\text{m}$ ) PPM		W/m <sup>2</sup> -sr- $\mu\text{m}$	
		MEAN	RMS	MEAN	RMS	MEAN	RMS	MEAN	RMS	MEAN	RMS
0	880.99	459.7	1.6112	2.43745	2.2851	2.1205	110.82	149.2055	57.8715	84.9255	
20	818.13	475.085	1.45875	2.5257	1.73115	1.7565	100.078	158.678	52.4455	90.729	
40	635.965	450.015	0.86745	1.90465	1.18945	1.23105	56.8715	116.718	29.3615	65.2525	
60	502.03	384.59	0.5009	1.4616	1.178	1.53065	32.439	89.608	16.683	49.2695	
80	429.47	322.98	0.30495	1.13945	1.48255	0.9802	19.0465	69.7125	9.929	38.4725	
100	385.64	268.51	0.2634	1.2734	2.1804	1.4315	14.595	72.711	7.556	41.446	
120	337.29	181.065	0.0749	0.54415	0.95215	1.72605	5.4215	28.031	2.727	15.211	

X/D = 4.3

POS (mm)	TEMPER K	EMISS SOOT PPM		ABSORP SOOT PPM		INTEN( $\lambda = 1.0\mu\text{m}$ ) PPM		INTEN( $\lambda = 0.9\mu\text{m}$ ) PPM		W/m <sup>2</sup> -sr- $\mu\text{m}$	
		MEAN	RMS	MEAN	RMS	MEAN	RMS	MEAN	RMS	MEAN	RMS
0	460.805	369.93	0.2227	0.781	1.45585	1.034	22.7725	13.173	45.9625		
20	436.1	344.58	0.1819	0.6789	1.1944	0.771	19.393	10.300	36.71		
40	387.45	283.7	0.1078	0.54135	1.2474	1.4338	11.7445	7.027	26.8865		
60	367.16	247.25	0.0955	0.55535	1.49975	1.0509	9.04	5.589	21.776		
80	344.99	196.72	0.1376	0.88945	1.7567	0.63615	7.8825	4.092	20.561		
100	348.305	199.815	0.18225	1.04165	1.8362	0.682	9.471	4.412	22.0565		
120	318.575	126.2	0.08	0.7436	0.5835	0.9048	7.284	2.164	16.765		
140	307.96	83.245	0.02095	0.28545	0.37925	0.46335	4.6025	0.980	7.479		

HEPTANE 30 CM

x/D = 0.2

POS TEMPER (mm) K	EMISS SOOT PPH	ABSORP SOOT PPH	INTEN( $\lambda=1.0\mu\text{m}$ ) PPH	INTEN( $\lambda=0.9\mu\text{m}$ ) PPH	MEAN	RMS	MEAN	RMS	MEAN	RMS	MEAN	RMS	W/m <sup>2</sup> -sr- $\mu\text{m}$
0	1041.17	652.77	0.2189	0.6177	1.2797	0.4711	47.17	117.11	70.89	177.18			
30	1237.15	502.25	0.36025	0.89985	1.69905	0.52965	61.91	106.345	97.53	162.595			
50	1298.98	528.185	0.2919	0.68855	0.42145	0.61815	78.52	134.48	118.845	197.855			
70	1210.34	576.035	0.2774	0.57025	0.8116	0.70715	111.115	194.975	163.5	280.845			
90	599.40	562.135	0.0812	0.2857	0.358	0.2843	43.08	151.69	59.6	215.465			

x/D = 0.9

POS TEMPER (mm) K	EMISS SOOT PPH	ABSORP SOOT PPH	INTEN( $\lambda=1.0\mu\text{m}$ ) PPH	INTEN( $\lambda=0.9\mu\text{m}$ ) PPH	MEAN	RMS	MEAN	RMS	MEAN	RMS	MEAN	RMS	W/m <sup>2</sup> -sr- $\mu\text{m}$
0	1273.176	398.5633	0.541066	0.716066	0.762133	0.448933	148.9666	198.56	235.817	296.09			
20	1350.086	470.9833	0.375833	0.5632	0.639366	0.8395	172.5166	239.08	260.91	346.51			
30	1177.793	540.4133	0.383366	0.515633	0.868733	0.525433	149.6966	218.7966	231.11	324.5			
40	1228.816	548.4733	0.3187	0.489033	0.6332	0.484566	150.3766	221.2833	227.677	324.11			
60	579.0033	521.9733	0.114233	0.340633	0.4194	0.529066	57.6667	166.8366	85.157	248.5733			
80	418.655	376.73	0.0454	0.2092	0.32795	0.5914	27.96	111.475	37.18	166.16			

x/D = 1.5

POS TEMPER (mm) K	EMISS SOOT PPH	ABSORP SOOT PPH	INTEN( $\lambda = 1.0\mu\text{m}$ ) PPH	INTEN( $\lambda = 0.9\mu\text{m}$ ) $\text{W/m}^2\text{-sr-}\mu\text{m}$	INTEN( $\lambda = 0.9\mu\text{m}$ ) $\text{W/m}^2\text{-sr-}\mu\text{m}$					
MEAN RMS	MEAN RMS	MEAN RMS	MEAN RMS	MEAN RMS	RMS					
0	1282.045	336.1	0.88485	1.20145	0.789	0.68225	302.775	326.315	188.3255	218.817
30	1202.735	473.245	0.57015	0.70255	0.70095	0.5069	284.711	332.9605	180.9605	223.0635
60	707.365	583.97	0.16935	0.3737	0.69065	1.0324	114.197	251.046	74.756	165.9975
90	443.305	389.085	0.07285	0.27515	0.6774	0.3532	46.5985	173.5465	31.4265	114.196
120	354.56	248.59	0.02985	0.1818	0.4173	0.80875	17.643	95.6485	12.8555	61.009

x/D=2.2

POS TEMPER (mm) K	EMISS SOOT PPH	ABSORP SOOT PPH	INTEN( $\lambda = 1.0\mu\text{m}$ ) PPH	INTEN( $\lambda = 0.9\mu\text{m}$ ) $\text{W/m}^2\text{-sr-}\mu\text{m}$	INTEN( $\lambda = 0.9\mu\text{m}$ ) $\text{W/m}^2\text{-sr-}\mu\text{m}$					
MEAN RMS	MEAN RMS	MEAN RMS	MEAN RMS	MEAN RMS	RMS					
0	1154.605	505.365	0.52355	0.591	0.94765	0.5982	251.5035	298.894	158.514	195.437
30	1180.425	482.07	0.6036	0.7128	0.81275	0.8819	268.079	317.595	167.830	208.574
60	996.115	617.89	0.3154	0.4874	0.53715	0.4814	204.963	306.2905	133.679	202.536
90	762.78	603.31	0.2074	0.4391	0.794	1.2843	123.863	244.8425	81.383	158.9835
120	515.235	454.71	0.10345	0.3155	0.4349	0.7616	62.8365	180.2375	41.965	117.2795
150	389.245	311.725	0.0349	0.17255	0.4966	1.05495	22.437	96.1795	17.395	61.4785

x/D = 3.4

POS (mm)	TEMPER K	EMISS SOOT		ABSORP SOOT		INTEN( $\lambda = 1.0\mu\text{m}$ )		INTEN( $\lambda = 0.9\mu\text{m}$ )		$\text{W/m}^2\text{-sr-}\mu\text{m}$
		PPH	RMS	PPH	RMS	PPH	RMS	PPH	RMS	
0	764.70	628.053	0.1713	0.382	0.6226	1.0375	98.58	208.89	68.95	132.66
30	853.02	650.247	0.20363	0.45057	0.7213	0.8300	120.02	230.13	82.42	148.34
60	788.26	639.433	0.1659	0.3789	0.6494	0.8556	101.42	212.72	70.93	137.63
90	576.36	516.490	0.10723	0.3327	0.5583	0.3416	58.32	151.20	43.92	96.89
120	581.51	537.40	0.0848	0.2419	0.5418	0.5833	63.55	165.29	51.49	106.90
150	507.4	462.080	0.0783	0.2926	0.6912	0.3444	51.15	129.91	47.75	84.00

x/D = 4.2

POS (mm)	TEMPER K	EMISS SOOT		ABSORP SOOT		INTEN( $\lambda = 1.0\mu\text{m}$ )		INTEN( $\lambda = 0.9\mu\text{m}$ )		$\text{W/m}^2\text{-sr-}\mu\text{m}$
		PPH	RMS	PPH	RMS	PPH	RMS	PPH	RMS	
0	372.21	267.90	0.1891	1.157	0.2475	0.1711	18.13	80.78	14.02	41.84
30	431.22	336.79	0.4575	1.880	0.7246	0.2754	35.16	117.55	20.18	61.45
60	458.04	369.95	0.5092	1.791	1.0880	0.7734	42.89	132.33	25.02	69.45
90	467.01	388.32	0.4254	1.555	0.7048	0.7458	41.37	131.66	25.24	69.54
120	374.43	255.13	0.1959	0.956	0.5999	0.2998	19.70	81.96	13.38	43.50
150	433.1	344.90	0.3671	1.402	0.8107	0.7778	35.90	122.41	21.17	65.58

**APPENDIX E**  
**SPECTRAL EMISSION AND FUEL VAPOR TRANSMITTANCE**  
**FUEL SURFACE REFLECTION**

FLAME EMISSION

TOLUENE		HEPTANE	
$\lambda$ (nm)	I (W/m <sup>2</sup> -sr- $\mu$ m)	$\lambda$ (nm)	I (W/m <sup>2</sup> -sr- $\mu$ m)
850.0	144.0	1200.0	697.8
900.0	206.3	1300.0	766.4
950.0	237.2	1400.0	847.0
1000.0	329.7	1500.0	962.7
1050.0	388.0	1600.0	882.9
1100.0	453.9	1700.0	938.1
1150.0	551.6	1800.0	1180.3
1200.0	808.4	1900.0	649.5
1600.0	2664.3	2000.0	898.1
1700.0	2098.8	2100.0	517.7
1800.0	2897.3	2200.0	609.4
1900.0	3353.0	2300.0	653.0
2000.0	2926.0	2400.0	522.2
2100.0	3381.0	2500.0	712.9
2200.0	2810.0	2600.0	1005.8
2300.0	2887.0	2700.0	1078.1
2400.0	2990.0	2800.0	1273.5
2500.0	2662.0	3100.0	944.3
2600.0	2903.0	3200.0	795.2
2700.0	2544.0	3300.0	593.3
2800.0	2517.4	3400.0	803.8
3200.0	1480.0	3500.0	892.7
3400.0	1634.0	3600.0	505.2
3600.0	1324.0	3700.0	286.9
3800.0	1374.0	3800.0	278.0
4000.0	1225.3	3900.0	252.9
4200.0	1933.0	4100.0	210.7
4400.0	3186.0	4200.0	1128.8

4600.0	1789.7	4300.0	781.5
4800.0	1739.0	4400.0	3950.1
		4500.0	2560.6
		4600.0	1601.6
		4700.0	409.9
		4800.0	248.5

**FUEL VAPOR TRANSMITTANCE**

TOLUENE		HEPTANE	
$\lambda$ (nm)	TRANSMITTANCE	$\lambda$ (nm)	TRANSMITTANCE
1000.000	0.940	1200.000	0.955
1100.000	0.947	1300.000	1.000
1200.000	0.965	1500.000	0.997
1300.000	0.957	1600.000	1.000
1400.000	0.959	1700.000	1.000
1500.000	0.959	1800.000	0.998
1600.000	0.965	1900.000	1.000
1700.000	0.950	2000.000	0.995
1800.000	0.972	2100.000	0.997
1900.000	0.980	2200.000	0.998
2000.000	0.969	2300.000	1.000
2100.000	0.968	2400.000	0.957
2200.000	0.946	2500.000	0.995
2300.000	0.945	2600.000	0.889
2400.000	0.941	2700.000	0.965
2500.000	0.915	2800.000	0.931
2700.000	0.963	3000.000	0.950
2800.000	0.960	3100.000	0.940
2900.000	0.967	3200.000	0.918
3000.000	0.955	3300.000	0.996

3200.000	0.669	3400.000	0.771
3400.000	0.650	3500.000	0.726
3600.000	0.985	3600.000	0.926
3800.000	0.998	3700.000	0.915
4000.000	0.999	3800.000	0.936
4200.000	0.989	3900.000	0.956
4400.000	0.968	4000.000	0.953
4600.000	0.929	4100.000	0.953
		4200.000	0.958
		4300.000	0.913
		4400.000	0.683
		4500.000	0.815
		4600.000	0.854
		4700.000	0.967
		4800.000	0.966

FUEL SURFACE REFLECTION

WATER		TOLUENE		METHANOL		HEPTANE	
ANGLE	REFLEC.	ANGLE	REFLEC	ANGLE	REFLEC.	ANGLE	REFLEC.
6.49	0.580	6.49	0.660	5.37	0.444	6.60	0.925
11.00	0.370	12.10	0.360	13.20	0.327	14.50	0.263
18.00	0.130	26.40	0.126	21.50	0.117	22.30	0.120
35.50	0.074	35.50	0.075	54.78	0.026	54.78	0.036

## REFERENCES

Akita, K. and Yumoto, T., 1965, "Heat Transfer in Small Pools and Rates of Burning of Liquid Methanol", Tenth Symposium (International) on Combustion, The Combustion Institute, p. 943

Alger, R.S., Corlett, R.C., Gordon, A.S., and Williams, F.A., 1979, "Some Aspects of Structure of Turbulent Pool Fires", Fire Techn., Vol. 15, p. 142

Blinov, V.I. and Khudiakov G. N., 1957, "Diffusion Burning of Liquids", Dokl. Akad. Nauk. SSSR, Vol. 113, pp. 241-244.

Bouhafid, A., Vantelon J. P., and Joulain, P., 1988, "On the Flame Structure at the Base of a Pool Fire", Twenty-second Symposium (International) on Combustion, The Combustion Institute, Pittsburgh, pp. 1291-1298.

Box, G.E.P. and Jenkins, G.M., 1976, Time Series Analysis, Holden-Day, San Francisco.

Burgess D. and Hertzberg, M., 1974, "Radiation from Pool Flames", Heat Transfer in Flames, N. H. Afgan and J. M. Beer, Eds., Hemisphere, N.Y., pp. 413-430.

Corlett, R.C. and Fu, T.H., 1966, "Some Recent Experiments with Pool Fires", Pyrodynamics, Vol. 4, pp. 253-269.

Cox, G., 1977, "On Radiant Heat Transfer from Turbulent Flames", Combust. Sci. Tech., Vol. 17, pp. 75-78.

Dalzell, W. L. and Sarofim, A. F., 1969, "Optical Constants of Soot and their Application to Heat Flux Calculations", J. Heat Trans., vol 91, pp. 100-104.

Daubert, T. E. and Danner, R. P., 1984, "Data Compilation Tables of Properties of Pure Compounds", Design Institute for Physical Property Data, American Institute of Chemical Engineers, N.Y.

deRis, J., 1978, "Fire Radiation - a Review", Sixteenth Symposium (International) on Combustion, The Combustion Institute, Pittsburgh, pp. 1003-1016.

Edwards, D.K., and Menard, W. A., 1964, "Comparison of Models for Correlation of Total Band Absorption", Applied Optics, Vol. 3, pp. 621-625.

Faeth, G. M., Gore, J.P., Jeng, S.M., and Chuech, S.G.. 1989, "Radiation from Turbulent Diffusion Flames", Ann. Rev. Numerical Fluid Mech. and Heat Trans. (C. L. Tien and T. C. Chawla, Eds.), Vol. 2, pp. 1-38.

Fernandez-Pello, C., 1991, "Pool and Wall Fires: Some Fundamental Aspects", Proceedings of ASME/JSME Joint Thermal Engineering Conference, Vol.5, ASME, New York, pp. 261-268

Fischer, S.J., 1988, "Study of the Radiative Properties of Liquid Pool Fires", Ph.D. thesis, Washington State University, Department of Mechanical and Materials Engineering.

Fischer, S.J., Hardouin-Duparc, B. and Grosshandler, W. L., 1987, "The Structure and Radiation of and Ethanol Pool Fire," Comb. Flame, Vol. 70, pp. 291-306.

Gore, J.P., 1986, A Theoretical and Experimental Study of Turbulent Flame Radiation, Ph.D. Thesis, The Pennsylvania State University, University Park, PA.

Gore, J.P. and Faeth, G.M., 1986, "Structure and Spectral Radiation Properties of Turbulent Ethylene/Air Diffusion Flames", Twenty-First Symposium (International) on Combustion, The Combustion Institute, Pittsburgh, pp. 1521-1531.

Gore, J.P. and Faeth, G.M., 1988, "Structure and Spectral Radiation Properties of Luminous Acetylene/Air Diffusion Flames", J. Heat Trans., Vol. 110, pp. 173-181.

Gore, J.P., Klassen, M., Hamins, A., and Kashiwagi, T., 1991, "Fuel Property Effects on Burning Rate and Radiative Transfer from Liquid Pool Flames", Fire Safety Science Proceedings of the Third International Symposium, (G. Cox and B. Langford, Eds.), Elsevier Science Publishers Ltd., London, pp. 395-404.

Goody, R. M. (1964), Atmospheric Radiation. Theoretical Base, Vol. 1, Clarendon Press, Oxford.

Grosshandler, W.L. and Sawyer, R. F., 1978, "Radiation from a Methanol Furnace", J. Heat Transfer, Vol. 100, pp. 247-252.

Grosshandler, W.L. and Joulain, P., 1986, P. Astro. Aero, Vol. 105II p.123.

Hamins, A., 1992, Personal Communication

Hamins, A., Klassen, M., Gore, J., and Kashiwagi, T., 1991, "Estimate of Flame Radiance via a Single Location Measurement", Comb. Flame, Vol. 86, p.223.

Hamins, A., Yang, J.C. and Kashiwagi, T., 1992, "A Simple Model for Predicting the Burning Rate of Liquid Pool Flames", Fire Safety Journal, submitted.

Hottel, H.C., 1958, "Review of Certain Laws Governing Diffusive Burning of Liquids", Fire Res. Abs. and Rev., Vol. 1, pp.41-44.

Hottel, H.C., and Sarofim, A. F., 1967, Radiative Transfer, McGraw Hill, New York.

Jeng, S-M and Faeth, G.M., 1984, "Species Concentrations and Turbulence Properties in Buoyant Methane Diffusion Flames", J. Heat Transfer, Vol. 106, pp. 721-727.

Kabashnikov, V.P. and Kmit, G.I., 1979, "Influence of Turbulent Fluctuations on Thermal Radiation", J. Applied Spect., Vol. 31, pp. 963-967.

Klassen, M., Gore, J.P., Sivathanu, Y.R., Hamins, A., and Kashiwagi, T. (1992), "Radiative Heat Feedback in a Toluene Pool Fire", Twenty-Fourth Symposium (Inter.) on Combustion, accepted.

Klassen, M., Gore J. P., Sivathanu Y.R., (1992), "Simultaneous Emission Absorption Measurements in Toluene-Fueled Pool Flames: Mean and RMS Properties", Comb. Flame, in press.

Koseki, H. and Yumoto T., 1988, "Air Entrainment and Thermal Radiation from Heptane Pool Fires", Fire Techn., Vol. 24, pp. 33-47

Kounalakis, M.E., Gore, J.P., and Faeth, G.M., 1988, "Turbulence/Radiation Interactions in Nonpremixed Hydrogen/Air Flames", Twenty-Second Symposium (International) on Combustion, The Combustion Institute, Pittsburgh, pp. 1281-1290.

Kounalakis, M. E., Gore, J.P., and Faeth, G.M., 1988, "Mean and Fluctuating Radiation Properties of Nonpremixed Turbulent Carbon Monoxide/Air Flames", J. Heat Transfer, Vol. 111, pp. 1021-1030.

Köylü, Ü.Ö., and Faeth, G.M. (1991), "Carbon Monoxide and Soot Emissions from Liquid-Fueled Buoyant Turbulent Diffusion Flames", Comb. Flame, Vol. 87, pp. 61-76.

Liu, K.V., Lloyd, J. R., and Yang, K. T., 1981, "An investigation of Laminar Diffusion Flame Adjacent to a Vertical Flat Plate Burner", Int.J. Heat Mass Transfer, Vol. 24, pp. 1407-1419.

Ludwig, C. B., Malkmus, W., Reardon, J.E., and Thomson, J.A., 1973, Handbook of Infrared Radiation from Combustion Gases, NASA SP-3080.

Markstein, G. H., 1981, "Scanning Radiometer Measurements of the Radiance Distribution in PMMA Pool Fires", Eighteenth Symposium (Inter.) on Combustion, The Combustion Institute, Pittsburgh, pp. 537-547.

Markstein, G. H., 1984, "Relationship between Smoke Point and Radiant Emission from Bouyant Turbulent and Laminar Diffusion Flames", Twentieth Symposium (International) on Combustion, The Combustion Institute, Pittsburgh, pp. 1055-1063.

McCaffrey, B.J., 1979, "Purely Buoyant Diffusion Flames: Some Experimental Results", NBSIR79-1910, National Bureau of Standards, Washington, D.C.

Modak, A. T., 1977, "Thermal Radiation from Pool Fires", Comb. Flame, Vol.29, pp.177-192.

Modak, A. T., 1981, "The Burning of Large Pool Fires", Fire Safety Journal, Vol. 3, pp. 177-184.

Modak, A.T. and Croce, P., 1977, "Plastic Pool Fires", Comb. Flame, Vol. 30, 1977, pp. 251-265.

Mudan, K.S., 1984, "Thermal Radiation Hazards from Hydrocarbon Pool Fires", Prog. Eng. Comb. Sci., Vol. 10, pp. 59-80.

Mulholland, G.W., Henzel, V. and Babrauskas, V., 1988, "The Effect of Scale on Smoke Emission", Fire Safety Proceedings of the Second International Symposium, pp. 347-357.

Orloff, L., 1981, "Simplified Radiation Modeling of Pool Fires", Eighteenth Symposium (International) on Combustion, The Combustion Institute, Pittsburgh, pp. 549-561.

Negrelli, D. E., Lloyd, J. R., and Novotny, J. L., 1977, "A Theoretical and Experimental Study of Radiation Convection Interaction in a Diffusion Flame", J. Heat Transfer, Vol. 99, pp. 212-220.

Pagni, P. J., 1989, ASME Paper Number 89-WA/FE-5, p.26

Portscht, R., 1974, "Studies of characteristic Fluctuations of Flame Radiation emitted by Fires", Combust. Sci. Tech., Vol. 10, pp. 73-84.

Quintiere, J. G., 1992, "Pool Fires - A Review", submitted to Prog. Eng. Comb. Sci.

Shinotake, A., Koda, S., and Akita, K., 1985, "An Experimental Study of Radiative Properties of Pool Fires of an Intermediate Scale", Combust. Sci. and Tech., Vol. 43, pp. 85-97.

Shokri, M. and Beyler C.L., 1989, "Radiation from Large Pool Fires", J. of Fire Prot. Engr., Vol. 1, pp. 141-150.

Siegal, H. and Howell, J.R., 1981, Thermal Radiation Heat Transfer, McGraw-Hill, N.Y.

Sivathanu, Y.R., 1990, Soot and Radiation Properties of Buoyant Turbulent Diffusion Flames, Ph.D thesis, University of Michigan, Ann Arbor, MI.

Sivathanu, Y.R., Kounalakis, M.E., and Faeth, G.M., 1990, "", Twenty-Third Symposium (International) on Combustion, The Combustion Institute, Pittsburgh, pp. 1543

Sivathanu, Y.R., Gore, J.P., and Dolinar, J., 1991, "Transient Scalar Properties of Strongly Radiating Jet Flames", Combust. Sci. Tech., Vol. 76, pp. 45-66.

Sivathanu, Y.R. and Gore, J.P., 1991, "Simultaneous Multiline Emission Absorption Measurements in Optically Thick Turbulent Flames", Combust. Sci. Tech., Vol.80, pp.1-21.

Sivathanu, Y.R., and Gore, J.P. (1992), "Transient Structure and Radiation Properties of Acetylene/Air Pool Flames", ASME J. Heat Trans., in press.

Steward, F.R., 1970, "Prediction of the Height of Turbulent Diffusion Buoyant Flames", Combust. Sci. Tech., Vol. 2, pp. 203-212.

Terai, T. and Nitta, K., 1975, Proc. Syms. Arch. Inst., Japan. Cited in Zukoski et al., 1984.

Thomas, P.H., 1962, "The Size of Flames from Natural Fires", Ninth Symposium (International) on Combustion, The Combustion Institute, Pittsburgh, pp. 844-859.

Tien C.L. and Lee, S.C., 1982, "Flame Radiation", Prog. Energy Comb. Sci., pp. 41-59.

Weckman, E.J. and Sobiesiak A. , 1989, "The Oscillatory Behaviour of Medium Scale Pool Fires", Twenty-Second Symp. (International) on Combustion, The Combustion Institute, Pittsburgh, pp. 1299-1310.

You, H.Z. and Faeth, G.M., 1979, "Ceiling Heat Transfer During Fire Plume and Fire Impingement", Fire and Materials, Vol. 3, pp. 140-147.

Yumoto, T., 1971, "Heat Transfer from Flame to Fuel Surface in Large Pool Fires", Comb. Flame, Vol. 17, p. 108.

Zukoski, E.E., Cetegen, B.M., and Kubota, T., 1984, "Visible Structure of Buoyant Diffusion Flames", Twentieth Symposium (International) on Combustion, The Combustion Institute, Pittsburgh, pp. 361-366.

NIST-114 (REV. 6-93) ADMAN 4.09		<b>U.S. DEPARTMENT OF COMMERCE</b> NATIONAL INSTITUTE OF STANDARDS AND TECHNOLOGY		(ERB USE ONLY)	
<b>MANUSCRIPT REVIEW AND APPROVAL</b>		ERB CONTROL NUMBER		DIVISION	
		PUBLICATION REPORT NUMBER NIST-GCR-94-651		CATEGORY CODE	
INSTRUCTIONS: ATTACH ORIGINAL OF THIS FORM TO ONE (1) COPY OF MANUSCRIPT AND SEND TO THE SECRETARY, APPROPRIATE EDITORIAL REVIEW BOARD		PUBLICATION DATE June 1994		NUMBER PRINTED PAGES	
TITLE AND SUBTITLE (CITE IN FULL) Structure and Radiation Properties of Pool Fires					
CONTRACT OR GRANT NUMBER 60NANB1D1169			TYPE OF REPORT AND/OR PERIOD COVERED September 1, 1991 - August 31, 1992		
AUTHOR(S) (LAST NAME, FIRST INITIAL, SECOND INITIAL) M.Klassen, J.P. Gore Purdue University West Lafayette, IN			PERFORMING ORGANIZATION (CHECK (X) ONE BOX) <input type="checkbox"/> NIST/GAITHERSBURG <input type="checkbox"/> NIST/BOULDER <input type="checkbox"/> JILA/BOULDER		
LABORATORY AND DIVISION NAMES (FIRST NIST AUTHOR ONLY)					
SPONSORING ORGANIZATION NAME AND COMPLETE ADDRESS (STREET, CITY, STATE, ZIP) U.S. Department of Commerce National Institute of Standards and Technology Gaithersburg, MD 20899					
PROPOSED FOR NIST PUBLICATION					
<input type="checkbox"/>	JOURNAL OF RESEARCH (NIST JRES)	<input type="checkbox"/>	MONOGRAPH (NIST MN)	<input type="checkbox"/>	LETTER CIRCULAR
<input type="checkbox"/>	J. PHYS. & CHEM. REF. DATA (JPCRD)	<input type="checkbox"/>	NATL. STD. REF. DATA SERIES (NIST NSRDS)	<input type="checkbox"/>	BUILDING SCIENCE SERIES
<input type="checkbox"/>	HANDBOOK (NIST HB)	<input type="checkbox"/>	FEDERAL INF. PROCESS. STDS. (NIST FIPS)	<input type="checkbox"/>	PRODUCT STANDARDS
<input type="checkbox"/>	SPECIAL PUBLICATION (NIST SP)	<input type="checkbox"/>	LIST OF PUBLICATIONS (NIST LP)	<input checked="" type="checkbox"/>	OTHER <u>NIST-GCR</u>
<input type="checkbox"/>	TECHNICAL NOTE (NIST TN)	<input type="checkbox"/>	NIST INTERAGENCY/INTERNAL REPORT (NISTIR)		
PROPOSED FOR NON-NIST PUBLICATION (CITE FULLY)		<input type="checkbox"/> U.S.	<input type="checkbox"/> FOREIGN	PUBLISHING MEDIUM	
				<input checked="" type="checkbox"/> PAPER	<input type="checkbox"/> CD-ROM
				<input type="checkbox"/> DISKETTE (SPECIFY)	
				<input type="checkbox"/> OTHER (SPECIFY)	
SUPPLEMENTARY NOTES					
ABSTRACT (A 2000-CHARACTER OR LESS FACTUAL SUMMARY OF MOST SIGNIFICANT INFORMATION. IF DOCUMENT INCLUDES A SIGNIFICANT BIBLIOGRAPHY OR LITERATURE SURVEY, CITE IT HERE. SPELL OUT ACRONYMS ON FIRST REFERENCE.) (CONTINUE ON SEPARATE PAGE, IF NECESSARY.)					
<p>An experimental and theoretical study of radiative feedback, burning rates, radiative heat loss fractions, and flame heights for pool fires with diameters ranging from 4.6 cm to 100 cm was completed. Transient measurements of soot and temperature distributions were obtained in 7.1 cm and 30 cm heptane and toluene fires using a three-wavelength emission/absorption probe. The heat release rates of the fires varied from 0.6 kW to 2166 kW allowing a study over a wide range. A variety of fuels were tried but most of the measurements were restricted to methanol, heptane, and toluene as representatives of the alcohols, paraffins and aromatics. Radiative feedback was measured using a new insitu purged optical probe inserted at the level of the fuel surface. Measurements of reflection of energy from the fuel surface were also obtained. A multi-ray radiation calculation procedure utilizing simultaneous single-point measurements of soot volume fractions and temperatures was used to estimate the heat transfer to the surroundings and that to the fuel surface. Importance of turbulent fluctuations of different frequencies on the radiation heat flux was studied using filtered simulations.</p>					
KEY WORDS (MAXIMUM OF 9; 28 CHARACTERS AND SPACES EACH; SEPARATE WITH SEMICOLONS; ALPHABETIC ORDER; CAPITALIZE ONLY PROPER NAMES)					
burning rate; flame height; heat loss; heat transfer; measurement; pool fires; radiation; soot; temperature distribution					
AVAILABILITY				NOTE TO AUTHOR(S): IF YOU DO NOT WISH THIS MANUSCRIPT ANNOUNCED BEFORE PUBLICATION, PLEASE CHECK HERE. <input checked="" type="checkbox"/>	
<input checked="" type="checkbox"/>	UNLIMITED	<input type="checkbox"/>	FOR OFFICIAL DISTRIBUTION - DO NOT RELEASE TO NTIS		
<input type="checkbox"/>	ORDER FROM SUPERINTENDENT OF DOCUMENTS, U.S. GPO, WASHINGTON, DC 20402				
<input checked="" type="checkbox"/>	ORDER FROM NTIS, SPRINGFIELD, VA 22161				

WORDPERFECT